INVESTIGATION OF DIFFUSION AND SOLID STATE REACTIONS ON THE NANOSCALE IN SILICON BASED SYSTEMS OF HIGH INDUSTRIAL POTENTIAL: EXPERIMENTS AND SIMULATIONS

CO-DIRECTED PHD THESIS
FRANCE-HUNGARY

by

Bence PARDITKA

for the degree of
DOCTOR OF PHILOSOPHY

In the subject of:
MATERIALS SCIENCE

Members of the Jury:

Bernard AUFRAY
Frédéric CHRISTIEN (Referee)
Csaba CSERHÁTI
Zoltán ERDÉLYI
Christophe GIRARDEAUX
Gabor LANGER
Alain PORTAVOCE
Kálmán VAD (Referee)

Contents

„…Well, my brother has his sword, and I have my mind. And a mind needs books like a sword needs a whetstone. That's why I read so much …"

Game of Thrones
George R.R. Martin

Motivations

In our new, modern Si based technological world the leading role belongs to the Si-Ge based electronic devices and to the different metal silicides and to the industries behind them. These metal- silicides whatever they are contact or structural materials play a significant role in the modern electronics.

It is in the human nature to study the surrounding world, to find, identify, categorize the things around us and tame them, form them in the way they serve us best.

Physical theories emerged in the ancient Greece, including the atomic theory as well (around the 5th century). Democritus, Greek philosopher named the building blocks of matter, and so the building blocks of everything around us, "*átomos"*, meaning "indivisible". They believed that atoms were uniform, solid, incompressible, uncuttable and so indestructible [1].Though, some parts of their theories have been overthrown by newer discoveries, thanks to the advanced ideas, devices and techniques, but the atoms themselves still remained the building blocks of our world. The atoms and the technologies behind the endeavor to manipulate the matter on atomic scale are the key to high-tech future devices.

The increased demand for miniaturization in every level and field of science is present. However decreasing the size of any kind of device, technically important structure, etc. inevitable the consequences of these changes can significantly affect the properties of the product. By decreasing the size of any unit, device e.g. in the field of electronics can considerably improve its performance it can open a door towards new problems we have to face with. By closing to the scale of single atomic layers or some tenth of nanometers in thin solid films the diffusion or diffusion related mechanisms can drastically alter the structure and through the properties of the product at elevated temperatures or even during the fabrication. The redistribution of materials, atoms within small particles, thin films and structures thus can considerably change its physical and chemical properties. Since this redistribution in this atomic scale takes place via diffusion its kinetics can identify some important details about the characteristics of diffusion at this short range close to the surface that can be very different from the diffusion in the bulk.

Thin films, layered structures are very important in science. The thickness of these layers scales from one atomic monolayer as it is in case of graphene or silicene to some hundred nanometers. The modern technology based upon them and we can find these layered structures just as in high-tech devices, as in everyday appliance, materials such as computers, calculators, lasers or even on glasses, sunglasses etc. Everywhere, where e.g. integrated circuits, microchips, secondary batteries, different optic devices can gain a foothold and beyond, they are present. Amongst the industrial applications one can find a huge variety of thin layered films of the elements of the periodic table. At this time however we will restrict our study to a specific branch of them only in order to fit in the boundaries of this thesis.

Silicon is still the basis for computer technology. Thus, the further investigations still of crucial importance until we find a new, better candidate as a replacement. Electronic devices based on semiconductor materials, such as Si and Ge, build up most of the applications that are used every day in our society. The need for the replacement of the vacuum tubes, the historical predecessors of the recently used electronic devices, has been raised in the mid twentieth century. From tablets through PCs to phones or even cars rely on these electronic devices. These units are prepared as a part of an integrated circuit or as a single piece of device as well. The technological importance of such devices comes from their property that by the addition of well calibrated amount of dopants, their conductivity can be controlled. Since their behavior can react to numerous external effects the applications based upon these materials include a quite large and diverse field e.g. sensors, solar cells, etc. The transistor is one of the semiconductor devices that reformed the face of the modern world. The first significant step in the history of transistors is the field effect transistors (FET) and the devices based upon them. Nowadays forced by the increased demand to reach higher efficiency with lower energy consumption metal–oxide–semiconductor field-effect transistors (MOSFETs) has become the most generally used transistors in integrated circuits (IC). Such microprocessor structures contain billions of transistors. The next step on this road came with the introduction of complementary metal–oxide–semiconductor (CMOS) structures, which ones consist of p- and n-channel MOSFETs. With this solution not just the energy consumption have been reduced more intensely, but another problem, the overheating, has been decreased as well, which one have become pretty significant problem since the increase of the number of the transistors within a unit area on the IC accelerated incredibly thanks to the miniaturization. The development of even more advanced units is still one of the main goals of this field.

While in one hand there was a great need for the reduction of their size on the other hand there came hand-in-hand with these efforts the increasing effects of diffusion with just as much weight in their fabrication as in their predictable life-time and properties.

The need for miniaturization demand new structures and materials, which ones are compatible with the already existing one, thus SiGe nano-scaled alloys, materials and their detailed

investigation are of great importance. Investigating the diffusion in semiconductor materials and other effects connected to diffusion is one of the most important task of solid state physics.[2,3]

In the early period of the technological breakthrough of solid state transistors, silicon based applications gained ground for their higher stability, though the charge carrier abilities of Ge were better. The very stable Si oxide compared to the less stable Ge oxide however made Si more attractive to the field of electronics. However the usage of the higher charge carrier abilities of Si-Ge alloys and their introduction into the already existing Si based technology could be still the matter of investigations. In turn these efforts demand the deeper understanding of the mechanisms that is behind the scene, a better understanding of the atomic mass transport, namely the diffusion in these materials.

In the applications silicon is usually in contact with different kind of materials, such as metals for example, and the reactions take place between them are worth to deal with. Materials like Cobalt (Co), Nickel (Ni), Copper (Cu), Silver (Ag) and Germanium (Ge) have a long last history with Silicon (see in the chapter of Results and Discussion) and some of them just started to face with new frontiers, finding a new solutions, new technologies of the future (see in the chapter of Results and Discussion). Thus silicon alloys are still in the focus point of material science. The importance of contact materials, new generation battery electrodes and the improved, low cost solar cell technologies can't be neglected. (Metal-) Silicides especially are of great importance. Running investigations on nanometric scale in order to find the answers for phenomena like stress effects, phase growing kinetics, and the improvement of the techniques we use to follow them, to tame them are just as important.

A promising candidate for the base material of the future electronic devices perhaps is the graphene. Though within this work we pay no considerable attention to the graphene itself, but we do focus on another 2D structure that possesses similar properties and similar honeycomb surface structure to graphene. This material is the silicene. As it is indicated in its name the structure of silicene is built upon Si atoms. This simple fact that the building blocks of silicene are the very same Si atoms that build up the devices of our technological society makes this structure so important and interesting for scientist all over the world.

In this manner, investigating reactions and the possibly emerging effects in technologically important Si based binary diffusion couples via experimental work and simulations had been settled as the main goal of this thesis. Simulations and experiments had been performed on systems: Si-Ge, Si-Cu, Si-Ni and Si-Ag in order to follow the effect of stress on diffusion, initial states of a growing silicide phase and to investigate the stability of different superstructures and phenomena which are of importance from fundamental and technological point of view.

Chapter I

Introduction

I. Introduction

The first section of this chapter gives an overview of volume diffusion focusing on the points relevant to the effects investigated in the framework of this these. After introduction to Fick's laws, the Boltzmann's transformation is discussed since the well-known Fickian or parabolic law (see later) will play an important role later on; first when we discuss our computer simulation investigation concerning that how stresses may affect diffusion kinetics and also when interpreting the experimental results obtained in the Si-Cu system. Then in the following subsection we will call up the main points of Stephenson's diffusion and stress model, which has been used for the computer simulations. Since in this study the composition dependence of the diffusion coefficient was a key factor, then the next subsection is dedicated to define the concept of diffusion asymmetry. Then there is a subsection to introduce the reactive-diffusion since reactive-diffusion processes have been studied experimentally both in the Si-Ni and Si-Cu systems. Finally, the last subsection is about diffusion of different species in Si, as in the framework of this thesis Si-metal contacts have been investigated experimentally and the Si-Ge was the basic model system for the computer simulation studies.

As Si-metal reactions are of importance not only for metallization processes in technology but also metal induced crystallization of Si, the second section summarizes the backgrounds of this process.

Since in the latter chapters a considerable effect of GBs (grain boundaries) will be included in the explanation of our result the third section recalls within a short discussion the principles of grain boundary diffusion.

The last section is summary of surface segregation which comes to play mainly in the interpretation of the results of the silicene studies but segregation process has also been observed in the Si-Cu system. Accordingly, we need some basic knowledge for the treatment of these results.

I.1 Volume Diffusion

The movement of atoms in the matter, whatever it is an ordered or disordered way, is called diffusion. This movement can take place in several well-known ways e.g. the mechanism of vacancies. The very first step toward the understanding and the controlling of the reactions in the matter on the nanoscale must be the understanding of the phenomena of diffusion.

Since the mid 18^{th} century Fick's laws are the origin/basis of the understanding of the diffusion.

I.1.1 Fick's laws

The first equation of Fick makes contact between the diffusion flux and the concentration by the diffusion coefficient tensor,

$$\vec{\mathrm{J}} = -\hat{\mathrm{D}}\mathrm{grad}\rho \tag{1}$$

where $\vec{\mathrm{J}}$ is the diffusion flux (number of atoms passed over a unit area under unit time), $\hat{\mathrm{D}}$ is the diffusion coefficient tensor while ρ equals to the number of atoms in a unit volume and grad is the gradient operator. In this way we can determine the diffusion coefficient only when the concentration gradient is independent of time.

From now on let us consider, for the sake of simplicity, that the mass transport, namely the diffusion permitted only in the direction *x*.

In order to integrate the conservation of matter into the equations of diffusion the equation of continuity had been created. The equation of continuity describes the system in non-steady state regime, where the diffusion depends on position and time. In this local form of conservation the interactions of atoms like chemical reactions or reactions between different sites in crystals, etc. are neglected/prohibited.

$$\frac{\partial \rho}{\partial t} + \mathrm{div}\vec{J} = 0, \tag{2}$$

where div is the divergent operator.

From the combination of Fick's I equation and the above introduced equation of continuity takes shape Fick's II equation as follows:

$$\frac{\partial \rho}{\partial t} = \mathrm{div}\left(\hat{D}\mathrm{grad}\rho\right) \tag{3}$$

In isotropic system and cubic crystals or in amorphous media the $\hat{D}$, diffusion coefficient tensor, becomes a simple scalar *D* in Fick's first and second equations respectively as follow. Fick's I law turns into:

$$\vec{J} = -D\mathrm{grad}\rho \tag{4}$$

and for the sake of simplicity in case when the concentration changes only in direction *x*:

$$J = -D\frac{\partial \rho}{\partial x} \tag{5}$$

Fick's II law turns into:

$$\frac{\partial \rho}{\partial t} = \frac{\partial}{\partial x}\left[D\frac{\partial \rho}{\partial x}\right] \tag{6}$$

Further simplification is permitted as long as the diffusion coefficient is independent of the concentration:

$$\frac{\partial \rho}{\partial t} = D\frac{\partial^2 \rho}{\partial x^2} \tag{7}$$

The above equation is a second order, linear partial differential equation. Initial and boundary conditions are essential to solve it.

I.1.2 Boltzmann transformation

By the introduction of the variable $\lambda = x/t^{1/2}$ the above equation (Fick II) turns into a simple differential equation, which one can be used if and only if the initial and boundary conditions depends on λ only. So thus the Boltzmann transformation transforms Fick's second partial differential equation into a simple differential equation:
Since

$$\frac{\partial}{\partial x} = \frac{d}{d\lambda}\frac{\partial \lambda}{\partial x} = \frac{1}{\sqrt{t}}\frac{d}{d\lambda} \tag{8}$$

and

$$\frac{\partial}{\partial t} = \frac{d}{d\lambda}\frac{\partial \lambda}{\partial t} = -\frac{\lambda}{2t}\frac{d}{d\lambda} \tag{9}$$

Fick's second equation–which is a second order, partial differential equation–turns into a simple second order differential equation:

$$-\frac{\lambda}{2}\frac{d\rho}{d\lambda} = \frac{d}{d\lambda}\left(D\frac{d\rho}{d\lambda}\right) \tag{10}$$

The solution of this equation depends only on $\lambda = x/t^{1/2}$. It follows that a plane with constant concentration shifts proportionally with the square root of time, i.e. $x \sim t^{1/2}$.

However this so-called parabolic law (since $x^2 \sim t$) sometimes is disobeyed. For these cases a general power function could describe the present relation as follows:

$$x(t) \sim t^{k_c} \tag{11}$$

where k_c , the kinetic exponent, and its deviation from 0.5 shows the deviation from Fickian kinetics. [4,5,6,7,8]

I.1.3 Stress & diffusion

The rise of stress effects in any material could be originated to three basic phenomena: thermal expansion, mismatch of lattice constants and diffusion

Thermal expansion: Come from the natural reaction of materials to the change their size when the temperature is changing in their surroundings. The rate of expansion can be quite different for two different materials in a given material made of more than one component. Accordingly, with the rising temperature at (and around) the borderline of the components stress appears.

Mismatch of lattice constants: Crystalline structures of different materials partly characterized by their lattice constant rarely share equal magnitude. Around the interface, where, for the sake of simplicity, two different crystal structures join together the lattice constant of one of them must be expanded while the other one must be compressed in order to create the bonds. Such a distortion in a certain thickness could easily lead to local stress effects even if these effects diminish in larger scale.

Diffusion: Each atom possesses different inner properties which characterize themselves, such as the number of protons, neutrons or their size, volume. In general, in diffusion couples one of the participants' atoms move orders of magnitudes faster than the other. If we also take into account the possible volumetric differences of the atoms one can expect a resultant volume transport from one side to the other. Considering these facts it seems reasonable expecting the rise of stress, as it is illustrated on Figure 1.

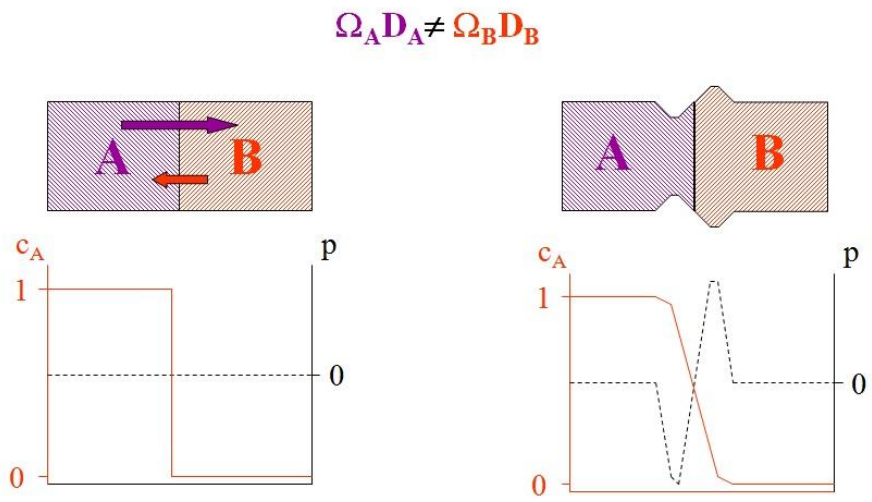

Figure 1 Illustration of the effect of diffusional stress development in the initial state (left panel) and in a later developed state (right panel). Here c_A and p stands for the change in the concentration of element A and the pressure or stress that changes due to the diffusion respectively Ω_i and D_i are the molar volumes and the diffusion coefficients of element A and B respectively. [9]

Stephenson for a one-dimensional, isotropic n component system – derived a set of coupled differential equations for the description of diffusion-induced stress development and stress relaxation [10,11]:

$$\frac{DP}{Dt} = \frac{2E}{9(1-\nu)}\left[\sum_{i=1}^{n}(\Omega_i \nabla j_i) - \frac{3}{4\eta}P\right] \tag{12}$$

$$\nabla v = -\sum_{i=1}^{n}(\Omega_i \nabla j_i) - \frac{3(1-2\nu)}{E}\frac{DP}{Dt} \tag{13}$$

$$\frac{D\rho_i}{Dt} = -\nabla \mathrm{j_i}, \qquad \mathrm{i} = 1, \dots, \mathrm{n} \tag{14}$$

where D/Dt denotes the substantial derivative, v is the velocity field required to determine the spatial evolution of the system (Kirkendall velocity), P is the pressure, t is the time, E is Young's modulus and η is the shear viscosity. Furthermore, Ω_i; ρ_i and j_i are the molar volume, the material density and the atomic flux of component i, respectively. By introducing the atomic fraction c_i instead of ρ_i is, using, $c_i = \rho_i/\rho$ where $\rho = \sum_{i=1}^{n}\rho_i$ is the total material density, the above equation becomes (since describing the system with c_i is much more reasonable):

$$\frac{Dc_i}{Dt} = -\frac{1}{\rho}\nabla j_i + \frac{c_i}{\rho}\sum_{k=1}^{n}\nabla j_k\,, \qquad i = 1, \dots, n \tag{15}$$

and so the atomic flux is given by

$$j_i = \rho \left[\Theta_i D_i^* \nabla c_i + D_i^* \frac{c_i \Omega_i}{RT} \nabla P \right], \quad i = 1, \dots, n \tag{16}$$

Here D_i^* is the tracer diffusion coefficient, R is the molar gas constant, T is the absolute temperature and Θ_i is the thermodynamic factor. Since only ideal binary system was considered, $\Theta_i = 1$.

Note that ignoring the stress effects, Stephenson's model is equivalent to Fick's: equation (14) and equation (16) without the second term give actually Fick's second law.

According to Boltzmann's transformation a plane with constant concentration shifts proportionally with the square root of time.[4,12] – or in other words the solution of Fick's second equation as it was discussed previously results in the parabolic shift of planes with constant c_i: $x_p^2 \propto t$ or $x_p \propto \sqrt{t}$, where x_p denotes the position of the monitored plane. Thus Stephenson's model is suitable to investigate how the stress effects influence the diffusion kinetics.

Previous experiments and theoretical approaches has already faced with the problems and the importance of stress effects, revealed some aspects and their possible handling in solid state reactions [13,14,15,16,17,18,19] such as e.g. the recent experiments of Schmitz et al. [20] pointed out that the intermixing rate could strongly be effected by stress, but surprisingly the parabolic growth rate is preserved. Schmitz et al. explained it by the switching between the Darken and Nernst–Planck regimes forced by the diffusion-induced stress.

During the intermixing by the net volume transport, by the difference in the intrinsic diffusion coefficients or by the possible change in the specific volumes if a new phase appears, stress-free strain evolves. Consequently stress develops within a certain characteristic time, leading to a steady state, which one can also relax within a characteristic time [21,10]. Due to terms proportional to the stress gradient in the atomic flux (see previously in Stephensons's Eqs.), the kinetics is obviously expected to differ from "pure diffusional" (Fickian or parabolic) type in the transient stages.

In the steady state – when the stress field remains roughly the same – even if the kinetics can remain Fickian, the intermixing rates can still differ considerably from the stress-free case. In the above referred article [20] it was shown experimentally that stress may have an easily measurable influence on the intermixing rate in spherical nanostructures but the diffusion kinetics still remains Fickian in time. The change in the intermixing rate was explained by the shifting of the system from the Darken to the Nernst–Planck regime triggered by the diffusion-induced stress.

We can separate the time evolution of the stress effect due to diffusion into four different stages as it follows [21,10,11]:

$$\text{(i) } t < t_{Qss} \text{ , (ii) } t_{Qss} < t < t_r \text{ , (iii) } t \approx t_r \text{ and (iv) } t \gg t_r. \tag{17}$$

where t_{Qss} is the time necessary to develop a steady-state stress distribution and t_r is the stress relaxation time of "pure" Newtonian flow determined by the second term in Eq. (12). Supposing that in a stressed sample the sum of the divergences of the atomic fluxes are negligible, Eq. (12) becomes

$$\frac{DP}{Dt} = -\frac{E}{6(1-\nu)\eta}P \tag{18}$$

and its solution is $P = P_0 exp\left[-\frac{E}{6(1-\nu)\eta}t\right]$, where P_0 is the value of the pressure at the beginning of the observation of the relaxation. The relaxation time, t_r, is the time necessary for the pressure / stress to decreases to the eth part of its initial value ("e" is the base of the natural logarithm):

$$t_r = 6(1-\nu)\eta/E. \tag{19}$$

I.1.4 Diffusion asymmetry

Our efforts investigating a diffusion couple can be easily discouraged if we try to apply the above mentioned Fickian, concentration independent diffusion coefficient in all cases. Why would we think that two different materials, with different physical and chemical properties will react the same way under the same conditions, such as the diffusion of materials in different matrixes? It doesn't exclude the possibility of such situation where it could be true but highlight the existence of such phenomenon which would result in concentration dependent diffusion coefficients. In a bilayer system which one is made of pure A and B material not only the diffusion coefficients could differ from one another but their relations to the change in the concentration as well:

$$D_A = D_A^0 exp(m_A c_A) \tag{20}$$

$$D_B = D_B^0 exp(m_B c_B) \tag{21}$$

where D_A^0 and D_B^0 are the diffusion coefficients of the pure A and B material, m_A and m_B define the strength of the concentration dependence, while c_A and c_B are the concentration/composition of the elements A and B.

By introducing the parameters $m'_A = \log_{10} e(m_A)$ and $m'_B = \log_{10} e(m_B)$, where e is the base of the natural logarithm, we can get the following equations below:

$$\log_{10}\left(\frac{D_A}{D_A^0}\right) = m'_A c_A \tag{22}$$

$$\log_{10}\left(\frac{D_B}{D_B^0}\right) = m'_B c_B \tag{23}$$

m' gives the ratio of diffusivities in the pure A and B matrixes. If e.g. $m'_A = 4$, the A atoms move 10000 times faster in the A matrix than in the B. The parameter m' had been introduced by Erdélyi Z, et al. in ref [22].

I.1.5 Reactive diffusion

The development of these new materials very often includes the chemical reaction of solids with another solid material.

Since we work with several systems which ones are actually reaction couples of multiphase binary systems it seemed to be rational to describe the phenomenon of reactive-diffusion in a few words. As its name suggests this process includes two main steps: the diffusion of the participants and their chemical reaction.

However the nucleation that takes place at the very beginning of the process when the participants meet at a single interface, its role in the growth can hardly gain any significant role since its volume is so small compared to the latter layer growth. According to the literature these initial volumes of the compound material that already possess all the physical and chemical properties of the bulk material ranges from as small volumes as a few nanometer. These initial volumes or thicknesses have been identified for different material with the help of different kinds of electron microscopy, Rutherford backscattering, X-ray diffraction and ion mass spectrometry amongst other methods as it is considered in detail in the references of the book of Dybkov [23].

The term reactive-diffusion itself indicates that the process takes place in two subsequent steps

1) Diffusion of atoms of the participants, through the appeared bulk compound (after the process of nucleation), in different direction.

2) Chemical transformation of the diffusing atom of one of the participants and the surface atom of the other one at one of the two interfaces of the growing compound layer.

The latter on includes the following steps:

a so called external diffusion that transfers the atoms of a given species through the interface between the different phases [24,25**]**

a) rearrangement of the atomic orbitals of the participants, so thus it fits for the newly growing product layer

b) the reconfiguration of the crystal structure resulting the bulk structure of the product layer

Since the process happens at two sites of the growing new alloy/compound material the contribution to the growth of the product layer is actually independent of each other, thus equal contribution of the two sides to the total layer growth is not necessary.

As a part of the better understanding of this phenomenon of reactive-diffusion various models and calculations were proposed by numerous members of the field. These approaches assume that the atomic diffusion at the interface of the growing layer is forced to overcome a potential barrier that tends to slow down the diffusion flux, by restraining the diffusing atoms to enter into the new phase (see [23,24,25] and the references therein). In some approach this problem is solved by introducing reaction constants that include the reactions taking place at the interface and the diffusion of atoms through the given phases. Whatever this process is controlled by the reaction at the interface or the diffusion the kinetics of the layer growth will be linear or parabolic respectively.

I.1.6 Diffusion in Si

Previous investigations of Bracht, Werner, Valenta, Voss and Mehrer, amongst many others revealed many aspects of the diffusion in semiconductors, especially in Si and Ge. Their researches concerned not just the diffusion of impurities in these materials but their self-diffusivities as well ((see e.g. [26]).

In one of the work of Bracht and Brotzmann one can find a broad summery of foreign atom and self-diffusivities and their comparison.Their summarized results can be seen in Figure 2:

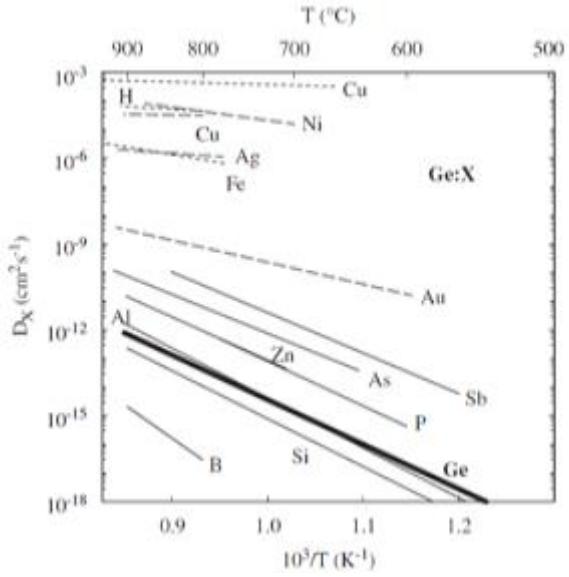

Figure 2 „Temperature dependence of the diffusion of foreign atoms in Ge (thin lines) compared with self-diffusion (thick line). Details and references to the data are given in the text. Solid lines represent diffusion data of elements that are mainly dissolved on substitutional lattice sites. Long-dashed lines (——) illustrate diffusion data of hybrid elements, which are mainly dissolved on substitutional sites, but diffuse in an interstitial configuration via the dissociative mechanism. The short-dashed lines (- - - -) indicate the diffusion of mainly interstitial dissolved elements. The upper short-dashed line shows the diffusivity deduced for interstitial Cu" [26]

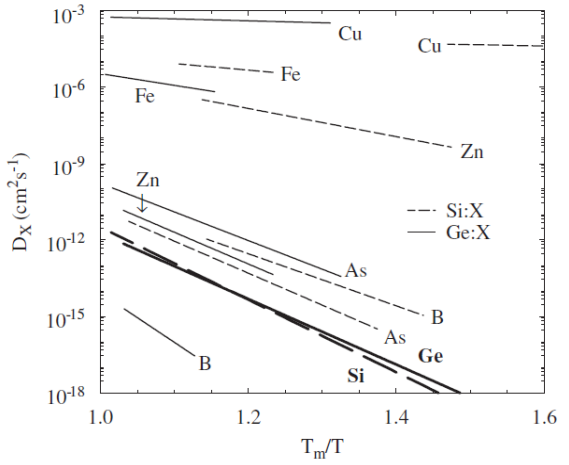

Figure 3 "Representation of self- and foreign-atom diffusion in Ge (Tm = 1210 K) and Si (Tm = 1685 K) as function of the homologous temperature Tm/T. The solid lines show diffusion data for Ge and the dashed lines for Si." [26]

From Figure 2 it is clear, that except the Si and the B all the foreign atom diffusivities exceed self-diffusion in Ge, while in Si, where the self-interstitials and vacancies play a role with

more or less the same weight in the self-diffusion, the foreign atom diffusivities are higher in all case

In Figure 3 one can see the comparison between self- and foreign-atom diffusion in Ge and Si as function of the homologous temperature T_m/T [melting temperatures of Ge (T_m = 1210 K) and Si (T_m = 1685 K)].

From the above Figure 3 we can conclude that the self-diffusion coefficient of Ge and Si are in the same magnitude that suggests similar self-diffusion mechanisms. In case of Cu and Fe as the results clearly show that they are in the same magnitude whatever we measure their diffusivities in Si or Ge. While in case of Zn and B there is a clearly visible difference. In case of Zn it was explained by the difference in the mechanisms that control the diffusion of this material in Si and Ge. In Si, Zn diffuses via interstitial–substitutional exchange mechanisms while in case of Ge it does by vacancy mechanism. However B acts as a shallow acceptor in both materials it diffuses much slower in Ge than it does in Si. The reason for this behavior is that B diffuses via self-interstitials (the kick-out or interstitial mechanism) while this mechanisms play hardly any significant role in Ge self-diffusion.

Another aspect of the diffusion in this system appears when we investigate the dependence of their diffusion to the concentration. It has been shown in $Si_{1-x}Ge_x$ alloys that the diffusion coefficients of these two elements are in agreement when we measure them in pure Si, however with increasing Ge content their diffusivities tend to differ and it is the greatest in pure Ge [27]. Since Si diffuses through intersticial and vacancy mechanism similar then the increasing Ge content in this SiGe alloy tends to increase the jump efficiency of Ge and so it becomes more and more successful. The obtained further data suggest a slightly lower activation enthalpy for Ge diffusion as well compared to Si.

The dominance of diffusion, mediated via vacancy mechanism, thus favors Ge. This behavior is supported by other investigations concerning diffusion asymmetry, where the sharpening or intermixing of a given binary system depends on the strength of diffusional asymmetry (m') that defines the difference in orders of magnitude in the diffusion of a given atom in two different matrices.

I.2 Metal Induced Crystallization (MIC)

It is reported and studied widely that the crystallization temperature of silicon in contact with metals reduces significantly, the phenomena is called MIC i.e. Metal Induced Crystallization. This can be related to two procedures: i) Template nucleation, i.e. in case of materials forming silicides, such as Ni, the forming silicide plays the role of the template for the latter nucleation of the crystalline silicon [28]. ii) Metal-induced bond weakening, which had been reported in cases of low melting materials such as Al [29,30]. When Al gets in contact with the

amorphous silicon the bonds of a-Si weaken at the interface resulting in so called free Si atoms which ones have larger mobility. These Si atoms can easily move into the grain boundaries of the metal counterpart and wet them. The crystallization will be initiated on these sites at a lower temperature.

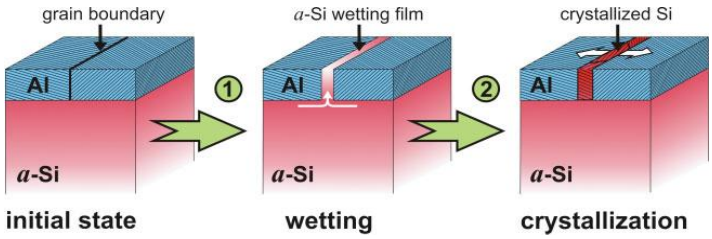

Figure 4 Schematic draw of MIC mediating through the phenomenon of grain-boundary diffusion and the metal-induced bond weakening as it is published in [31]

I.3 Grain-boundary diffusion

Till now our system was restricted to ideal conditions where the diffusion could flow in the way as it does happen in single crystalline or amorphous media. However in most cases e.g. in metals where the bulk material is built up by smaller parts called grains the diffusion can occur orders of magnitude faster than in case of volume diffusion. In case of poly- or nanocrystalline materials concerning grain-boundary diffusion, three different kind of kinetics can be distinguished following Harrison, namely A, B and C kinetics.

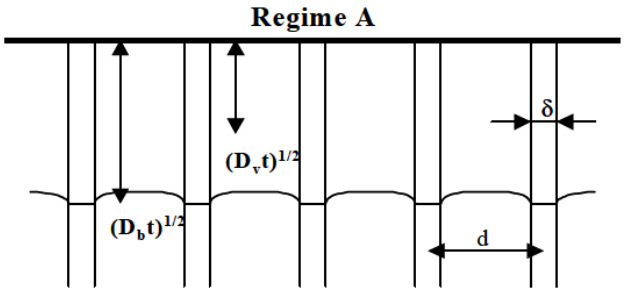

Figure 5 Schematic illustration of regime A after Harrison, where d is the grain-boundary size, $(D_b t)^{1/2}$ and $(D_v t)^{1/2}$ represent the grain boundary and the volume diffusion respectively. Here the diffusion can be characterized by an effective D_{eff} diffusion coefficient that comes from the combination of volume and grain-boundary coefficients. [32]

In Regime-A for long enough annealing times or for small enough grain sizes the diffusion fields, considering diffusion into grains, are overlapping. The system acts like a homogeneous media from the point of view of diffusion which one in turn can be characterized by an

effective D_{eff} diffusion coefficient. It comes from the combination of volume and grain-boundary coefficients:

$$D_{eff} = fD_{gb} + (1 - f)D_v \tag{24}$$

where f is the fraction of atomic sites.

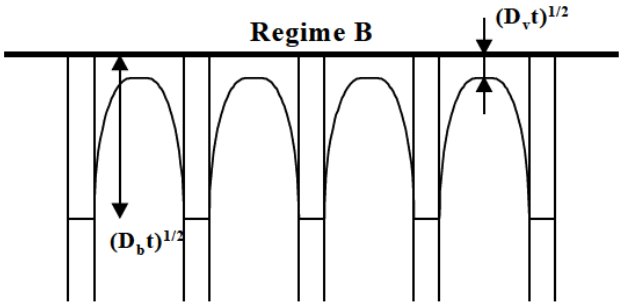

Figure 6 Schematic illustration of regime B, after Harrison, where $(D_b t)^{1/2}$ and $(D_v t)^{1/2}$ represent the grain boundary and the volume diffusion respectively. Here the volume diffusion length is significantly shorter than the grain-boundary diffusion length. Sothere is no uniform diffusion front line, but there is diffusion into the grains. [32]

In Regime-B the volume diffusion length is significantly shorter than the grain-boundary diffusion length. So this there is no uniform diffusion front line.

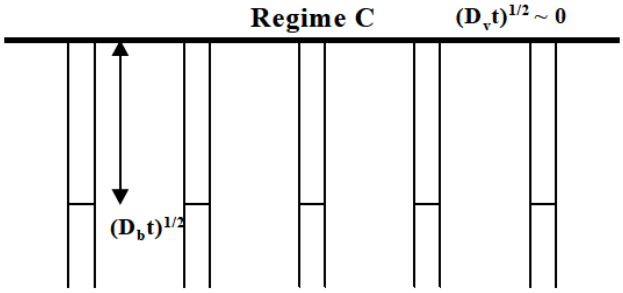

Figure 7 Schematic illustration of regime C, after Harrison, where $(D_b t)^{1/2}$ and $(D_v t)^{1/2}$ represent the grain boundary and the volume diffusion respectively. Here the diffusion from grain-boundaries into grains is insignificant and so the diffusion takes place only in grain-boundaries. This regime can be characterized by one diffusion coefficient again. [32]

While in Regime-C the diffusion from grain-boundaries into grains is insignificant and so the diffusion takes place only in grain-boundaries. This regime can be characterized by one diffusion coefficient again.

I.4 Surface Segregation

The rearrangement of atoms in a given e.g. binary alloy material between the surface and the bulk that results in different composition at the surface compared to the bulk is called surface segregation.

The phenomenon have been discussed in details since the nineteenth century (by J.W. Gibbs [33]); many scientists took a part in the better understanding of this phenomenon by performing numerous experimental and theoretical approach in order to reveal another pieces of this scientific puzzle.

Generally we can say that during the segregation the uppermost several atomic planes are considered to differ from the bulk material and so take a part in the process, affected by the phenomenon.

According to the theoretical approach the simplest one is the monolayer model [34], according to the general monolayer model only the upmost one atomic layer is influenced, however it is worth mentioning here that by creating any surface not just the bonds of the atoms at the surface but the bonds in the nearby few deeper atomic layers will be altered as well. In those cases thus, when the segregation affect more than one layer at the surface a multilayer model can be applied.
For both the monolayer and the multilayer approach there are several theoretical calculations performed in previous investigations [35,36,37,38,39,40].
Many of these models considering segregation based upon a broken bonds model. It means that the segregation is mediated through the existence of broken bonds at the surface. Since segregation can appear not only on the surface but at grain boundaries as well. However since the amount of these broken bonds are lower in case of grain boundaries the effect of segregation at these sites is considered less pronounced.

Considering ΔH as the segregation energy, the segregation can be separated generally in three components:

$$\Delta H = \Delta H_{tens} + \Delta H_{chem} + \Delta H_{size} \quad (25)$$

where ΔH_{tens} corresponds to the effect of the surface tension, ΔH_{chem} to the chemical effect while ΔH_{size} takes into account the difference in the size of the constituents [33,40,41,42].

The latter one is usually negligible; its role can be considerable only in that case when the previous two effects can compensate each other.

Chapter II

Experimental techniques & Tools

II. Experimental techniques & Tools

This chapter reports on the experimental techniques and tools used in the experiments, performed in the framework of this thesis, describing each one of them and the principles behind. In all of the experimental investigations, the reliable and efficient vacuum system was essential, since the efficiency of our vacuum system can strongly affect the quality of our results. The lower the pressure in our experimental chamber the cleaner it is, considering the contamination of the samples during and „before" the experiments. Since contaminations can affect a given sample behavior, thus it is a very crucial point of any experiment from the very beginning to either minimize their presence or consider them when interpreting the results. For this reason inside the chamber the ultra-high vacuum condition especially for surface analytical techniques–such as XPS, AES, STM or LEED–where the information is originated from the topmost few nm of the sample is critical. At lower vacuum levels contamination of , especially, Oxygen or Carbon, can prevent us to obtain any valuable information from the surface.

II.1 Sample preparation methods

Thickness of thin films ranges from one monolayer to several tens or hundreds of nanometers. The processes creating them can be categorized, depending on the behavior of the methods, into two sets such as chemical and physical methods. This time, considering the finite capacity of this work it is recommended to restrict the shortly summarized description of the possibly techniques only on the physical methods; especially as these methods were used to prepare the samples in the framework of this work.

It is worth mentioning here that thin films whatever method took place in their production gained a foothold in a wide range of applications like integrated circuits, screens and displays, magnetic data storage devices, optical tools, solar cells and X-ray mirrors, however these examples do hardly cover the full potential of this field. Almost each and every aspect of our life has already been affected by their presence and their influence is growing day by day.

The physical methods creating thin films can be sorted in two main groups, namely sputtering and evaporation.

II.1.1 Sputtering

During this process within a vacuum chamber under high or ultrahigh vacuum conditions (in case of our sputtering system the possibly reachable base pressure within the main chamber is in the range of ~10^{-7} mbar) and attacked by bombardment of ions. These ions originated from

the plasma of a given high purity (99.999%) noble gas created by the DC voltage applied to the target.

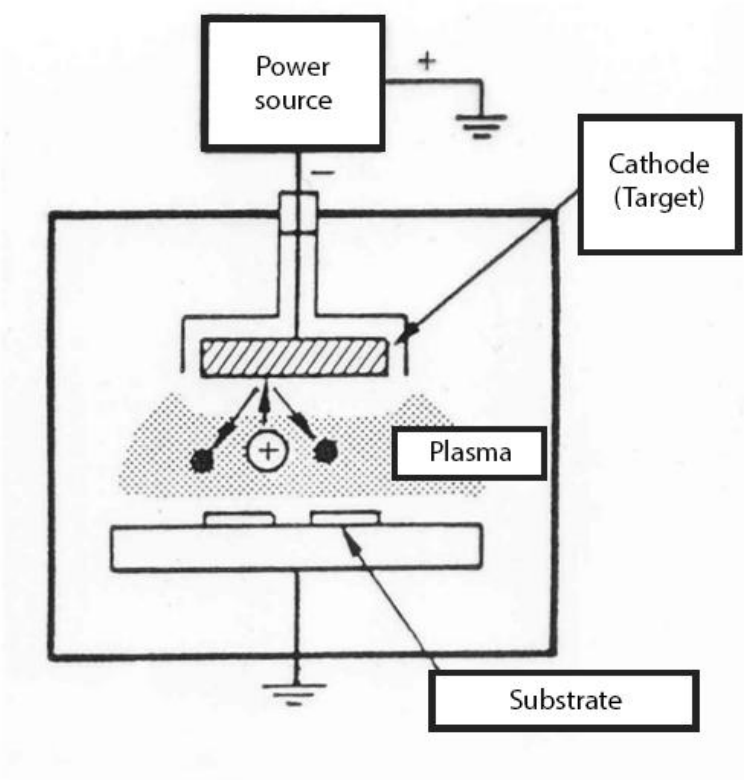

Figure 8 Schematic figure of a theoretical sputtering system indicating the path of the bombarding ions and the sputtered particles.

In order to maintain the noble gas plasma the noble (Argon) gas pressure within the chamber is settled around 10^{-3} mbar (by its dynamic flow). The incident ions will participate in several collisions in the upper few atomic layers of the target meanwhile its energy will be transferred to the atoms. This energy, at the end of the process, will be focused on a surface atom which one in turn will be ejected. The sputtered parts are natural in general.

Since the bombarded target heats up its cooling is recommended. By attaching magnets under the targets we can increase the efficiency of the sputtering and stabilize the plasma itself over the targets too.

The vertical position of the sample holder can be changed within 5-8 cm, measured from the surface of the targets (diameter of 5 cm in our system). The homogeneous area of the deposition is around 2-3 cm^2. For in-situ heat treatments the sample holder can be supplemented with an annealing system as well. The highest reachable temperature is 800^oC. The power source of the magnetron can be settled within 0-400 Watts.

Multiply samples were prepared for both the Cu-Si and for the Ni-Si experiments by magnetron sputtering in Debrecen, Hungary. During the deposition we created a $P = 5 \times 10^{-3}\ mbar$ pressure of dynamic Ar gas flow inside the chamber at which pressure a plasma discharge is generated just above the target material plates. The Ar ion bombardment attacks the target, from which the atoms are ejected and move further toward the substrate in the vacuum, which is about 5-8 cm away from the target positioned normally to it.

In order to determine the deposition rate before the preparation of the real samples we deposited layers of the given target on glass substrates for 300 seconds each and measured the depth by profilometer (see in II.4.1). For each deposition rate measurement several profilometer measurements were performed to gain the right value.

Depositing samples by magnetron sputtering depending on the target material could be not only reasonably fast but even cost effective as well, considering the fact that one can load multiply substrates into the preparation chamber, from which each one of them is large enough for multiply measurements. The available number of samples which can be prepared in this way in one deposition circle is limited only by the homogeneous area of the deposition. The magnetron sputtering machines in Debrecen are purpose built, highly flexible tools.

Two types of samples were prepared by magnetron sputtering for the investigations performed in the framework of this thesis: i) Si-Cu bi- and trilayers (Cu/a-Si/substrate, Cu/a-Si/Cu/substrate, a-Si/Cu/a-Si/substrate); ii) Ta/a-Si/Ni/a-Si/Ta/substrate (for detailed description of the samples see Chapter III). In the machine in which these samples were sputtered 3 individual targets can be used simultaneously, shielded with shutters. The optimal position can be checked through the viewing port. The sample transition between the targets and the control of the shutters can be achieved in two ways: manually or by computer controlled pneumatic valves and step motor. The preparation chamber also contains vacuum gauges, gas management, and 3 magnetrons, optionally quartz crystal monitor and an in-situ heated sample holder. The magnetrons are placed on the bottom of the stainless steel chamber at an angle of 120^{o} from each other.

We applied 40 Watts on the power sources of the magnetrons for each targets during the sample preparation process of the Si-Cu or the Si-Ni systems, except for the tantalum mirror layers, between which the a-Si/Ni/a-Si trilayer were deposited, in which case we used 60 Watts. Since the lower the power one applies the higher the sample preparation accuracy is then we tried to increase our accuracy as much as we could by these settings. In our sputtering system 40 watts are the available lowest sputtering power so thus the lowest deposition rate as well. The samples were deposited at ambient temperature in each case. The base pressure in the sputtering chamber was maintained by a two-step vacuum system. The $P = 10^{-7} mbar$ base pressure is achieved with the combination of a turbomolecular pump and a rotary pump mounted on the side wall of the chamber.

Before the introduction of the Silicon substrates were cleaned in sequential steps of cleaning in distilled water in ultrasonic bath and later in ethanol or chloroform in order to get rid of all the possible dust or any other surface contaminants.

II.1.2 Evaporation

The method of evaporation can be further separated into subgroups:

- Joule heating (or Ohmic heating or Resistive heating)
- Heated by electron bombardment
- Heated by laser

The process of joule heating can also be further separated into subgroups:

- Direct methods
- Indirect methods

In case of the direct heating we pass a given current (which partly defines the resultant layer's thickness) through the material (meant to be evaporated) that is connected directly to the electric circuit. Meanwhile in case of the indirect methods the ceramic or graphite sample holder is heated up through a metallic wire (with high melting point).

The sample preparation for Silicene samples were performed in Marseille, France. The experimental chamber in this laboratory is divided in 4 main parts:

- Introduction Chamber
- Cleaning Chamber
- Deposition/Annealing/AES/LEED Chamber
- STM Chamber

For each main chamber except the introduction chamber the possibly reachable vacuum is in the ultra-high vacuum range, $P = 10^{-9} - 10^{10}\, mbar$, and achieved via a 3 step vacuum system with 3 separate ion pumps, two turbomolecular pumps and a rotary pump. The 4 main chamber is separated through gates thus in the chambers of STM and AES the vacuum is usually maintained only by the ion pumps, meanwhile in those chambers where the pressure can vary highly during the sample introduction and the ion bombardment, due to the airing and the Ar gas inlet, there are the turbomolecular pumps, the rotary pump and the third ion pump mounted.

Since these techniques are highly surface sensitive, the very good vacuum condition is absolute necessary even for the in-situ sample preparation.

During the cleaning process we achieved a pressure of $P = 5 \times 10^{-5}\ mbar$ of dynamic flow of high purity Ar gas inside the chamber and settled the focus of the ion gun in a way that the Ar ions covered not only the surface of the Ag(111) substrate but its surrounding as well. After the ion bombardment we annealed the substrate to regain the (111) structure for the upper layers affected by the ion gun as after the bombardment they become amorphous. The applied annealing temperatures and times varied between 430°C – 530°C and 2 – 15 hours respectively for different experiments. The silicon was deposited by evaporation from a silicon wafer mounted in the same chamber as the AES system under the horizon of the sample translation path. In constant current mode, depending on the desired superstructure, we let from 8 to 12 A through the silicon wafer. During the deposition the current and the voltage were simultaneously monitored. Significant fluctuation or changes in them were not experienced.

II.2 X-ray Diffraction (XRD)

Diffraction can appear in case of all kind of waves for sound waves or electromagnetic ones such as X-rays just as well. In the last several decades or so these XRD patterns have been identified and collected and are available. X-rays are actually electromagnetic waves just like the visible light however they situated between the ultraviolet light and the gamma rays because of their small wavelength and high energy.

It is well known that when a wave (whatever its origin) and an object with a periodicity similar in length to the incidence meet then the phenomenon of diffraction is observed. The wavelength of X-ray ranges from 10^{-9} to 10^{-12} m and so these distances are similar to those measured in crystalline structures. In turn working with X-ray can serve with information about any crystalline structure in hand through diffraction patterns that follow Bragg's law. According to the common description of the phenomenon when the travelling wave meet an obstacle and the wavelength of this beam has similar magnitude as the object it will bend and in case of specific incidences the reflected waves will interfere fully constructively. The relation between the wavelength, the incidence and the dimension of the obstacle is determined by the Bragg-equation:

$$2d \sin \theta = n\lambda \tag{26}$$

where d is the dimension of the obstacle e.g. the distance of the lattices in crystalline structures, θ is the incident angle and λ is the wavelength of the probing beam.

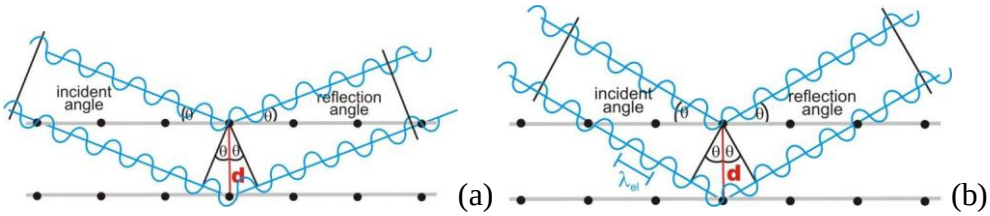

Figure 9 Phenomenon of diffraction for two different incident angles on a crystalline structure; (a) complete destructive interference, (b) complete constructive interference (for denotations see eq. 26). [43]

Based upon the phenomena of diffraction numerous different experimental techniques had been developed and used routinely in material science. Since, depending on the applied technique, characteristic information can be gathered about the periodically organized bulk or surface, such as lattice parameters or orientation of different the surface structures, this is perhaps one of the most commonly exploited phenomena of physics for material science. The more specific applications of the phenomena will be discussed in details in the chapter of the experimental techniques.

The X-ray machine in Debrecen we used to study the Si-Cu system has a Cu K alpha X-ray source and was applied in Bragg-Brentano geometry.

II.3 X-ray standing wave methods

II.3.1 Synchrotron light sources

The measurements by X-ray standing wave methods required the application of synchrotron light sources. Besides several others, the synchrotron radiation has two advantages, which were crucial for us, against the X-ray used in laboratory machines: the adjustable beam energy and the brilliance. The brilliance is the photon flux per unit area [44]. A synchrotron source is extremely bright compared to the X-rays used for example in a hospital. However creating such a bright X-ray source is much more complicated than building a more or less simple X-ray tube. For this you need a combination of different accelerators, where the huge circular shaped storage rings maintain the pre-accelerated electrons in their circular path using magnetic fields forcing the moving electrons to change their directions and so emit energy in turn.

The storage ring is like a tube where the electrons circle at high speed. Within the tube the pressure is low (~10^{-10} mbar). As the electrons travel in this ring and produce X-rays and at given points of the storage ring we find the beam lines, where these emitted X-ray beams get out and pass through towards different experimental setups.

During our experiments we worked in Helmholtz-Zentrum Berlin für Materialien und Energie (HZB) at the KMC-2 beamline.

The storage ring in the Helmholtz-Zentrum Berlin für Materialien und Energie (HZB) a third generation synchrotron radiation source in Germany, where we performed our experiments on Ni/a-Si samples, contains numerous beamlines and offers various possibilities of experimental opportunities with good energy resolution.

Figure 10 Zentrum Berlin für Materialien und Energie (HZB) [45]

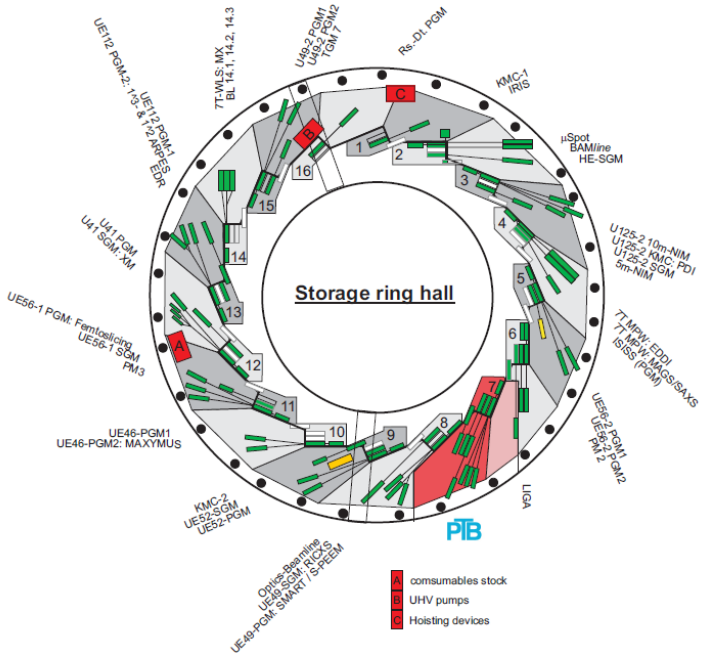

Figure 11 Schematic figure of the work stations of Zentrum Berlin für Materialien und Energie (HZB) [46]

The KMC-2 beamline provides an experimental set-up for EXAFS and fluorescence measurements in the energy range of 4 keV – 15 keV. The intensity of the beam is stabilized by MOSTAB electronics. The beamline contains: a Si-PIN photodiode, a scintillation counter, an energy-dispersive detector and a 6-axis HUBER goniometer for reflectometry and X-ray diffraction measurements.

II.3.1 Grazing Incidence X-ray Fluorescence (GIXRF) in X-ray waveguide structure

The advantage of X-ray Standing Wave (XSW) techniques has already been discussed in detail in [47,48] and [49]. So here I would like to summarize shortly the basics of the technique only.

Since X-rays are highly penetrating radiations, thus the gathered information originates from a depth range of the sample. XSW based techniques, however, offer elemental depth profiling with nanometer resolution. One of the possible geometries is to put the sample layer in the space between two reflecting (mirror) layers. The trapped incident beam will be bounced back and forth on the waveguide mirror layers and interfere with itself, and so at specific incidences standing waves of the electric field form (see Figure 12).

The angles satisfying such conditions where we get different resonance modes can be written as it follows:

$$\Theta_m = (m+1)\pi/kW \tag{27}$$

where k is the absolute value of the propagation vector of the X-ray, W is the width of the cavity (distance between the waveguide layers) and m is an integer.

Since the interaction between the atoms and the X-ray beam is mainly electrical, then the square of the developing electric field at a given depth can be regarded as the intensity of the primary X-ray beam. When we place these layered materials - including an absorbing (in our case Ni) layer - between the mirror layers, then the fluorescence intensity is going to be proportional to the square of the electric field at the absorbing layer position and the fluorescence signal will come from that part of our structure where the absorbing layer and the anti-nodal part i.e. the electric field intensity of the XSW overlaps. [47,48,49,50,51,52]. In this way, changing the angle of the incidence, the tuning of the different modes of the XSW is possible and so the positions of the anti-nodal parts can be positioned to the depth of interests.

The square of the electric field generated by the incoming X-ray beam is therefore proportional to the intensity of the fluorescence signal as it is given as follows:

$$I(\Theta) = \int_0^L c(x)E^2(\Theta, x)\,dx, \tag{28}$$

where c is the atomic fraction of the material which we are interested in, E is the amplitude of the electric field, L is the length of the sample – including the waveguide layers, and theta is

the incident angle. On the basis of this equation, therefore, it is possible to calculate the fluorescence radiation intensity versus the angle of incidence, which provides the possibility to reconstruct the composition profile of the absorbing element. In order to use this formula, however *E* has also to be calculated. This is based on the application of Fresnel equations, modified to account for interface imperfections, which describe the reflection and transmission of an electromagnetic plane wave incident at an interface between two optically dissimilar materials. [53,54,55].

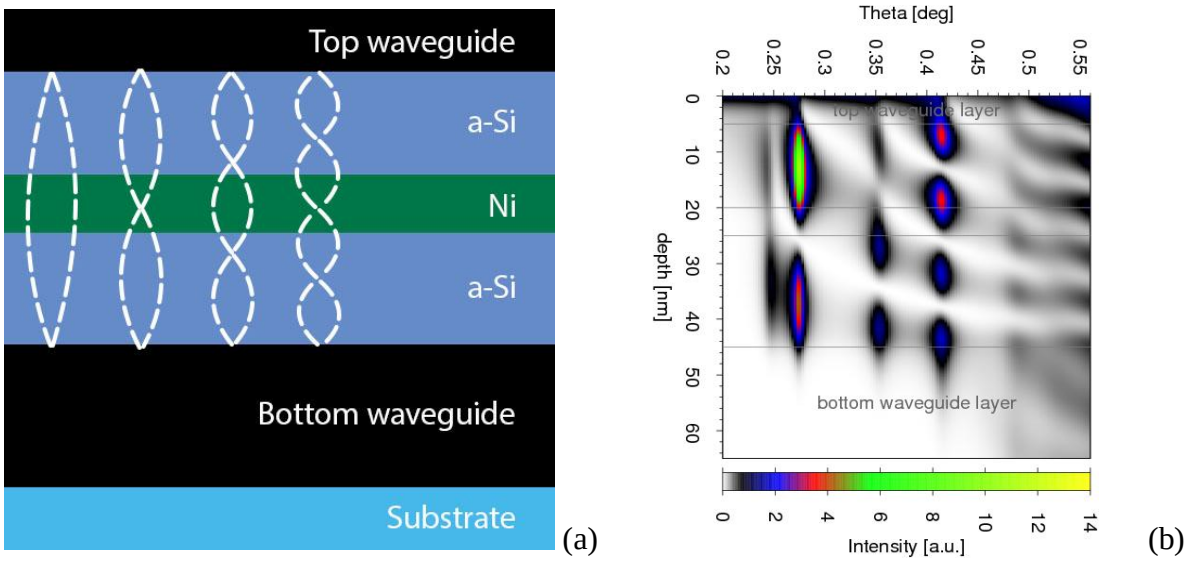

Figure 12 (a) Waveguide sample structure. The Si/Ni/Si trilayer is the 'sample to be investigated'. The schemes of the first four transversal modes of the electric field (TE) are also illustrated. (b) Intensity plot of the calculated electric field (photon energy: 8.40 Å keV). The different TE as a function of the angle of incidence is displayed.

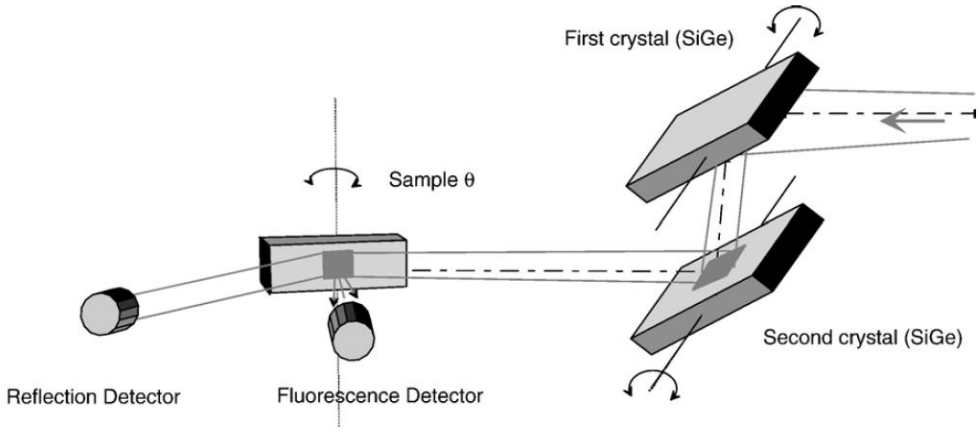

Figure 13 Schematic figure of the experimental setup of GIXRF measurements using Synchrotron radiation. [47]

Therefore, supposing composition profile, it is possible to calculate the electric field and so also the fluorescence intensity. The calculated fluorescence intensity curve can be compared to the measured one. By iterative fitting of the measured and simulated intensities, the composition profile can be reconstructed. The reconstruction software was developed by our group. [49]

II.3.2 Extended X-ray absorption fine structure (EXAFS) in fluorescence detection with XSW

When the energy of the incident X-ray photon equals or exceeds the ionization energy edge of an electron of an element the electron will be released, ejected from the atom. In the X-ray absorption spectrum this phenomenon is marked by an abrupt drop that is called the absorption edge. These edges are sorted by the quantum numbers of the electron in ground state.

The EXAFS is the oscillating part of the recorded X-ray absorption spectrum that starts from the absorption edge and finishes a thousand eV above. Structural information such as distances of the neighboring atoms from the central atom, number of neighbors and some properties of them can be extracted from this oscillating part. In brief a branch of chemical information becomes available with the help of this powerful probe.

The photoelectrons ejected from the absorber atoms and interfere with scattering centers in the surroundings, the neighbor atoms. The obtained EXAFS spectra are the result of the interference of the ejected and scattered photoelectrons. The nature of the interference, whatever it is destructive or constructive, depends on the distance and the atomic number of the neighbor atoms.

For the EXAFS, we are interested in the oscillations well above the absorption edge, and define the EXAFS fine-structure function $\chi(E)$, as [56]

$$\chi(E) = \frac{\mu(E)-\mu(E_0)}{\Delta\mu_0(E)}. \tag{29}$$

Here $\mu(E)$ is the measured absorption coefficient and in fluorescent detection

$$\mu(E) \propto \frac{I_f}{I_0} \tag{30}$$

where I_f is the monitored intensity of a fluorescence line associated with the absorption process and I_0 is the X-ray intensity incident on a sample, $\mu_0(E)$ is a smooth background function representing the absorption of an isolated atom, and $\Delta\mu_0$ is the measured jump in the absorption $\mu(E)$ at the threshold energy E_0. The primary quantity for EXAFS is then $\chi(k)$, the oscillations as a function of photo-electron wave number, where

$$k = \sqrt{\frac{2m(E-E_0)}{\hbar^2}} \tag{31}$$

with m the electron mass and $\hbar$ Planck's constant over 2π.

The different frequencies apparent in the oscillations in χ(k) correspond to different near-neighbor coordination shells which can be described and modeled according to the EXAFS equation

$$\chi(k) = \sum_j \frac{N_j f_j(k) e_j^{-2k^2\sigma_j^2}}{kR_j^2} \sin\left[2kR_j + \delta_j(k)\right] \tag{32}$$

where $f(k)$ and $\delta(k)$ are scattering properties of the atoms neighboring the excited atom, N is the number of neighboring atoms, R is the distance to the neighboring atom, and σ^2 is the disorder in the neighbor distance. Though somewhat complicated, the EXAFS equation allows us to determine N, R, and σ^2 knowing the scattering amplitude $f(k)$ and phase-shift $\delta(k)$. Furthermore, since these scattering factors depend on the Z of the neighboring atom, EXAFS is also sensitive to the atomic species of the neighboring atom.

To measure an absorption spectrum, one has to vary the energy of the incident beam. This would however change the electric field pattern. In order to gain information form a given depth one must keep, however, the electric field pattern constant. In order to achieve it simultaneous corrections of the incident angle were necessary to execute. Control software was used to provide this simultaneous energy scan of the monochromator and angular scan of the sample.

The thickness of the sampling volume was estimated to be of 2 nm. The position of the sampling volume could be changed by changing the transversal mode of the electric filed pattern. [57,58]

II.4 Secondary Neutral Mass Spectrometer (SNMS)

The removal of atoms from the solid surfaces due to the impact of energetic particles, is commonly called sputtering.

When a sample is bombarded by low- or medium energy ions originated from noble gas plasma, then at the surface it results in an ion-atom collision and cause atom-atom collision inside the target. If the transported energy is large enough atoms and molecules close to the surface can be ejected, while the ions of the primary beam can be backscattered or implanted in the target material. The ejected parts can be separated in two groups as charged and neutral

parts. Since in my thesis we used only the SNMS mode of the machine in Debrecen, accordingly I focus the attention mainly on the neutral ones.

Secondary neutral mass spectrometry is a routinely used analytical technique, exploiting the above phenomena, achieving quantitative surface and depth analysis in the last few decades. The ion bombardment and the latter post-ionization achieved by the low pressure noble gas plasma (Ar, Xe, Ne… etc).

Since in this technique the neutral components (mostly atoms and seldom simple molecules) are ejected by sputtering, and the ionization takes place separately the side effects (matrix effects) which rise in case of SIMS does not occur. Conducting and non-conducting samples can be treated identically. The latter one is provided by HFM (High Frequency Mode), which controls the amount of charge being transferred to the sample by periodically interrupting ion accelerating voltage between the sample and the plasma. With this procedure thus we can compensate the charging of the sample and this simple step allows the measurement of insulator samples. The sputtered neutrals are ionized in the plasma by electron impact and a fraction of them enters the ion optics located in front of the quadrupole mass analyzer. Accordingly the sputtered and post ionized species subsequently analyzed (by in our case a quadrupole mass spectrometer operating in the 1-340 amu range).

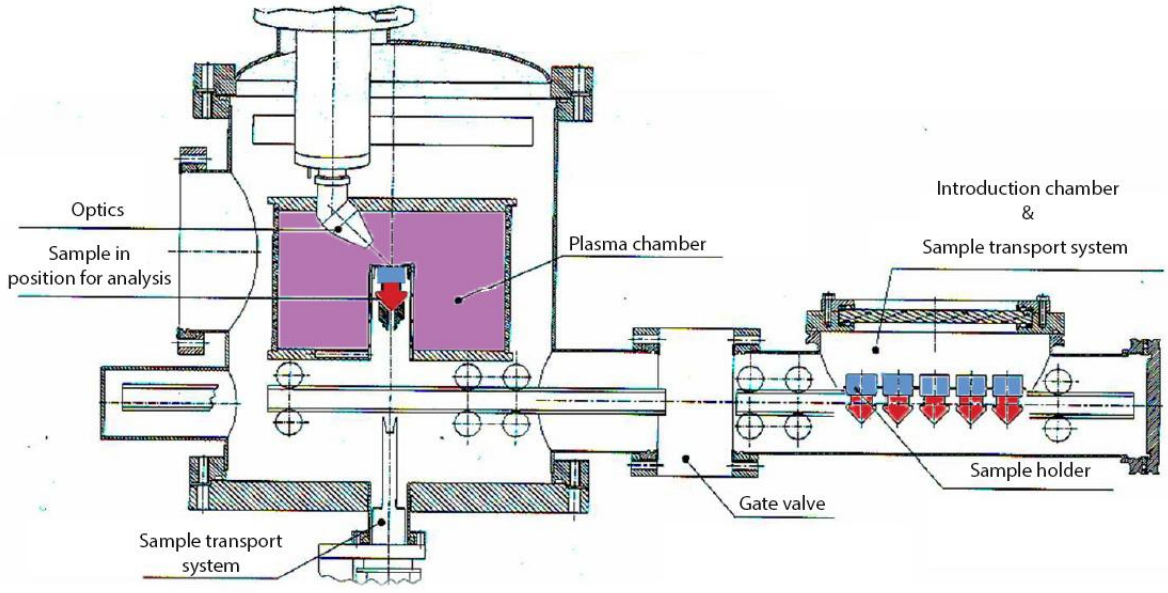

Figure 14 The INA-X SNMS system

With this system the thin film's structure, their stability, the development of interface reactions can be followed in nanometer depth resolution. This does not require special sample preparation compared to e.g. TEM analysis and relatively quick results can be gathered.

However, the technique is destructive (compared to e.g. an XPS measurement), accordingly multiply samples may be needed for certain (e.g. kinetics) investigation. Compared to XPS or AES where mainly the surface is analyzed by the ejected electrons, in case of SNMS the different species themselves are analyzed / detected by the mass.

SNMS measurements provide intensity versus sputtering time (raw) data; however, usually composition versus depth curves (composition profiles) are desired. The conversion of raw data is therefore a two-fold procedure: on the one hand calculation of composition from intensity is needed; on the other hand depth has to be deduced from sputtering time.

Basically two procedures exist to calculate the composition. The one uses standards with known compositions; this is a simple calibration method. This requires numerous samples for calibration and presumes that elements in the sample are known. The other is based on the knowledge of relative sputtering efficiency and the detection sensitivity for the given elements.

Basically, also two procedures exist for the sputtering time to depth conversion. The one is based on the knowledge of the sputtering rates of the elements. This is, however, a delicate problem since sputtering rate depends not only on the sputtered element itself but also on its local environment (composition). For this reason it is desired to measure the depth of the crater at different points of the measurement and to use these data for the conversion. A handy tool for this purpose is the profilometer (see next subsection), which is suitable not only to measure the depth of the crater but also to check the shape of the crater. The shape is a critical factor since reliable measurements require plan crater bottoms. [59,60,61,62]

II.4.1 Profilometer

The profilometer we used in Debrecen is an Ambios XP-1 profilometer. This is a contact profilometer in which a stylus (with ~2 microns radius) moves along a defined path on the sample following the changes of the surface. Thanks to the system small surface variations or steps, layer thicknesses, or the roughness of the surface can be easily determined, identified. The used low-force stylus working in the 0.05-10 mg range is appropriate for measuring even soft films as well without scratching, damaging it. Since it is based on force and displacement measurements the technique can be used with large variety of samples from semiconductors to glass substrates. Supplemented by evaluating software the leveled raw data provides the easily measureable step heights, surface roughness, etc. [63]

In the Figure 15 one can see the equipment itself and a depth profile measured with it and the schematic figure of the process in Figure 16.

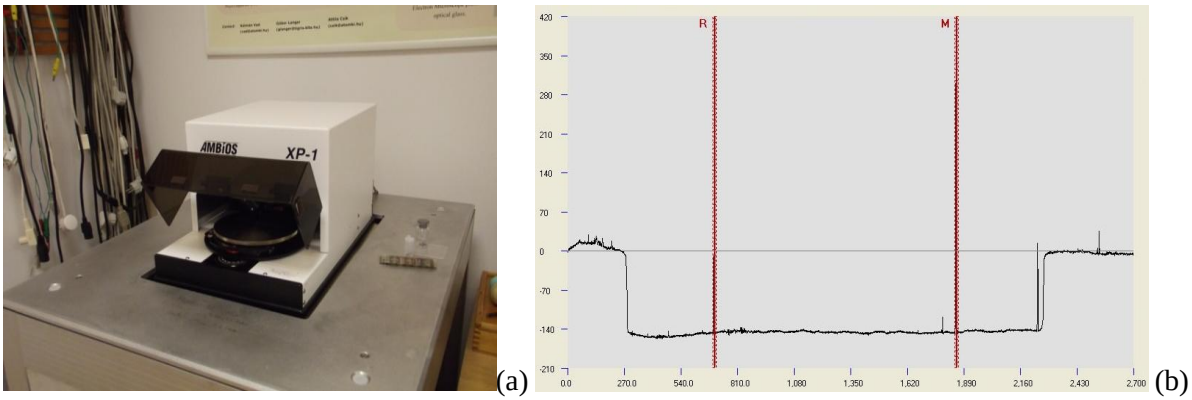

Figure 15 (a) Ambios XP-1 profilometer (b) and a measured linear depth profile

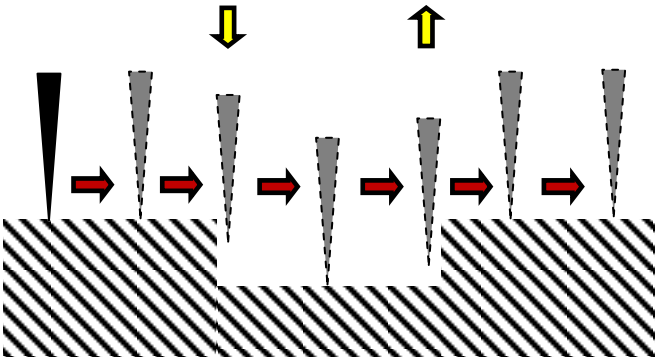

Figure 16 Schematic figure of the profilometer measurement

II.5 X-ray Photoelectron Spectroscope (XPS)

The XPS i.e. X-ray Photoelectron Spectroscopy is a surface analysis technique, with a non-destructive nature, based upon the reaction between the electrons of elements of a given material close enough to the surface and the bombarding (low energy:~1-2 KeV) X-ray photons.

The history of this technique includes the names of famous physicists such as Albert Einstein and at least two Noble prizes as well:

- Nobel Prize for the discovery of the law of the photoelectric effect (Albert Einstein - 1921).
- Shared Nobel Prize for his contribution to the development of high-resolution electron spectroscopy (Kai M. Siegbahn - 1981).

The theoretical base of the technique connects to the photoelectric effect discovered by Heinrich Hertz in 1887 and its description achieved by Einstein.

The law of photoelectric effect applied for photoelectron spectroscopy:

$$E_k = h\nu - E_b \tag{33}$$

where E_k is the kinetic energy of a measured electron, $h\nu$ is the energy of the X-ray while E_b is the binding energy of a given electron.

The process proceeds as it can be seen in the schematic figure of Figure 17.

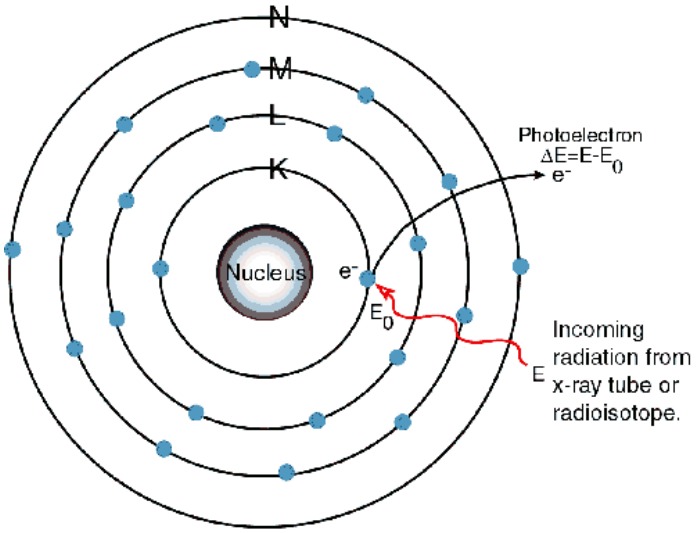

Figure 17 Schematic figure of the photoelectric effect [64]

The XPS is known by another acronym as well namely ESCA i.e. Electron Spectroscopy for Chemical Analysis introduced by Kai Siegbahn et al.

The available information by XPS e.g.:

- Identification of elements
- Relative concentrations
- Chemical state
- Oxidation states of transition metals
- Electron structure

It was found that above its characteristic elemental sensitivity in the upmost layers of a sample the XPS can reveal changes in the electron orbitals affected by the chemical bonds causing a shift in the kinetic energies. Since the depth from which the gathered information is originated is limited by the AL (attenuation length) UHV conditions are required for XPS measurements. It is very important because even at such pressure as 10^{-6} mbar in a few seconds any surface can be covered by a thin strongly bonded gas layer which can strongly alter the surface conditions and so the achievable results, furthermore the number of electrons detected by the detector can be decreased through scattering or attenuation during their path to the detector.

A schematic figure about an experimental setup of photoelectron spectroscopy can be seen in Figure 18 below consisting of 3 main parts:

- the X-ray source
- the UHV vacuum system and
- the detection & analyzer system

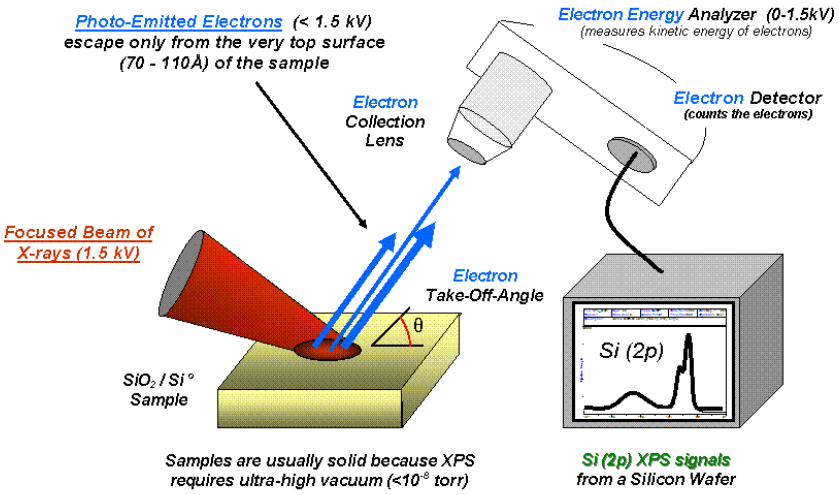

Figure 18 Schematic figure of an XPS system. [65]

The XPS system in the laboratory is consist of a Specs Phoibos 100 (100 mm mean radii)– hemispherical electrostatic energy analyzer (equipped with 5-channel detector) – allows recording energy spectra for negative particles (electrons) and positive particles (ions) in the kinetic range between 0-3500 eV and a HSA 3500 power supply. The system is equipped is supported by two X-ray sources: Al & Mg, and controlled by an XRC 1000 X-ray source control unit. Phoibos analyzers provide the detection of electron and ion energies between 0-3500 eV with minimum step width of 7 meV [66].

There is an interesting detail about the above mentioned two tools, namely the SNMS and the XPS located in Debrecen. They are interconnected through the introduction chamber. It means that we can transfer the samples from one experimental chamber to the other one under high vacuum. This makes possible to extract chemical information via XPS in the craters bored by the SNMS measurements without contaminating the samples. This setup is unique in the world of its kind and holds a great potential.

II.6 Scanning Tunneling Microscope (STM)

Invented by Binning and Rohrer the STM (Scanning Tunneling Microscope) gained the shared Noble prize in physics in 1986 for the two physicists of IBM.

A schematic figure about the system can be seen in Figure 19.

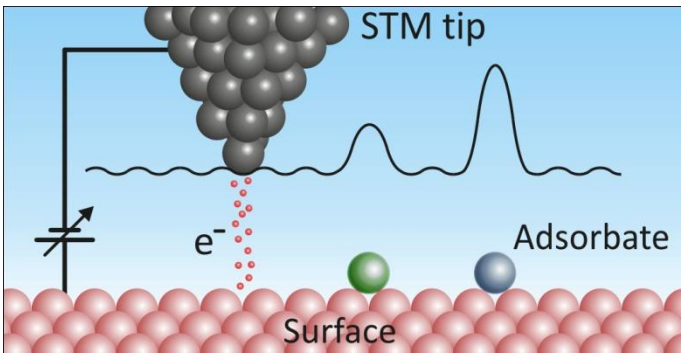

Figure 19 Schematic figure of the STM in work. [67,68]

Theoretically the tip of the STM equipment ends in a single atom, usually made of tungsten (W), controlled by a piezoelectric system in each of the 3 directions (x, y, z) perpendicular to each other. Applying sawtooth voltage on the piezoelectric systems of direction x and y one can scan a given surface. The distance between the tip and the surface of the sample is only a few angstroms during the operation. The electron wave functions between the tip and the surface at such a distance overlap thus the electrons can get through the gap between them (Tunneling effect). The voltage applied between the tip and the surface initiate a tunneling current. The vertical control of the tip afterward is managed through a feedback loop which is dedicated to maintain the above mentioned tunneling current permanent (so called constant current mode). By recording the positions of x, y and z and plotting them we can obtain a 3D atomic resolution image (in case of good conditions) about the scanned part of the sample. The system therefore extremely sensitive for vibrations and even with severe and deliberate work behavior it is quite hard succeeding.

These measurements were performed in Marseille.

II.7 Low-Energy Electron Diffraction (LEED)

The LEED (Low Energy Electron Diffraction) is a technique used to identify surface structures of crystalline materials, based upon particle-wave duality and the scattering of the electrons on the atoms (considered as point sources of scattering). Since the wavelength of these electron (~100 eV) falls in the range of the atomic distances the effect of diffraction rises.

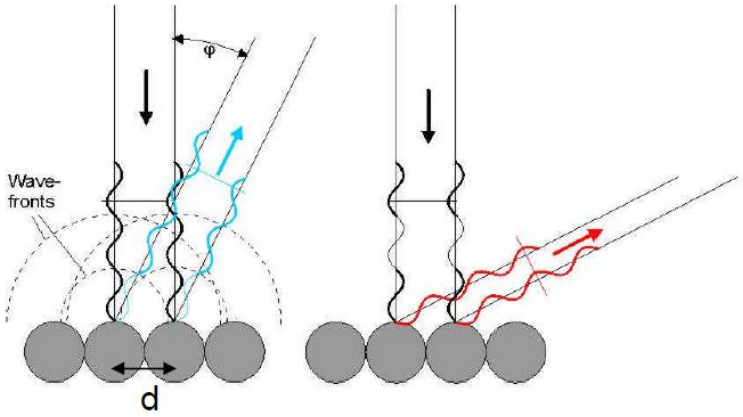

Figure 20 Schematic of the relation of Bragg equation and LEED representing the extinction and the enhancement of the diffracted beam, respectively. [69] (for denotations see eq. 34)

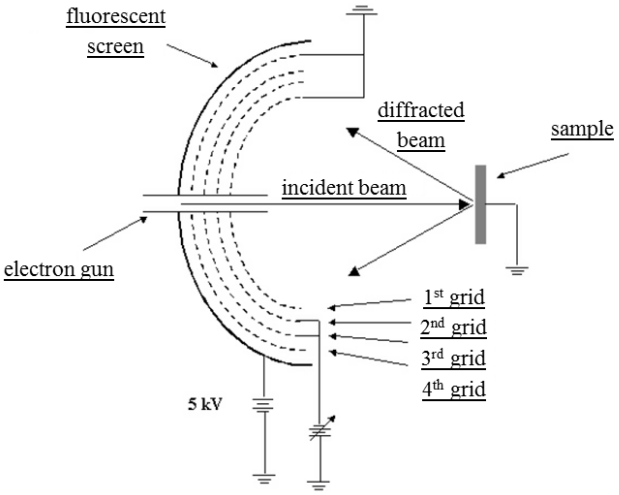

Figure 21 Schematic drawing of a LEED system.

The constructive interference obeying the law similar to Bragg's law used in XRD:

$$n\lambda = d \sin \varphi \tag{34}$$

here d is the periodicity of the surface structure at a given direction.

The wavelength determined by the De Broglie equation.

$$\lambda = \frac{h}{\sqrt{2mE}} \tag{35}$$

Here, *E* is the energy of the primary electron beam (eV), *h* is the Planck constant and *m* stands for the mass. According to the low energy and interaction volume of the incident probe only the upmost few layers participate in the formation of the diffraction image.

The pattern observed on the screen could be originated from the arranged surface of the substrate and from the organized atoms deposited on the substrate.

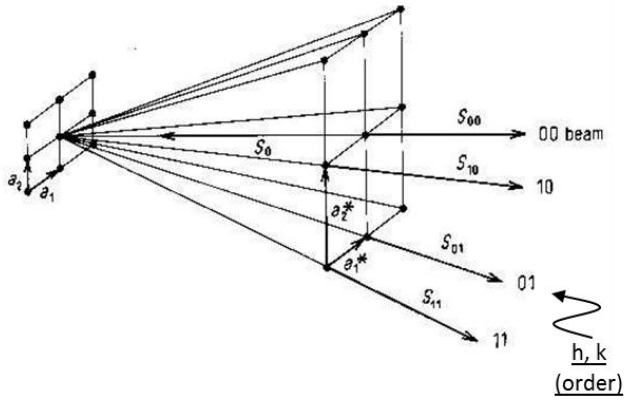

Figure 22 Formation of diffraction pattern in LEED. [70]

In order to identify and separate the different superstructures/overlayers we used the terminology of Woods. Compared to the matrix terminology (where the relation between the structure of the bulk material and the structure of the overlayer is expressed by 2x2 matrices) this one is preferred:

$$i\left(\frac{b_1}{a_1} \times \frac{b_2}{a_2}\right) R(\alpha) - A \tag{36}$$

where *i* equals to *p* (primitive) or *c* (centered) depending on the unit cell defined for the adlayer, b_1 and b_2 stands for the vectors of superstructure, a_1 and a_2 stands for the vectors of the bulk material α refers to the angle between the a_1 and b_1 or a_2 and b_2 and A marks the adsorbant.

Let's note that we can use Woods terminology only when b_1 and b_2 are rotated with the same angle α respect to a_1 and a_2.

This experimental tool in Marseille we used in our experiments consist of an electron gun that emits low energy (~ 500 eV) electrons normal to the sample surface, while the electrons scattered on the sample surface are accelerated toward the hemispherical fluorescent screen (with a potential of 7 kV - in our experiments) and filtered by a set of grids dedicated to let through the elastically scattered electrons only.

II.8 Auger Electron Spectrometer (AES)

The first report/discovery of the phenomenon belongs to the Austrian-Swedish scientist Lise Meitner in 1923; though the technique got its name after the French physicist Pierre Auger who discovered it independently in 1925.

AES i.e. Auger Electron Spectroscopy is a high sensitivity surface analyzer technique. The technique is capable of distinguishing the chemical nature of the constituents of the upmost few atomic layers of a sample, and providing information about their concentrations or about the deposited layer's thickness/amount.

The extreme surface sensitivity comes from the fact that only those Auger electrons can be measured which ones can escape from the material so thus localizing the origin of the information within the upmost atomic layers.

When an atom on the surface of a given sample gets under high energy electron bombardment then an electron from its inner shell (A) could be knocked out. The excited atom can get back to normal ground state through basically two ways/paths. The first step is identical. An electron from a higher Energy level (B) is going to fill in the place of the knocked out electron. The energy difference between these levels can be released in two ways afterwards. In the first case the atom can release this energy in the form of an X-ray photon, which energy will corresponds to the difference between the energy levels (A-B), while in the other case this energy can be transferred and released in the form of an electron ejected from an upper energy level (C), what is called Auger electron. Thus we can distinguish KLL, LMM, MNN transitions. The process is schematically given below.

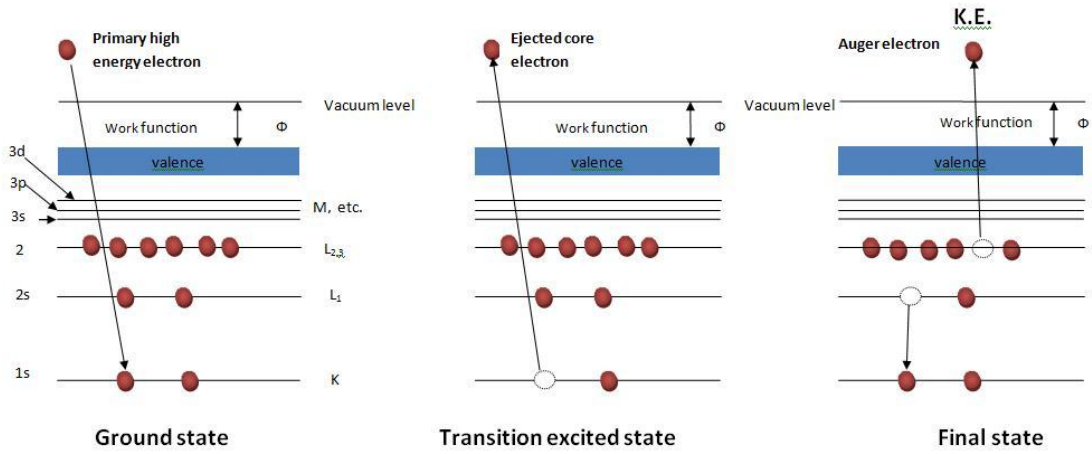

Figure 23 Effect of the ejection of an Auger electron. [71]

The kinetic energy of the escaped and detected Auger electron is given in equation 37:

$$E_{kinetic} = E_A - E_B - E_C - \phi \tag{37}$$

where E_A, E_B and E_C corresponds to the energies of the different energy levels of the electrons participating in the process while Φ corresponds to the work function.

The de-excitation by X-ray photons is preferred by the heavier atoms, while by Auger electron is preferred by the lighter ones. Since this phenomenon needs the participation of several energy states and electrons it is obvious that atoms such as H or He cannot perform such phenomenon.

A schematic figure of the CMA system can be seen in Figure 24.

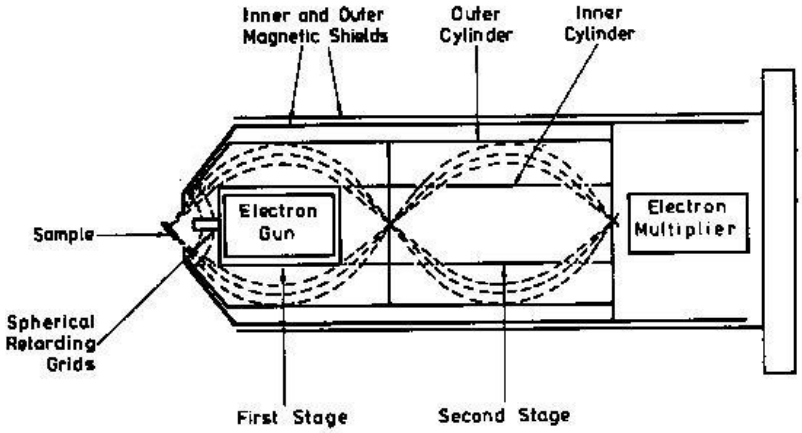

Figure 24 Scheme of the Cylindrical Mirror Analyzer (CMA) [72]

The Cylindrical Mirror Analyzer (CMA) consists of an electron gun surrounded by two concentric cylinders which ones focus ejected the electrons to the window of the electron multiplier.

AES is often used in derivative mode by applying a small sinusoidal AC voltage highlighting the peaks of Auger electrons.

From the measured Auger spectra knowing the peak-to-peak height of the given species we can determine their concentration by equation 38:

$$C_A = \frac{{}^{I_A}/_{S_A}}{\left({}^{I_A}/_{S_A} + {}^{I_B}/_{S_B}\right)} \tag{38}$$

for a sample consist of two components only, where I is the peak-to peak height of the given element and S is its sensitivity factor. The sensitivity factors can be found in the Auger handbooks.

Recording and latter plotting the intensities of the substrate and the deposited element (with a deposition constant deposition rate in time) growth modes can be differentiated such as Frank-van-der Merwe, Stranski-Krastanov or Volmer-Weber.

Let's restrict ourselves here only for the one in interest:

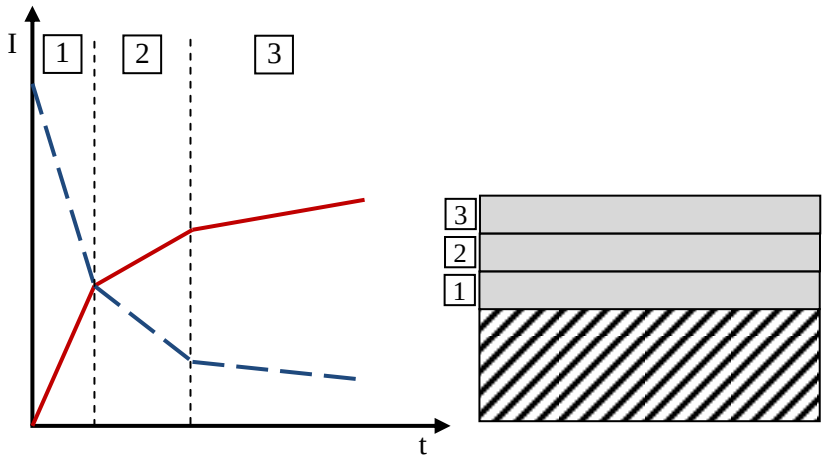

Figure 25 Growth mode of Frank-van-der Merwe, where the break points on the intensity versus time plot refers to the beginning of the growth of the next layer in a layer by layer mode. The (red) straight line represents the intensity of the growing material while the (blue) dashed line represents the intensity of the substrate.

When the growth takes place layer by layer, then the AES curves contains break points marking the beginning of the growth of the new/next layer layer. By having such plots the growth of 1 monolayer of the desired adsorbate can be determined knowing the ratio of the intensities of the substrate and the adsorbate at the breaking point.

Analytical conditions used during the acquisition of the spectra:

During our AES measurements in Marseille we used the following setup at all times: the primary incident electron energy was set at E_p = 2000 eV, the amplitude modulation was 3 V, the emission current (I_e) ranged between 14 and 16μA, the sensitivity was set at 20 mV and the time constant was 0.1 sec.

II.9 Atom probe tomography (APT)

APT started from its invention in the late 1960s by Müller et al. [73] and by the merge of Field Ion Microscopy (FIM) and Time-of-Flight (ToF) detectors, came to live a unique analytical tool for materials science in the last few decades that is called Atom Probe Tomography (APT) [74].

The samples used in this analytical tool have an apex radius of less than 100nm. In general the sample—whatever is its structure—must be shaped into the form of a tip as it is essential for the measurements. We have two main options considering this point. Firstly, we can build the sample upon the top of a pre-etched (e.g. W) tip, thus obtaining highly curved structures. Secondly, we can cut down the top of the pre-etched tip thus obtaining a flat surface with a diameter approximately in the range of micrometers. Considering this second one, it can also proceed in two ways. On the one hand we can use the above mentioned flat end of the tips as a substrate and then deposit the required thin layers onto it to obtain flat thin layered structures. On the other hand we can cut out specimens from the bulk of any kind of material by FIB and attach it to these pillars (could also be purchased) with the so-called "lift-out" technique. In the last step the specimens can be sharpened into a tip shape by a FIB annular milling.

Whatever is the origin of the samples the tip like shape is essential for the proceeding of an accurate measurement.

The basic principle of the method is based on controlled single atom evaporation from the specimen. In order to achieve this a high voltage is applied to the specimen. If this voltage is sufficiently high atoms of the specimen are ionized and desorbed. In a modern APT the so-called base voltage is set to be less than this evaporation threshold. The field evaporation is triggered by additional short electric pulse. On the other hand this technique requires samples with quite good conducting properties in order to gain the achievable best results.

Since this technique could serve with interesting information about not just conductor materials but others as well in some cases the system is supported by a laser (with high impulse rate) that is directed to the tip. In this way the individual pulses of the laser and not the pulses of the high voltage that makes it possible to use this equipment in case of semiconductor or insulating materials as well. Accordingly, the ejection of the parts detected in time is triggered and separated by the laser pulses.

Measurements result in 3D "maps" that show the position and the chemical property of the detected parts in the investigated sample with subnanometer accuracy. These 3D "maps" can be analyzed in a various way later on. We can make straight line concentration profiles or

curved ones (e.g. along the perimeters of grains), we can choose any volume of interest in our sample for a more detailed analysis, or we can use the whole 3D structure in order to pinpoint for example the signs of grain-boundary diffusion or segregation.

The instrument we used is located and has been designed at the Institute of Materials Physics of the Univeristy of Münster (Germany) has a delay line detector system with 120 mm diameter and an aperture angle of 30°. [75]

Chapter III

Results and Discussion

III. Results and Discussion

This chapter will serve with the detailed description of our studies performed on Si based binary systems. The chapter is organized in four sections. It will present the details of the investigations and the results obtained from the simulations concerning the diffusional stress effects basically in Si-Ge system; how we monitored the very beginning of silicide phase formation in the Ni-Si system by a combination of GIXRF and EXFAS in waveguide structure; the result obtained from the combination of various techniques used for investigating the initial phase growth in the Cu-Si system; and the dissolution kinetics measurements where we followed the dissolution of one monolayer silicon (silicene) into the silver substrate. Furthermore, at the beginning of each section a short description of the studied systems will also be given.

III.1 Stress effects on the kinetics of nanoscale diffusion processes

The Ge – Si system is an ideal model of complete mutually soluble systems. The significant difference between the melting points of these two materials presumes strong diffusion asymmetry.

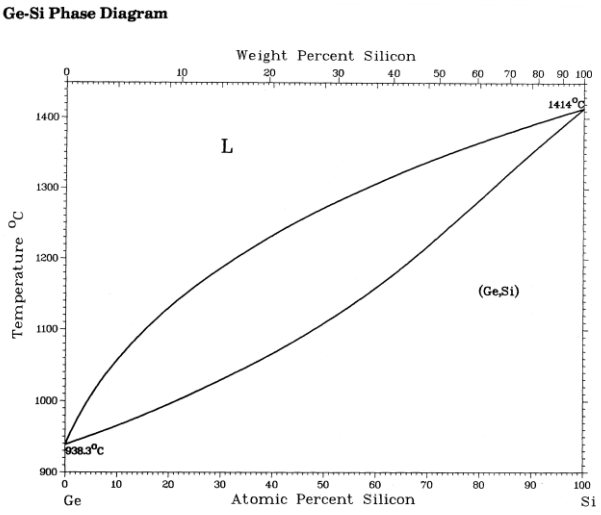

Figure 26 Equilibrium phase diagram of the Si-Ge system [76]

The Si-Ge system is widely investigated and analyzed in many-many aspects as it is usually when there are technologically interesting materials in hand, however the questions about the possible effects of stress with different origin are still the matter of debate (see in [77] and references therein). In order to find another piece of this puzzle we analyzed this question

theoretically – for the sake of simplicity, for planar model geometry – to find the role of stress in diffusion and to identify the cause for effects forcing the system to shift from the Darken to the Nernst–Planck regime as it is reported in [20].

III.1.1 Input parameters and calculations

We didn't want to restrict our simulations to some specific case, however, thus we have chosen input parameters from a quite wide range; the figures in bold correspond to the Si/Ge system:

Young's modulus was supposed to be composition-dependent $E = c_A E_A + c_B E_B$, where $E_A = 18.5, \mathbf{185}$ and 1850 GPa, $E_B = 10.3, \mathbf{103}, 1030, 16.3, \mathbf{163}$[1] and 1630 GPa; Poisson's ratio: $\nu_A = \nu_B = 0.27$; viscosity: $\eta_A = \eta_B = 2 \times 10^{12}, 2 \times 10^{14}$ and 2×10^{16} Pas; molar volumes: $\Omega_\mathrm{A} = 1.20 \times 10^{-5}\mathrm{m^3mol^{-1}}$, $\Omega_\mathrm{B} = 1.36 \times 10^{-5}\mathrm{m^3mol^{-1}}$; $T = 700\,\mathrm{K}$. We supposed exponentially composition-dependent diffusion coefficients: $D_i^* = D_i^0 exp(-mc_A)$ and that $D_A^0/D_B^0 = 1, \mathbf{2.4}$ and 10; moreover, $m' = m \log_{10} e = 0, \mathbf{4}$ and 7 (where e is the base of natural logarithm and m' gives, in orders of magnitude, the ratios of the diffusion coefficients in the pure A and B matrixes; for instance, $m' = 5$ means that the A atoms jumps 100,000 times faster in the A matrix than in the B) [78].

Note that, using these parameter values, t_r falls in the range of $(5-9) \times 10^6$s (~50 – 100 days). We transformed every equation into a form containing only dimensionless variables and parameters: $x' = x/l$, $t = tD/l^2$; $P' = P/E$; $D_i' = D_i/D$; $\eta' = \eta D/El^2$; $\Omega_i' = \Omega$; $\rho_i' = \rho_i \Omega$. Here l is an arbitrary length comparable to the lengthscale of the investigated problem, E is the average Young modulus, Ω is the average atomic volume and D was chosen to be equal to D_A^0.

With the above parameters the equations of (12), (13), (15) and (16) have been solved numerically - input parameters corresponding to the Si/Ge system [$i = A, B$ in the equations: (12) – (16)] - are highlighted. However during the performed simulations a large variety of the parameters were applied in order to check various possibilities and not just one specific case [11,79,80,81].

III.1.2 Results

Figure 27 illustrates two pressure and composition profiles calculated for stress-free initial conditions - (where stress could originate from the diffusion itself only).

[1] Two values (both in bold) had been found in the literature for the Young's modulus of germanium.

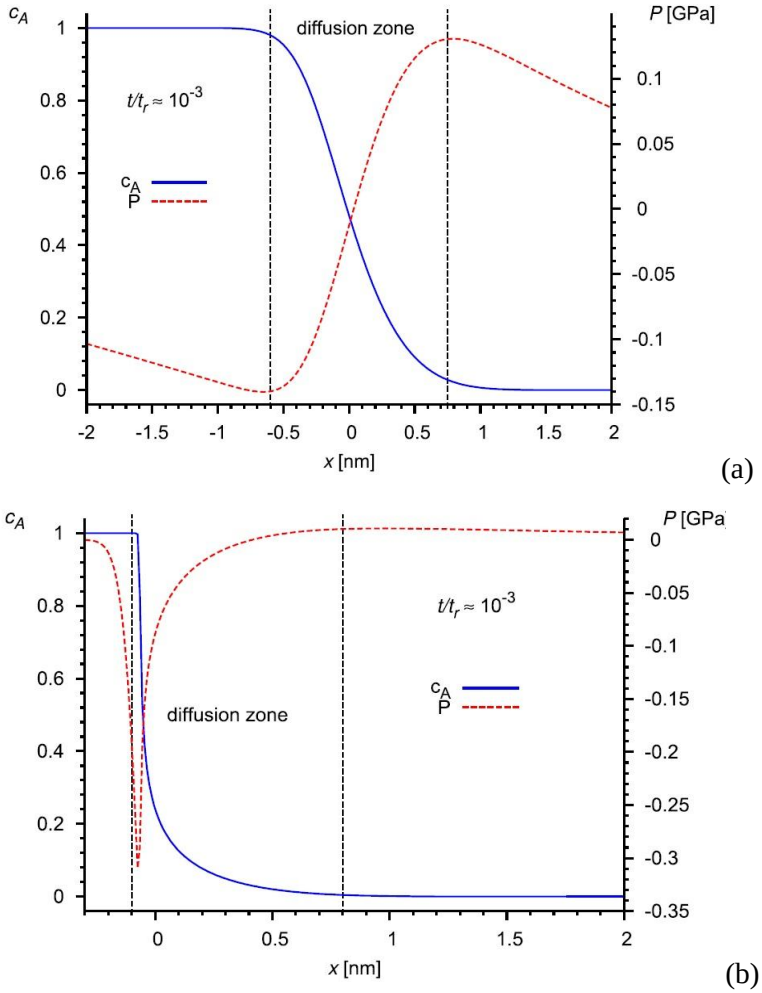

Figure 27 Illustration of two pressure and composition profiles calculated for stress-free initial conditions - (where stress could originate from the diffusion itself only); (a) without and (b) with considering diffusion asymmetry. [82]

Figure 27a shows the stress development in the diffusion couple which changes symmetrically during the diffusion process since we supposed composition-independent diffusion coefficient. Meanwhile in the other case in Figure 27b because of the composition-dependent diffusion coefficient the curves are strongly asymmetric. In such case as can be seen in Figure 27b where the diffusion is orders of magnitude faster in one matrix of the diffusion couple than in the other a sharp stress peak appears close to one of the sides of the diffusion zone and moves with the moving interface, while an almost homogeneous stress field appears on the other side. This is so, because if the diffusion is significantly faster e.g. in matrix B then in matrix A, the A atoms can easily dissolve into the matrix B however the component B can hardly penetrate into the matrix A.

For investigating the diffusion kinetics, the logarithm of the position of planes with constant composition $(c_A = 0.1, 0.2, \dots, 0.9)$ was plotted as a function of the logarithm of time: $x_p \propto t^{k_c}$, i.e. $\log_{10} x_p \propto k_c \log_{10} t$, where k_c is the kinetic exponent.

If the kinetics is parabolic, the data points fit a straight line with a slope of 0.5. If it differs– in case of anomalous diffusion kinetics, either the slope deviates from 0.5 or the data points do not fit a straight line. In Figure 28 one can see two examples, obtained for cases where we took the stress effects into account and where we neglected them. The data points fit a straight line with a slope of ≈ 0.5 for both cases.

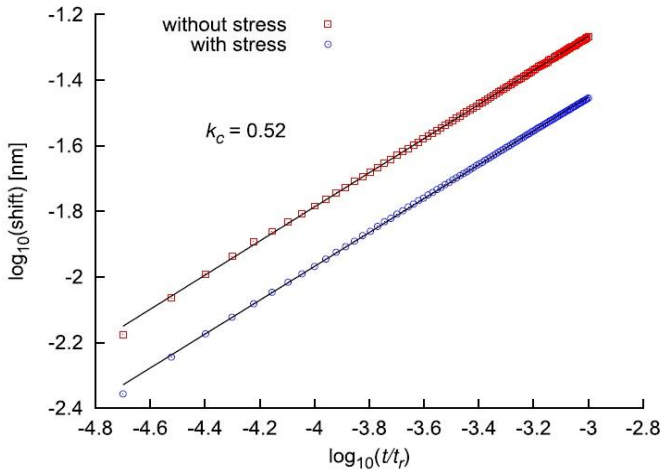

Figure 28 Position of a plane with constant composition $(c_A = 0.6)$ as a function of time $\left(x_p \propto t^{k_c},\ i.e. \log_{10} x_p \propto \log_{10} t\right)$. $D_A^0/D_B^0 = 10$, and the other input parameters are the same as in Figure 27a. As can be seen, the plane shift is around 0.1 nm but k_c is already close to 0.5. Moreover, the intercept is lower for the case when stress is considered; therefore the intermixing rate is slower [82].

Under such conditions that we used during the simulations (see above) the resultant kinetic exponent ranged between 0.5 and 0.55. Although k_c looks unaffected by stress effects it slowed down the intermixing process (the intercept is lower). Considering the time evolution of diffusional stresses, it can be classified into four different stages as was shown in equation (21). According to our observation, stage (i) is extremely short. Intermixing on the scale of a few tenths of a nanometer is enough to reach it, in agreement with the experimental observation of Schmitz et al. [20]. That is the stress gradient at the interface, where the intermixing happens, becomes quasi-stationary extremely quickly for composition-independent diffusivities ($m' = 0$, symmetric diffusion) as can be seen in Figure 27a. In the case of composition-dependent diffusivities ($m' \neq 0$, asymmetric diffusion), the stress profile also becomes quasi-stationary. In this case, however, two significant stress gradients develop at one of the borders of the diffusion zone (at the left boundary of the diffusion zone in Figure 27b). Thus, we would expect different results on the atomic fluxes in stage (ii) considering the spectacular difference in the stress profiles. In stage (ii), for symmetric diffusion case, since

the aroused stress gradient tends to diminish the volume flow, the slowing down of the intermixing is expected. The larger the difference in the present volume flow (measured by $\Omega_A D_A - \Omega_B D_B$) the stronger the effect. Note that stress gradients evolve outside of the diffusion zone as well, however their influences on the intermixing process are insignificant.

In case of asymmetric diffusion, the situation is a little bit more complicated. Since there are two stress gradients with opposite signs on the left side of the diffusion zone (see Figure **27**b), then depending on the sign of the stress gradients one of them decreases while the other increases the volume flow. According to the computer simulations the stress effects slow down the intermixing process even in this case, i.e. the slowing down effect rules the process. As we saw it above the stress effects practically have no influence on the kinetics (the exponent k_c remains fickian).

A diffusion kinetics that deviates from the classical Fickian can arise only if the second term in Eq. (16) becomes dominant or at least comparable to the first one. For further analysis, we reformulate Eq. (16) by rearranging $\Theta_i D_i^* \nabla c_i$ outside the brackets:

$$j_i = -\rho \Theta_i D_i^* \nabla c_i \left[1 + \frac{c_i \Omega_i}{RT\Theta_i} \frac{dP}{dc_i}\right] \tag{39}$$

where $dP/dc_i = \nabla \mathrm{P}/\nabla c_i$. Thus $\frac{c_i \Omega_i}{RT\Theta_i} \frac{dP}{dc_i}$ has to be compared to unity to estimate the weight of the influence of the pressure gradient on the atomic flux. Since the composition and the pressure fall in very similar length scales in the diffusion zone, dP/dc_i is practically constant. Its value can be estimated as c_i changes between 0 and 1 in the diffusion zone, and the change in pressure can be determined from the simulations. Therefore $dc_i \approx \pm 1$. Moreover, $dP \approx 0.3$ GPa in Figure 27. Thus $dP/dc_i \approx \pm 0.3$ GPa . Note that, depending on the input parameters, the absolute value of dP/dc_i falls in the range of 0.2 - 1 GPa. Substituting $c_i = 0.5$ (as an average value in the diffusion zone), $\Omega_\mathrm{i} = 10^{-5} \mathrm{m}^3\mathrm{mol}^{-1}$, $T = 700\ K$ and $\Theta_\mathrm{i} = 1$, the absolute value of $\frac{c_i \Omega_i}{RT\Theta_i} \frac{dP}{dc_i}$ is equal to approximately 0.17 – 0.86, and thus has an important influence on the atomic flux. Thus the intermixing slows down. However, as the composition and the pressure fall in very similar length scales and their maxima hardly change, the dP/dc_i ratio is practically constant for a very long time, even for $t > t_r$.

A simple multiplying constant in the flux cannot change the kinetic exponent, but may result in the slowing down of the process. Defining $\Theta_i D_i^* \left[1 + \frac{c_i \Omega_i}{RT\Theta_i} \frac{dP}{dc_i}\right]$ as an effective diffusion coefficient D_i^{eff}, the expression (39) for the flux can be written in the form of $j_i = -\rho D_i^{eff} \nabla c_i$. According to these in our simulations one of the two atomic fluxes is enhanced by a factor of 1.17 - 1.86, whereas the other is diminished by a factor of 0.83 - 0.14. The respective changes of the atomic fluxes actually level them. This means that the system is

in a Nernst–Planck regime i.e. the diffusivity is limited by the slower component. This can be seen at the beginning of the curve in Figure 29., where the ratio of the atomic fluxes is plotted as a function of time. The fluxes depend, of course, on the position (see Figure 30). In Figure 29 the ratio is calculated from the maximal absolute value of the fluxes, i.e. $\max|j_A| \,/\, \max|j_B|$. As can be seen, the ratio decreases extremely quickly from 10 to approximately 1. In the Nernst–Planck limit $D_A^{eff} \approx D_B^{eff} = \widetilde{D}_{NP}$, where $\widetilde{D}_{NP}$ is the interdiffusion coefficient in this limit, whereas in the Darken limit (no stress) $D_A \approx \widetilde{D}_D$: $\widetilde{D}_D/\widetilde{D}_{NP} \approx 1.2 - 7.1$ in our calculations.

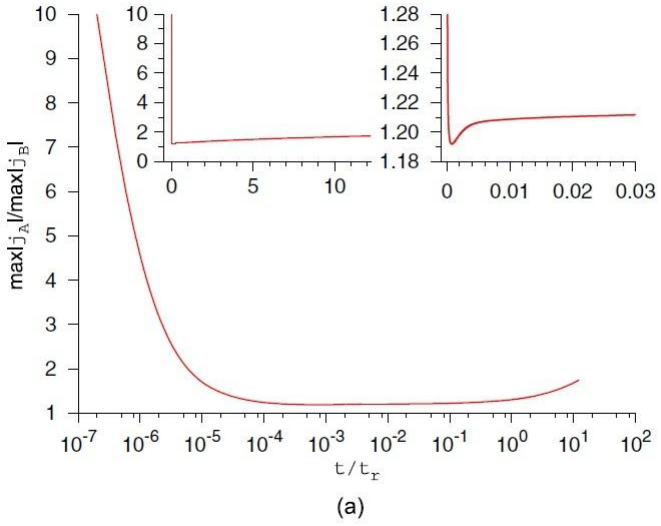

Figure 29 Ratio of the atomic fluxes of the atoms A and B versus the logarithm of time. The left inset shows the same curve but the time scale is linear, whereas the right inset shows the curve around its minimum [82].

Note that this change is of the same order of magnitude as that observed in Ref. [20]. In that study $\widetilde{D}_D/\widetilde{D}_{NP} \approx 2.6$, where $\widetilde{D}_D$ and $\widetilde{D}_{NP}$ were calculated from the growth rate of the Θ' phase in the Cu/Al/Cu as well as Al/Cu/Al triple layers. In stages (iii) and (iv) in Eq. (17), significant stress relaxation is expected. We observed hardly any decrease in the stress levels, even though the investigated time interval was much longer than the stress relaxation time t_r. This is so because in our case $\sum_i \Omega_i \nabla j_i$ (the volume flow) is not negligible compared to $\frac{3}{4\eta}P$ in Eq. (1) even in the steady-state regime, as can be seen, for example, in Figure 31. Consequently, the stress is not only relaxing but also always redeveloping, and the estimation of t_r from Eq. (18) leads to an unrealistic value.

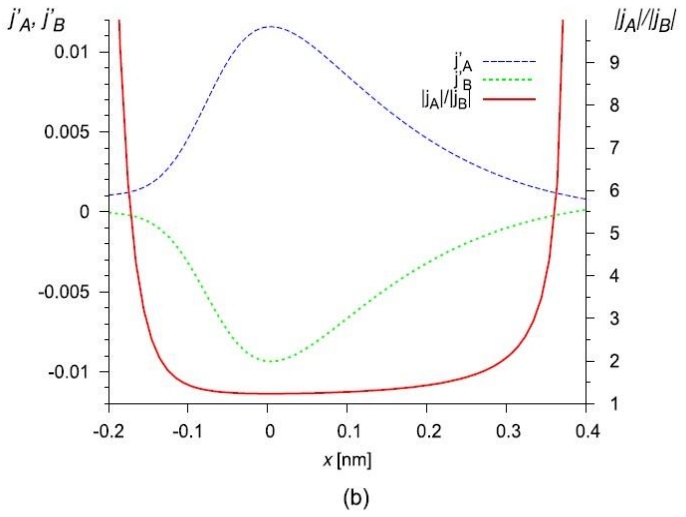

Figure 30 Atomic fluxes (their dimensionless form: $J_i' = J_i \Omega l / D$) and their ratio in the diffusion zone at $t/t_r \approx 1/5$. Input parameters: $m' = 0$, $D_A^0 / D_B^0 = 10$, $E_A = 1850$ GPa, $E_B = 1630$ GPa, $\eta = 2 \times 10^{12}$[82].

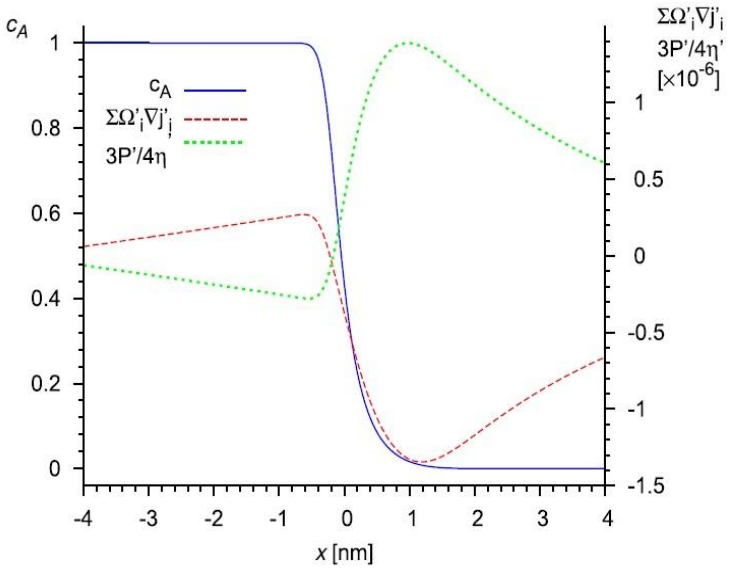

Figure 31 Composition profile as well as the dimensionless form of $\sum_i \Omega_i \nabla j_i$ and $\frac{3}{4\eta} P$ from $t/t_r \approx 2$. This figure is similar at any t/t_r in the steady-state regime [82].

III.1.3 Conclusions:

In conclusion we obtained that stress effects do not have any measurable effects on the kinetic coefficient of the interface shift, i.e. the parabolic growth rate is preserved. However, the intermixing rate decreases.

The stress field enhances the atomic flux of the slower component but diminishes the other. As a consequence, their initial difference is equalized, leading to the establishment of the Nernst–Planck regime. The development of the Nernst–Planck regime is remarkably fast, finishing before any detectable shift of the interface. These results are in agreement with the results in of Schmitz et al.[20].

Since the composition profile is not static but changes quickly and thus the stress redevelops continuously in the time scale of the stress relaxation, then the steady-state stage was not long enough to reach its perfect relaxation.

My own contribution: *I have contributed to the development of the software, performed the computer simulations and participated in the evaluation of the results.*

III.2 Investigation of the early stage of phase formation in Ni-Si system by XSW based techniques

In this section we demonstrate that using a combination EXAFS and GIXRF in waveguide structure and comparing their results can be used to follow the phase growth in metal silicide systems in a non-destructive way. To our best knowledge our Hungarian team used first these methods to monitor compound phase formation, namely the formation of CoSi in Co-Si system [49]. The experiment reported in this thesis is the second example.

As a model system we have chosen another technologically important participant in most of the electronic devices, the Ni-Si system. The properties of nickel silicide thin films have taken on importance for advanced technologies in state-of-the-art microelectronic devices [83,84,85,86,87,88,89,90]. The lower formation temperature, silicon consumption and the slightly lower resistivity overcome the limitations of $TiSi_2$ as well as $CoSi_2$ contacts and its scaling ability provides an extension into the even lower scale technology range. Formation that is controlled by diffusion (vs. nucleation) of Ni [91] leads to much smoother interfaces and surfaces. The phase sequence and identification has been discussed in the past [88,92]. Depending on the Ni film thickness, the Ni_2Si, Ni_3Si_2 and $Ni_{31}Si_{12}$ phases have been observed. (see also Figure 32) The initial phase to form is a strained Ni_2Si layer [88,93]. The strain in this original silicide layer remains until the Ni film is completely consumed.

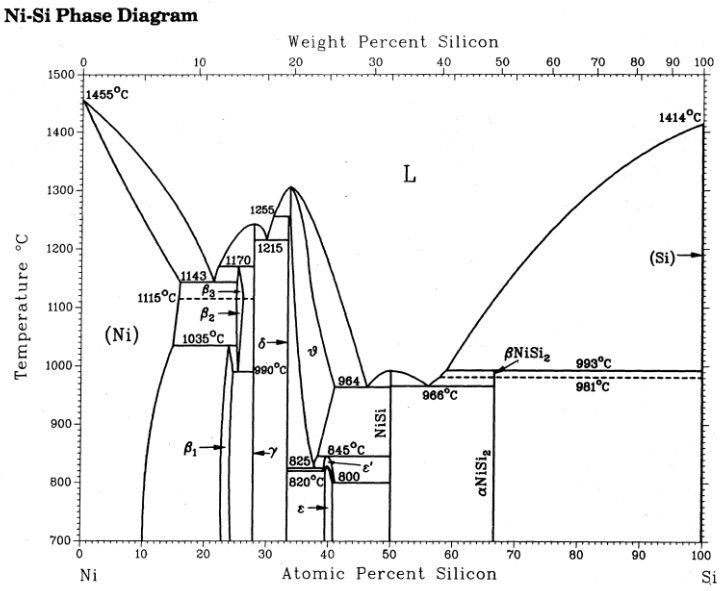

Figure 32 Equilibrium phase diagram of the Ni-Si system. [76]

III.2.1 Experiments

The Ta(5 nm)/a-Si(12 nm)/Ni(10 nm)/a-Si(14 nm)/Ta(30 nm)/SiO_2(substrate) samples were prepared by magnetron sputtering (see II.1.1). Tantalum was chosen as waveguide (mirror) layers since on the one hand it fulfills the requirements to be good mirror materials (high atomic number) and on the other hand Ta/Ni contacts remain intact during heat treatment (no reaction or significant diffusion take place). The samples were annealed for different times at 463K and 503K in a furnace under high vacuum ~10^{-7} mbar conditions. Note that on the basis of previous and literature results, we expected measurable Ni_2Si phase formation (first phase to grow) in this temperature range. Ni_2Si and Ni standards have also been prepared in order to perform linear combination fit using EXAFS data.

The graded-crystal monochromator beamline KMC-2 was used to set-up of the in-depth nanoprobe EXAFS system. The X-ray beam in the energy range of 7 keV–9 keV was monochromatized by the double-crystal monochromator and collimated in both directions using two slit systems. The X-ray beam is condensed to the sample using a toroidal mirror. Since the convergent beam is passing through the monochromator, a special Si-Ge graded crystal was used to provide the energy bandwidth of 1.5 eV. The beam size on the sample position was 100 μm horizontal and 700 μm vertical. The beam divergence was obtained on the order of 20 arc sec by the rocking curve measurements of a Si (111) reference crystal. The total flux in the spot was in the range of 10^9 phot/s/100 mA. Ring current varied between 290 and 150mA. Beamline monochromator, stabilized by MOSTAB feedback system for EXAFS measurements, provides RMS intensity variations in the order of 1.7×10^{-3} in entire energy range. Control software was used to provide simultaneous energy scan of the monochromator

and angular scan of a sample. A schematic figure of the experimental setup can be seen in II.3.1. (see Figure 13)

For every sample, a simultaneous reflectometry and GIXRF measurement were performed to measure the composition profile of the multilayer sample. PIN photodiode detector was used for measurements of reflected (diffracted) beam and an energy dispersive detector was mounted 10 mm above the sample surface oriented normally to the surface to record the fluorescence spectrum of the sample. We used an energy value above the K absorption edge of Ni (8.33 keV). We changed the angle of the incidence between 0-0.6^{o} and achieved the formation of X-ray standing waves with 4 anti-nodal parts.

EXAFS experiments by detecting the fluorescence signal were performed for standing wave patterns with the maximal field amplitude at the interfaces. We tuned the energy between 8300 – 8600 eV

III.2.2 Results

III.2.2.1 Profile reconstruction – GIXRF

As was described in II.3.1, since the GIXRF intensity can be measured and calculated we can compare the measured and the calculated signals. In this way by the measured and simulated intensity curves, the composition profiles can be reconstructed.

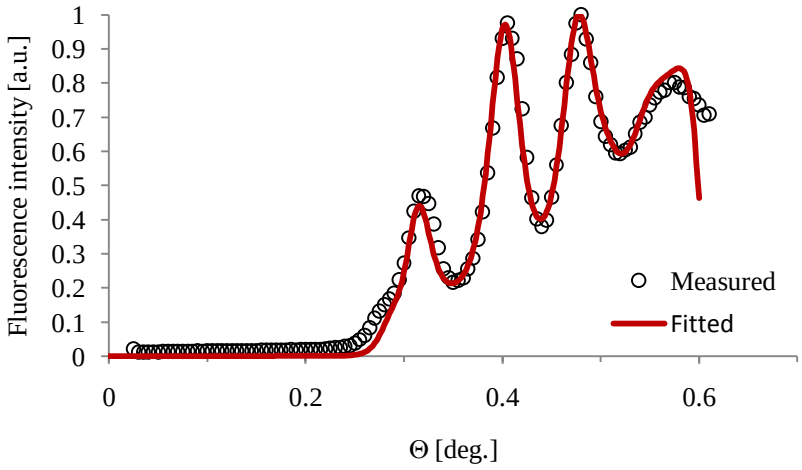

Figure 33 Measured data (annealed at 503 K for 4h30) obtained from GIXRF measurements (blue squares) and the fitted counterpart (red line).

As a demonstration Figure 33 shows a measured and a calculated intensity curves. Note that at higher incident angles the signal can get smeared since in real samples the thickness in

millimeter range can vary few nanometers and that can cause deviations between the real and simulated curves. This effect does not equal to the roughness of the layer at the interfaces, which one can be included in calculation.

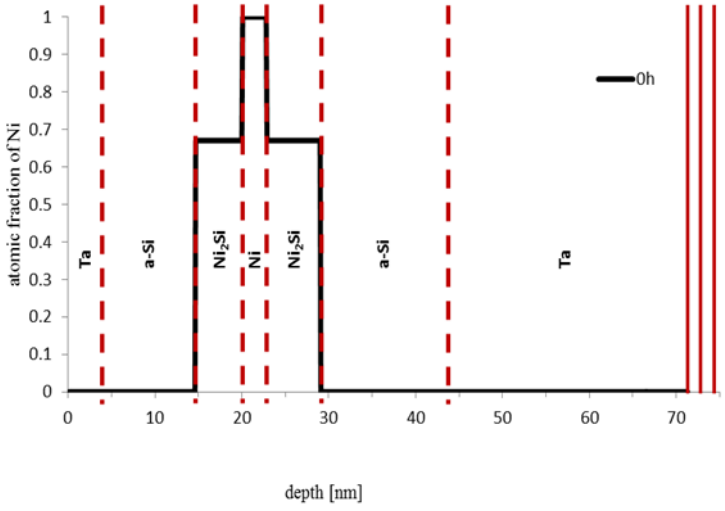

(a)

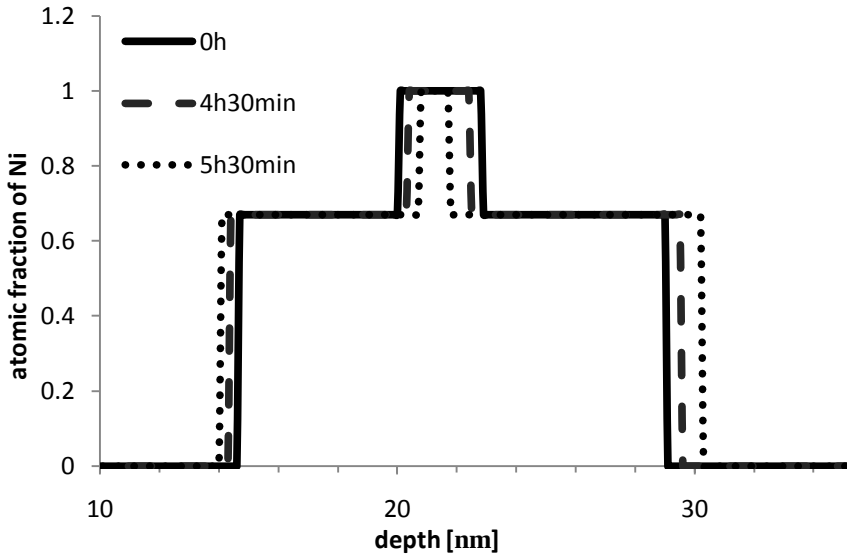

(b)

Figure 34 a) Full composition profile of Ni and the initial positions of the interfaces in case of the as-deposited sample. b) $Ni_2Si/Ni/Ni_2Si$ layer structure right after the deposition (0 hours) and after 4 hours 30 minutes and 5 hours 30 minutes of annealing at 503 K).

Figure 34 shows the reconstructed profiles for the samples annealed for 4 hours 30 minutes, 4 hours 45 minutes and 5 hours 30 minutes at 503 K. As can be seen even at the as-deposited sample a Ni_2Si phase or a mixture of Ni and Si with 2:1 composition ratio (even if

amorphous) has already formed on both side of the pure Ni. Such a phenomenon is not unique for samples prepared by sputtering techniques, where a several nm thick mixed layer's existence is possible [94,95,96].

III.2.2.2 EXAFS

We performed EXAFS measurements in fluorescence detection across the Nickel absorbing edge. With this experiment we wanted to obtain more information about the composition of the specimen as well as the chemical state of the species (number of nearest neighbors, atomic distances, etc.) The EXAFS data have all been carefully calibrated, aligned, and merged. The raw EXAFS data had to be calibrated by the known value of the absorption edge of Ni at first. Then the data of the separate measurements had to be aligned to that edge. Finally, for better statistics, samples were measured several times and the data points were merged.

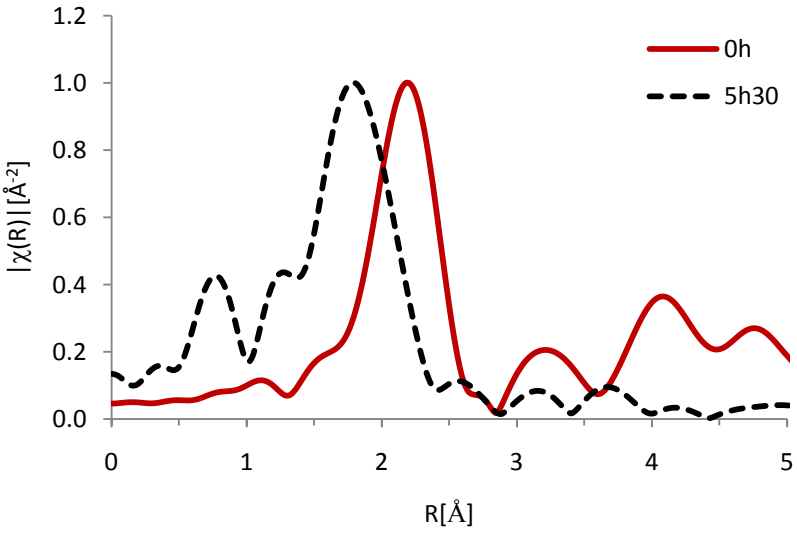

Figure 35 Magnitude of the Fourier transform of $\chi(k)$ for the as-prepared and the annealed (5.5h) specimen plotted on a normalized scale.

In Figure 35 the magnitude of the Fourier transform of the as-prepared and the annealed (5.5h) specimen is plotted on a normalized scale. The relative average atomic distances can easily be read from this kind of plot. As can be seen, the position of the most intense peak is shifted towards smaller value of *R*, which means that the nearest neighbor distance is decreased. This is in agreement with the expectation that Ni_2Si forms at the Ni/Si interfaces during heat treatment. This also shows that in the as-prepared sample (see Figure 34), at the interfaces there are only mixtures, possibly amorphous, of Ni and Si atoms with a ratio corresponding to Ni_2Si.

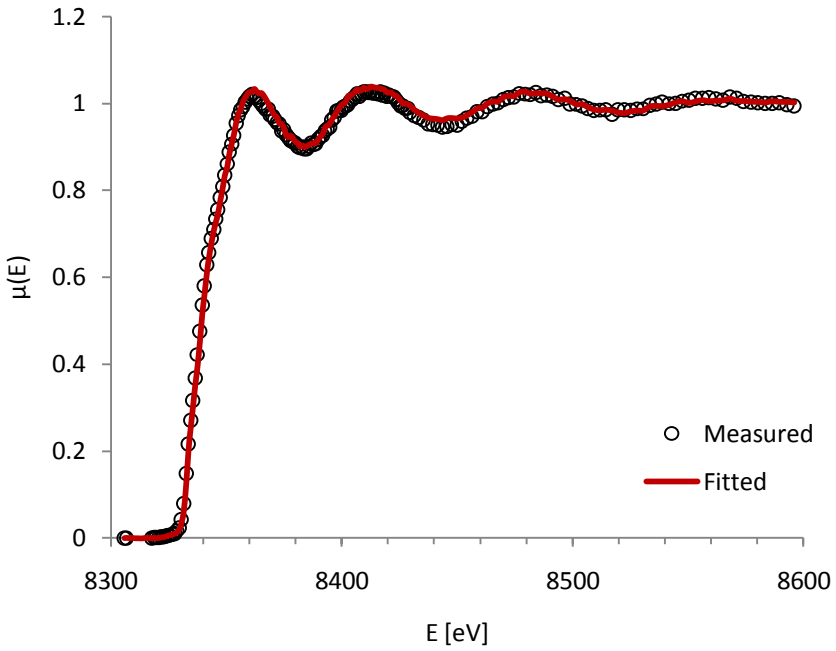

Figure 36 Result of the linear combination fit (see in the text) of the data is plotted (sample annealed at 503K for 4.5h).

In Figure 36 the result of the linear combination fit of the data of a sample annealed at 503K for 4.5h is plotted. The linear combination fit means that we also performed measurements on standards (Ni and Ni_2Si samples, which were prepared on the same manner as the specimens themselves) and used their weighted results to fit the EXAFS data obtained from the real samples In order to further strengthen the idea that the product phase is indeed Ni_2Si, the EXAFS data was fitted up to R = 5Å (k=8.5Å^{-1}) using the ATHENA-ARTEMIS software package [97]. (see Figure 37) This analysis confirmed that Ni_2Si was formed at the interfaces during annealing but only a mixture of Si and Ni atoms with 2:1 composition ratio was at the interfaces in the as-prepared samples. We found that after an annealing of 5.5h at 503K, almost the whole Ni layer transformed to the Ni_2Si intermetallic phase. This is in agreement with the GIXRF results (see Figure 34).

Note that the result of the EXFAS analysis was used to refine and confirm the sample structure to fit the fluorescence curves.

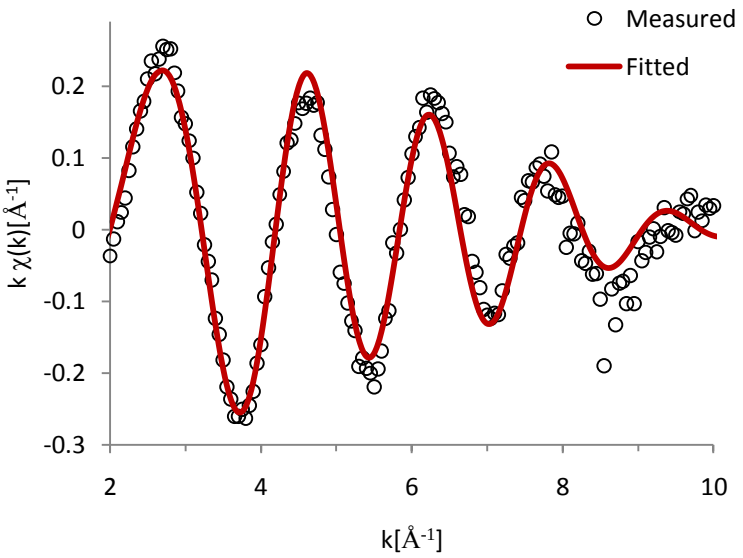

Figure 37 Fitting of the recorded EXAFS spectrum of the annealed sample. Crystallographic data of the Ni_2Si were used from [98] in the Arthemis software in order to fit the obtained data.

III.2.2.3 Determination of the I_{Ni_2Si}/I_{Ni} ratio

To increase the reliability of the results obtained using GIXRF-EXAFS combined method we further developed the evaluation method by correlating the results obtained from the GIXRF and EXAFS *independent* measurements.

Both in the GIXRF and EXAFS measurements the total fluorescence signal is originated from the volume where the pure Ni and the Ni_2Si product layers overlap with the anti-nodal parts of the generated electric field (Figure 38) and proportional to the number of Ni atoms in the overlapping area.

This means that the ratio of the signal coming from the Ni_2Si layers and the Ni layer (I_{Ni_2Si}/I_{Ni}) can be deduced from the GIXRF measurements, since it is equal to the overlapping area of the electric field and the Ni_2Si layers times 2/3 (only 2/3 of the atoms is Ni in Ni_2Si) divided by the overlapping area of the electric field and the Ni layer. Both the electric field pattern and the composition come from the fitting procedure described in II.3.1.

On the other hand, I_{Ni_2Si}/I_{Ni} originating from the EXAFS measurements is equal to the ratio of the weighting factors used in the linear combination fit presented in III.2.2.2 (see Figure 36)

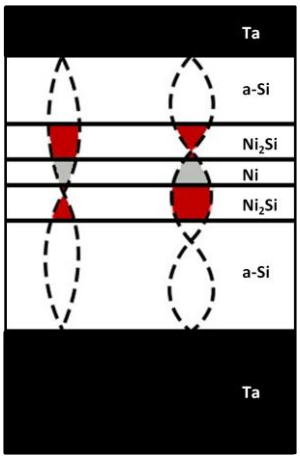

Figure 38 The source of the fluorescence signal for two different transversal modes of the electric filed. The total fluorescence signal is originated from volume where the pure Ni (gray) and the Ni_2Si (red) product layer overlaps with the anti-nodal parts of the generated XSW. The ratios calculated and plotted in **Figure 39** come from the weighted values of these areas.

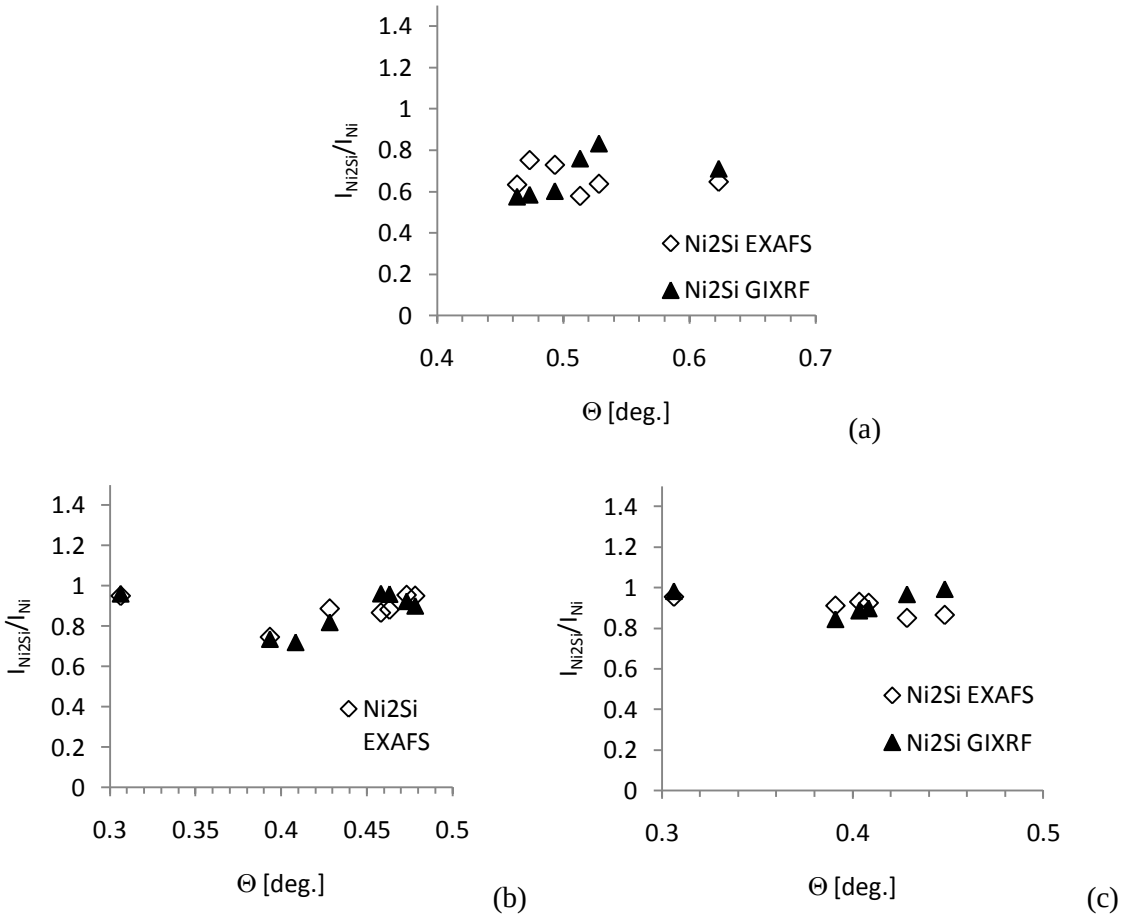

Figure 39 I_{Ni_2Si}/I_{Ni} ratio for (a) as-prepared, annealed at (b) 503K for 4h 30 min and (c) 5h 30 min obtained from the EXAFS and GIXRF analyses.

I_{Ni_2Si}/I_{Ni} was determined for different transversal mode of the electric field and as a function of annealing time. (see Figure 34)

As can be seen, the results we got from the two independent experimental methods are in a good correlation.

III.2.3 Conclusion

The experiment reported in this thesis is the second example for such a study where the silicide formation was followed by XSW based technique. This was, however, not only a repetition of the previous experiment in another system but further developed the evaluation method by correlating the results obtained from the GIXRF and EXAFS *independent* measurements. From both analyses we were able to determine the I_{Ni_2Si}/I_{Ni} ratio in the function of annealing time and compare them, which increase the reliability of this combined method.

In conclusion we demonstrated that using a combination GIXRF and EXAFS analysis in waveguide structure can be used to follow the phase growth on the nanoscale in metal silicide systems in a non-destructive way. The GIXRF and EXAFS measurements equally pointed out the appearance the later development of the Ni_2Si phase. It has already been proved in many different fields that the experimental capacity and variety of synchrotron radiation based techniques is remarkable. With this work we wanted to contribute to the already existing and commonly used methodology by investigating the phase formation.

My own contribution: My part in this investigation included the sample preparation. I have participated in the measurements in HZB and lead the data analysis concerning the GIXRF measurements. Furthermore I did perform the calculations for the determination of the Ni_2Si/Ni ratio.

III.3 Phase growth in amorphous Si-Cu system: combination of SNMS, XPS, XRD, and APT techniques

The Cu-Si system, as it can be seen in Figure 40, forms multiply silicide phases similarly to the Ni-Si system. It shows a negligible Cu solubility in Si and around ~10% maximum solubility of Si in Ni and just like in case of the Si-Ge system, the large difference in the melting points assumes a strong diffusion asymmetry in this case as well.

Previous experiments have shown that the MIC starts with the formation of the Cu_3Si phase. See in ref.: [99,100].

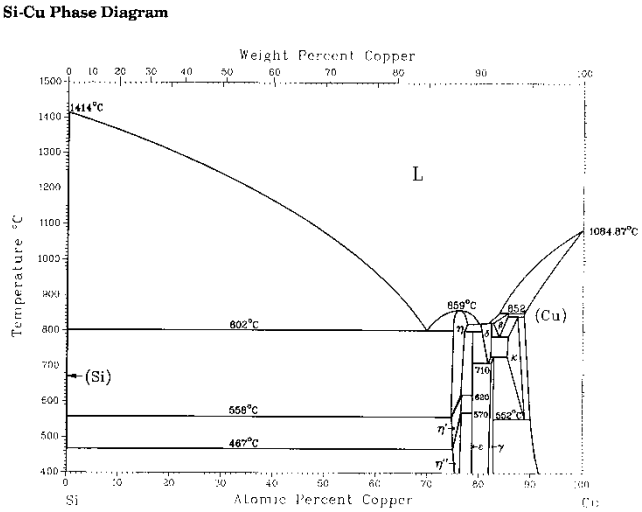

Figure 40 Equilibrium phase diagram of the Cu-Si system. [76]

It is well known that crystalline, high efficiency, silicon films has a crucial importance in solar cell industry. Since the efficiency of amorphous silicon solar cells is restricted by their disordered state then their efficiency tail away from their monocrystalline big brother. Low cost deposited silicon films built by physical vapor deposition usually amorphous but the quite high (re)crystallization temperature of silicon (around 1000 K) requires heat resistant so thus expensive substrates (such as quartz glass). In Ref. [31] one can see in Figure 41 a set of possible substrates and their heat tolerance.

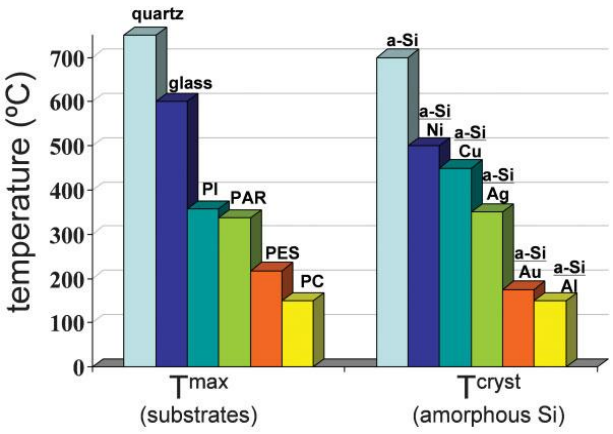

Figure 41 "The left-hand side shows the maximum operating temperatures (Tmax) of some technologically important substrates: quartz glass, conventional glass, polyimide (PI), polyarylate (PAR), polyethersulfone (PES), and polycarbonate (PC). The right-hand side shows the reduction in the crystallization temperature of a-Si (Tcryst) induced by contact with various metals." [31]

It can be clearly seen that the recrystallization of pure a-Si requires the expensive substrate but in the other hand that one can be seen clearly just as well that this problem can be solved.

Another field where the above mentioned Cu_3Si phase can play an interesting role is the field of power sources. The core of the new generation li-ion secondary or rechargeable batteries/cells, the Si nanowires or nanorods used as anodes have higher specific capacity and enlarged surface compared to the traditional graphite anodes. This results in an increased energy density and faster charging-discharging, and some other advantages, see in ref.: [101].

From the structural build-up of these new generation batteries and due to the large volume change caused by the insertion and extraction of Li ions during the charging processes, arise some disadvantages as well. The anode arrangement is brittle. Consequently it loses its initial shape and electric properties quickly, which shortens the lifetime of the battery. Other works pointed out the possibility of increasing the cycling stability with a copper coating or co-depositing Cu and Si can increase significantly the reversible capacity and the flexibility of these power sources – [101].

In each case it was shown by XPS or XRD that the Cu_3Si phase has appeared during the fabrication. This in turn means that studying the formation and the changing of this phase could have technologically great importance. Her et al. observed the appearance of this phase between 370-520 K [100]. Moreover depositing an a-Si/$Cu_{70}Si_{30}$ layer, Ou et al. reported the formation of crystalline Cu_3Si grains in the as prepared layer [102]. The kinetics of the phase growth in the 450-500 K range was found to be parabolic by Chromik et al, [103] while in some Metal/Si systems non-Fickian phase growth kinetics was observed [104,105,106,107,108].

III.3.1 Experiments

III.3.1.1 Phase growth of Cu_3Si

As it has been shown in the previous chapter, the sample preparation has been done by a DC magnetron sputtering system at ambient temperature. The Cu/a-Si sample structure has been deposited on Si(100) substrate. Before the deposition of the 120 nm a-Si and the latter 45 nm Cu layer, the base pressure in the main chamber was $P = \sim 10^{-7} mbar$. Targets of Cu (99,99%) and Si(99,999%) were used as sputtering sources. The sputtering was performed at $P = 5 \times 10^{-3} mbar$ pressure and the sputtering powers were set at 40 Watts. In order to make sure that we can compare the annealed samples to the as deposited ones, the samples were cut into pieces. Since the size of the samples was under the homogenous area of the magnetron sources, we expect for the whole surface of all the samples a good homogeneity in thickness. We used an AMBIOS XP-1 profilometer to determine the sputtering rates and the latter layer thicknesses.

In order to determine the thickness of the layers for the as deposited samples, we took a depth profile with SNMS (Secondary Neutral Mass Spectrometer) till we reached the native oxide layer, marked by the reduction in the Si (28 amu) signal. The second crater was ion etched till the Si (28 amu) and the Cu (63 amu) signals became equal. These depths were measured by the previously mentioned profilometer.

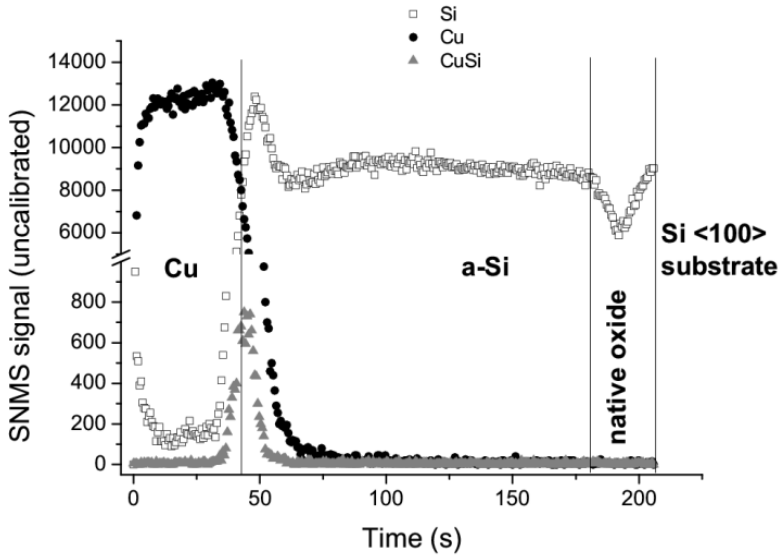

(a)

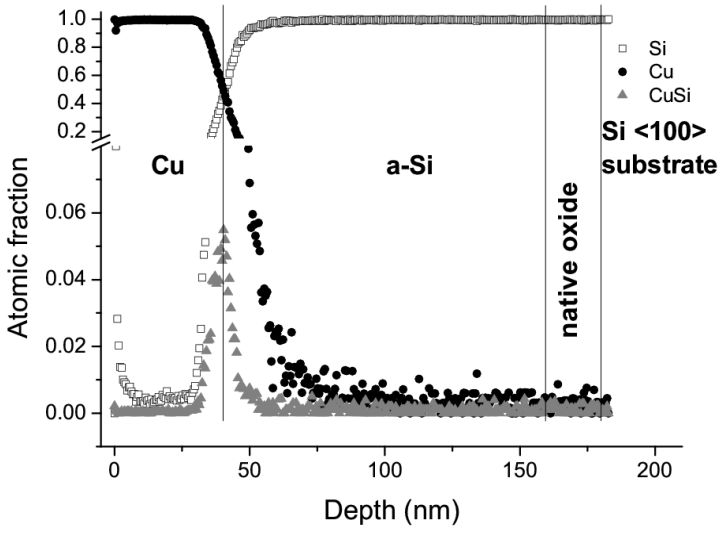

(b)

Figure 42 (a) Raw data (intensity vs. time) and (b) the calculated, concentration depth profiles of the as-deposited sample, respectively [109].

The depth of the second crater gave the thickness of the Cu layer (41.6±1.6 nm, the error represents the standard deviation of 21 individual crater depths). This depth position was set

later as the position of the original Cu/Si interface. The Cu/Si transition zone was found to be adequately narrow, in the range of 10 nm.

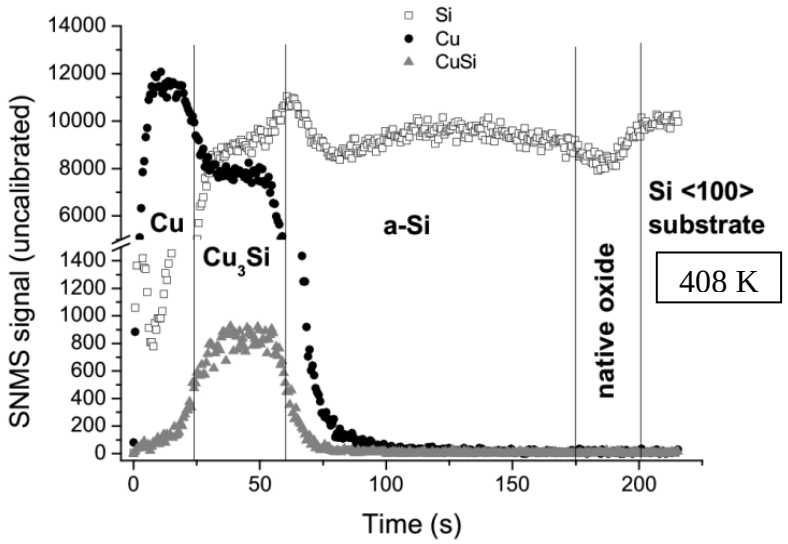

(a)

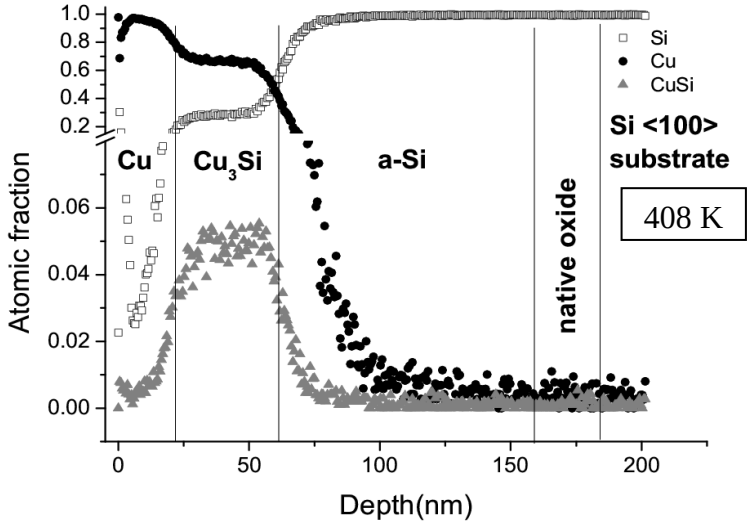

(b)

Figure 43 (a) Raw (intensity vs. time) and (b) the calculated, concentration depth profiles of an annealed sample (12 hours), respectively [109]. The vertical lines indicate the positions where the bombardment was stopped (and thus mark the borderlines between the different phases of the sample [Cu/Cu_3Si/a-Si] as it is shown).

Right before the heat treatment in order to determine the right temperature and the belonging time for the heat treatments, we performed 4-wire resistivity measurement. Al_2O_3 <111> (Sapphire) substrate were chosen since it is insulator material. From the result gained from the curve of the 4-wire resistivity measurement, we chose 408 K as the annealing temperature and

annealed the second part of the samples for 1, 2, 4, 8, 12 and 18 hours and another one that we declared as "t_0" since at the moment when the temperature reached the above mentioned 408 K value, the annealing system was turned down so thus the sample immediately started to cool down.

Note that, the heat treatments and the 4 wire resistance measurements were performed in high vacuum conditions (in the range of $P = 10^{-6}\ mbar$) in a separate vacuum chamber.

Right after these heat treatments, the samples were moved to the SNMS system where the samples with their as deposited pair were analyzed and the thicknesses of the initial and product layers were determined for each sample. In both case we followed not only the signal of Si (28amu) and Cu (63amu) but the (28+63 amu) signal of CuSi molecule were also recorded. Note that the majority of the sputtered species is individual atoms, sputtering of molecules has very low probability especially that of more complex ones. This suggests the detection probability of molecules is negligible. On the other hand molecules may be formed by recombination of atoms above the surface of the sample. Formation of molecules larger than diatomic has, however, infinitely low probability, hence cannot be detected. We were able to detect CuSi signal which is a good indicator that both components were present in the analyzed (see Figure 43).

We stopped the ion bombardment, when the CuSi intensity curve dropped to the half of the plateau value in the reaction layer on both sides. - The depth of each ion etched craters was measured with the profilometer afterward. One can see that this procedure requires numerous samples since the destructive behavior of the SNMS, so each measurement demanded a brand new sample. In order to obtain some information about the chemical state of the samples, XPS measurements were performed at the interface of the as-deposited samples and in the product layer of an annealed one by a PHOBIOS HSA3500 100 R6 (SPECS) X-ray photoelectron spectrometer. To gain 3D information on the process, atom probe supporting measurement were done, using a laser-assisted tomographic atom probe unit (LA-TAP) [110]. The instrument has a delay line detector system with 120 mm diameter and an aperture angle of 30°. Optimal measurement conditions have been achieved by using UV-laser light (340 nm wavelength) with 220 fs pulse length, ~0.2 μJ pulse energy and 200 kHz repetition rate. For these investigations a layer system of 20 nm Cu/40 nm a-Si was deposited onto field developed tungsten tips (W). The samples were annealed in ultrahigh vacuum conditions (p<10-7 mbar).

Let's focus our attention now on the region of interest of our samples. SNMS depth profiles of the as prepared and of their annealed pair (408 K, 12 hours) show the growing region of the new phase marked by the detected CuSi molecules.

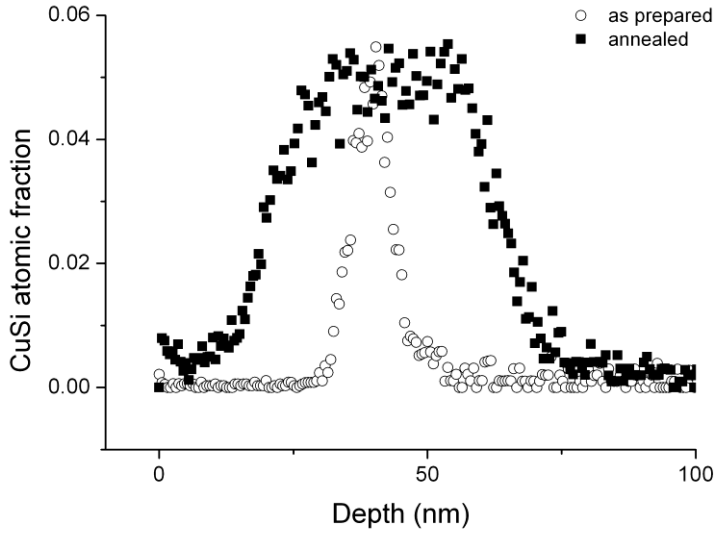

Figure 44 Recorded (28+63 amu) signal of CuSi molecule (for the as-deposited and an annealed sample – 12 hours) that was followed during the measurements indicating the growth of the product Cu_3Si layer [109].

The interface positions were determined by profilometer measurements, while the depth scale was determined from the sputtering time- expecting a constant sputtering rate. Since the XRD measurement we performed on the sapphire substrate showed that the growing phase is Cu_3Si so thus the product layer marked by the CuSi molecules in the SNMS profiles should refer to this phase consequently.

The 10 nm wide initial merged region, that we found in the as-prepared samples is not unique and comes from the deposition technique as an usual artifact of it that caused by the mixing of the incoming energetic Cu with the Si atoms at the interface during preparation. Let's note that instead of the existence of this mixed section the gained curves around the interface are smooth, i.e. we found no traces of a Cu_3Si layer, unlike it was indicated by others (Ou et al. [102]). The XRD, XPS and APT measurements supported these initial and latter developed conditions as you will see later.

XRD measurements were performed on as-deposited and annealed samples in order to check whatever any crystalline newly grown Cu_xSi_y phase exist in the as deposited sample or not and that whichever phase continue to grow afterward during the annealing. In case of the as-prepared samples we could not identify any peak corresponding to any CuxSiy phases. This indicates that there could be very low amount – if any – Cu_3Si or any other possible crystalline phases in the as-prepared samples. In the sample annealed for 18 hours at 408 K, however, the peak <1120> belonging to the hexagonal Cu_3Si could be easily identified.

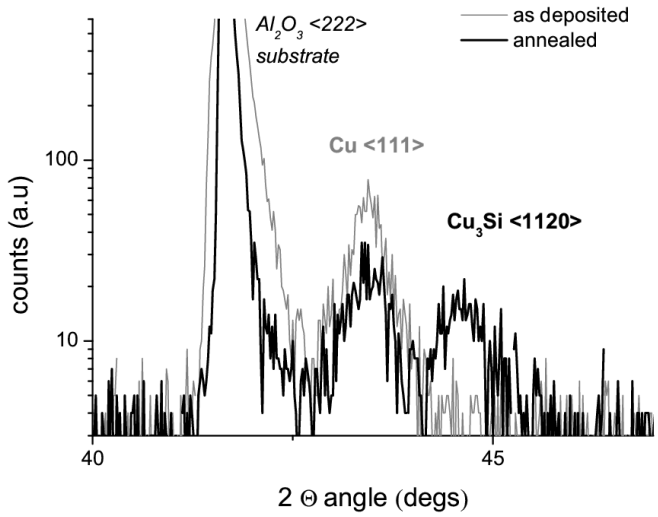

Figure 45 Result of the XRD measurements done on sapphire substrate before and after the annealing at 408 K for 18 hours [109].

XPS spectra were recorded at the interface and in the pure Cu layer of the as deposited sample and inside the Cu_3Si phase in the annealed one. The case of the annealed samples shows clearly that the position of the peak corresponding to the Cu 2p photoelectrons shifted compared to the one recorded in the pure Cu layer. This shift did not appear at the interface of the as deposited counterpart sample highlighting the role of the heat treatment in the phase formation.

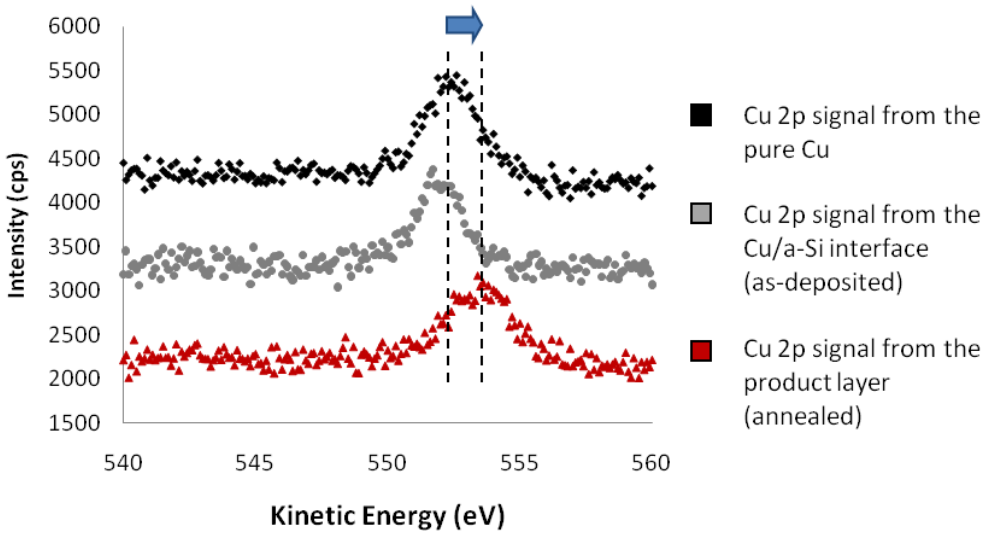

Figure 46 Three individual XPS measurements recorded at the interface and in the pure Cu layer of the as deposited sample and inside the Cu_3Si phase in the annealed one. The results show the shift of the Cu 2p photoelectrons in case of the annealed sample in the product layer compared to the as-deposited sample [109].

III.3.1.2 Asymmetrical phase growth in triple layered, sandwich structure of Cu and a-Si

In the previous investigation, we have found a very fast phase formation that resulted in a ~20 nm thick product layer prior to the latter linear phase growth. For this reason, we continued our study by preparing Cu_{30nm}/a-Si_{30nm}/Cu_{30nm} and a-Si_{30nm}/Cu_{30nm}/a-Si_{30nm} sandwich layered samples. These samples were prepared and analyzed under vacuum conditions in the same experimental setup and under similar conditions as it was described for the previous experiment (see in II.A.1.). However at this time the structure was chosen to be a triple layer in order that both interface configurations (the Cu on a-Si and its reverse form) could be investigated simultaneously. The annealing temperature was set to 438 K. After the sample preparation a part of the samples were kept and analyzed in as-prepared state while other parts were annealed prior to the SNMS analysis.

III.3.2 Results

III.3.2.1 Phase growth of Cu_3Si

We used an integral form of the linear parabolic growth for determining the kinetics of the shift of the interfaces and the growth rate of Cu_3Si phase [108,111,112,113].

$$\frac{x^2}{2D} + \frac{x}{K} = t - t_0\,, \tag{40}$$

where x, t and t_0 are the thickness the time and an integration constant, respectively. D and K, apart from a constant factor in the order of unity [113], are the interdiffusion coefficient (assumed to be composition independent) in the phase and K is an effective interface rate coefficient ($K^{-1}=K_1^{-1}+K_2^{-1}$ where K_1 and K_2 belong to the interfaces bordering the phase [113]). In that case, when we investigate the shift of a given interface, K refers to the shift of this separate interface in interest of course [114].

Figure 47 shows the obtained shifts of the interfaces as a function of the annealing time achieved by the above described combined technique of SNMS and profilometer measurements. To improve the reliability of the above mentioned profilometer measurements, however it is worth to mention that each produced crater was measured for several times and in several directions to obtain an accurate averaged depth value.

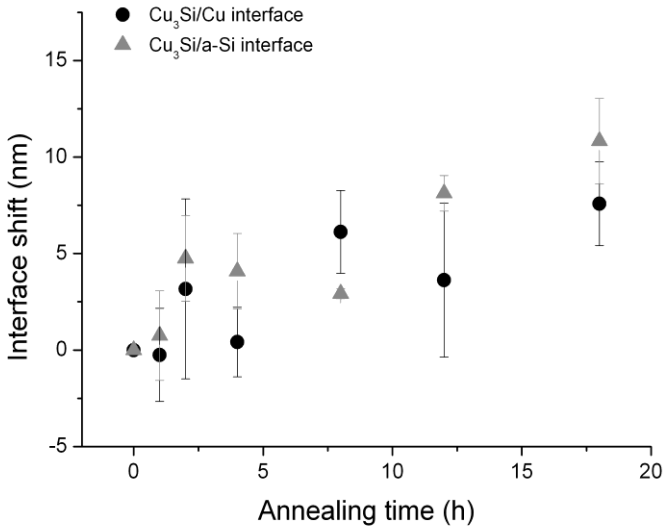

Figure 47 Shift of the interfaces surrounding the product layer (subtracted the quickly nucleated initial thickness of 20 nm that appeared after t_0 – see also text) [109].

The zero point of these data points comes from the interfaces position of the sample annealed for t_0, as mentioned previously. Surprisingly even in the case of t_0 a quite wide 20 nm thick Cu_3Si layer had already formed in the sample. Interestingly no significant difference is observable between the consumptions of the Si and Cu, seemingly they decreased equally, though the 1:3 stoichiometry would suggest a much stronger of Cu decrement compared to the Si. One considering the grain-boundary diffusion of Si into the Cu layer although could explain these results: The diffusion of Si into the grain boundaries of the polycrystalline Cu layer can cause the shrinkage of the Si layer and the expansion of the Cu. Accordingly, the interface shift caused by the phase formation can be altered by previously mentioned GB diffusion. As can be seen in Figure 43, Si shows a possible mark of segregation near the surface and well measurable average Si composition throughout the whole Cu layer. On the other hand the Cu signal drops to zero immediately when it reaches the Si layer. This clearly shows that the solid state reaction is accompanied by significant Si grain boundary diffusion into the Cu layer. APT measurements carried out at 438 K support this picture (see Figure 49 and Figure 50 later).

The obtained data points on Figure 47 show very similar shift rates of the two interfaces that suggest that the effective parameters (indicating that at least two types of atomic jumps – grain boundary and bulk – are involved) determining the shift have similar values. Using a linear fit $K_1 \cong K_2 = (1.5 \pm 0.5) \times 10^{-13} ms^{-1}$ was obtained.

The analysis of the growth of the full product layer was carried out as wells. In Figure 48a the thickness of the Cu_3Si phase is plotted versus square root of the annealing time, and versus the annealing time in Figure 48b and on a double logarithmic scale in Figure 48c.

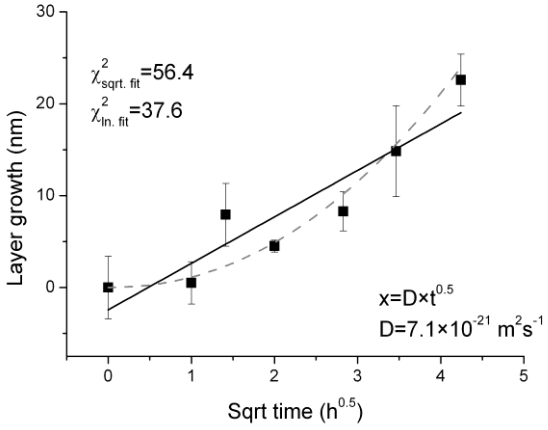

(a)

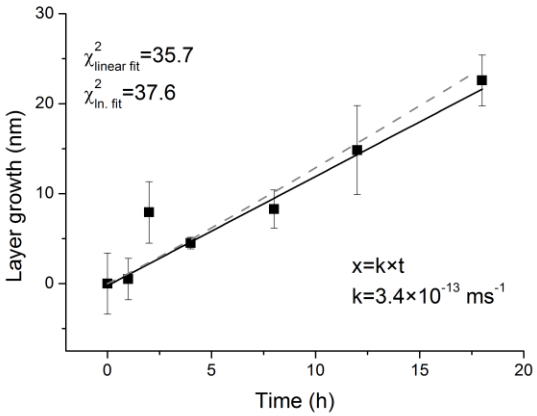

(b)

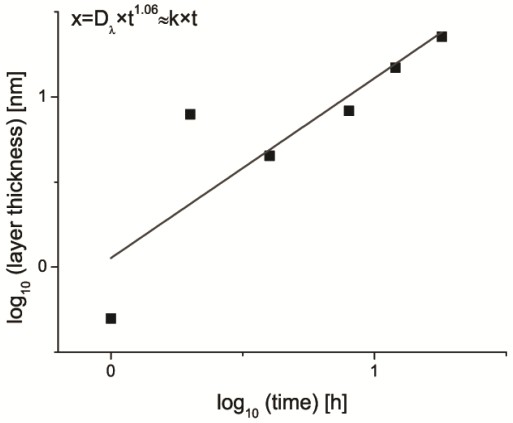

(c)

Figure 48 Evolution of the total thickness of the Cu_3Si layer (a) as a function of the square root of the time, (b) as a function of the time (linear) and (c) on a double logarithmic scale respectively. The solid black lines represent the straight line fitted to the data in the given representation. The linear growth assumption and the log-log fitting provide comparable results. For better convenience, the power function obtained from the fitting on the log-log scale is also plotted by dashed gray curves in figs. a) and b). The $\chi 2$ of the different fitting are also shown [109].

Even a crude comparison reveals that the assumption of a linear growth rate offers a much better description than the standard parabolic model. The χ^2 of the former model is less than two thirds of the latter (35.7 and 56.4 respectively). Since all fitting functions contain the same amount of free parameters, a direct comparison of the χ^2-s is possible.

We may, therefore, conclude that we observed an anomalous, linear growth, process laying in the so-called super diffusive regime [115].

Thus, these results may also contribute to the understanding of anomalous growth processes in solids besides their importance in other fields (metal-silicon contacts [116], metal induced recrystallization). From the fitting with the linear term in equation (40) a linear growth (see Figure 48b) a reaction rate coefficient of $K = (3.4 \pm 0.4) \times 10^{-13} ms^{-1}$can be deduced at 408 K. As it is expected, both Cu_3Si/Cu and Cu_3Si/a-Si interfaces contribute to the growth equally and thus $K \cong 2K_1$ (or $2K_2$) within the error bars.

Let us now turn back to the fast formation of the Cu_3Si phase during the annealing. This somehow suggests that some precursor layer should exist between the Cu and Si even in the as-deposited case. This is also supported by the relatively wide 10 nm thick transition zone between the Cu and Si in the SNMS depth profiles.

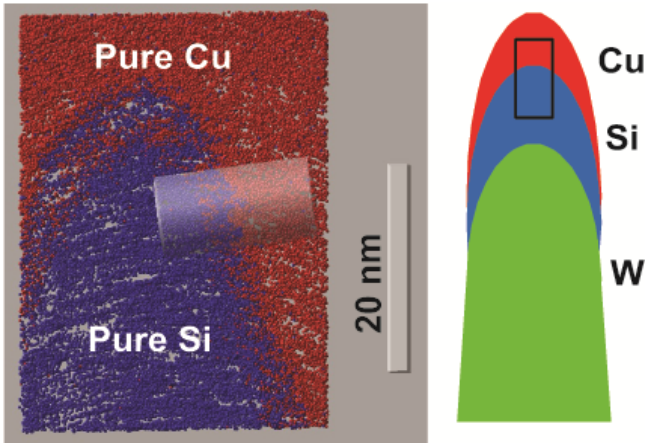

Figure 49 A section from an atom probe reconstruction of a layer stack in as-deposited state from an as-prepared specimen (Cu atoms are represented by red/lighter, while Si atom by blue/darker balls). A relatively broad mixed zone at the interface is visible. The sketch of the geometry and the position of the section in the specimen can be seen on the right hand side [109].

In Figure 49, a section from an atom probe reconstruction of a layer stack in as-deposited state can be seen. A mixed region (of a few nanometer) containing Cu as well as Si atoms is clearly observed. Analysis cylinders, were placed across the mixed zone perpendicular to the

interfaces (perpendicular to isoconcentration contours) to determine local concentration profiles. Figure 50 presents such a composition profile (the cylinder diameter was 4 nm, while section length was 0.2 nm, no moving average was used to smoothen the data). This (local) composition profile demonstrates a relatively broad (5-10 nm) more or less smooth transition; the apparent Si and Cu richer domains visible on Figure 49 are already washed out.

We observed that two stages can be distinguished in the solid state reaction during the formation of the Cu_3Si phase. The first one is a very rapid process which creates a more or less 20 nm thick intermetallic layer - which layer was already present after the "t_0" annealing. This process was followed by a very slow growth which proceeds linear in time and duplicates this initial width only after around 18 hours at 408 K

However in accordance with the results of the SNMS depth profiles, namely clear signs of segregation appeared on the surface region of the sample measured by APT (after annealing at 438 K for 5 h) in Figure 51, the APT device found another segregation zone, that appeared at the Cu-Cu_3Si interface too, which one was not present on the SNMS profiles. The distribution of the Si atoms in the Cu layer are not homogeneous, there are stripes of higher concentration of Si atoms and in between zones of pure Cu. A more careful analysis, using multiple sections from different direction revealed that these zones are interconnected, thus this is a result of the Si diffusion in the Cu grain boundaries. Accordingly the main features of the SNMS intensity curves are well supported by direct local analysis.

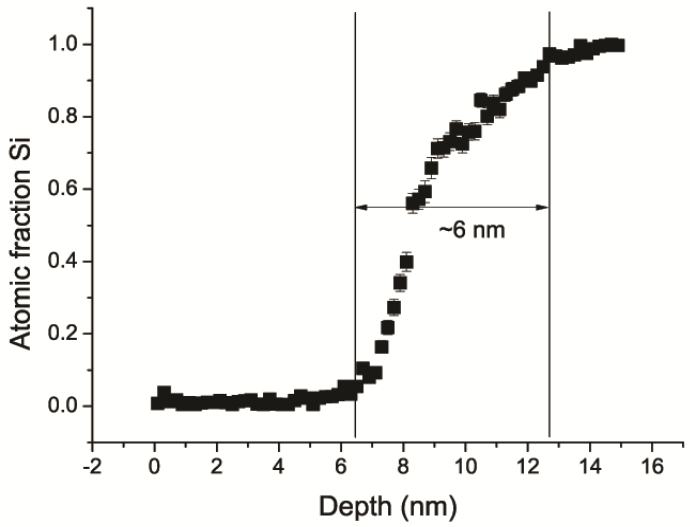

Figure 50 Si composition profile within the analysis cylinder. No trace of the Cu_3Si phase in the as prepared state [109].

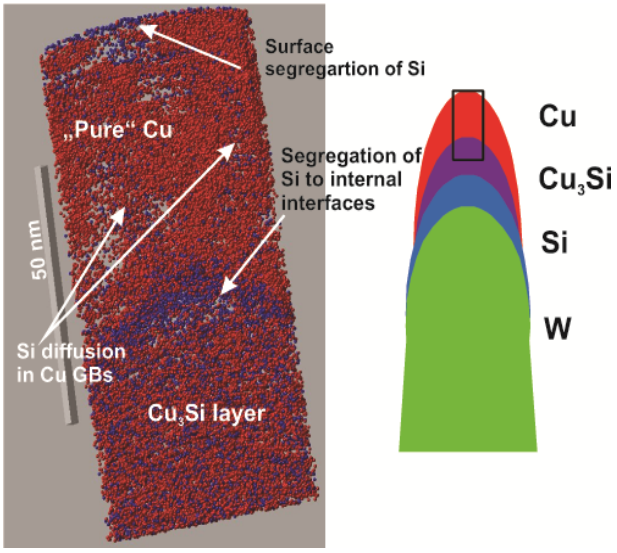

Figure 51 Section of an APT measurement after annealing the specimen for 5 h at 438 K; a well-developed silicide layer is visible in the bottom. Si segregation to the free surface and at the Cu/Cu_3Si interface as well as Si rich stripes appear in the Cu (most probably GBs). The sketch of the measurement geometry can be seen on the right [109].

III.3.2.2 Asymmetrical phase growth in triple layered, sandwich structure of Cu and a-Si

In the depth profiles of the as-deposited samples (Figure 52) the smooth interfaces at both sides of the inner amorphous silicon layer suggest the good initial quality of the samples. Showing no measurable trace (by SNMS) of phase formation that would appear during the preparation part of the procedure however it is worth mentioning that there is a minor intermixing that is observable and marked by the slightly wider interface at the upper Cu/Si contact.

On the other hand when we take a look at the samples after annealing (at 438 K) a quite remarkable difference is visible between the two interfaces (see Figure 53).

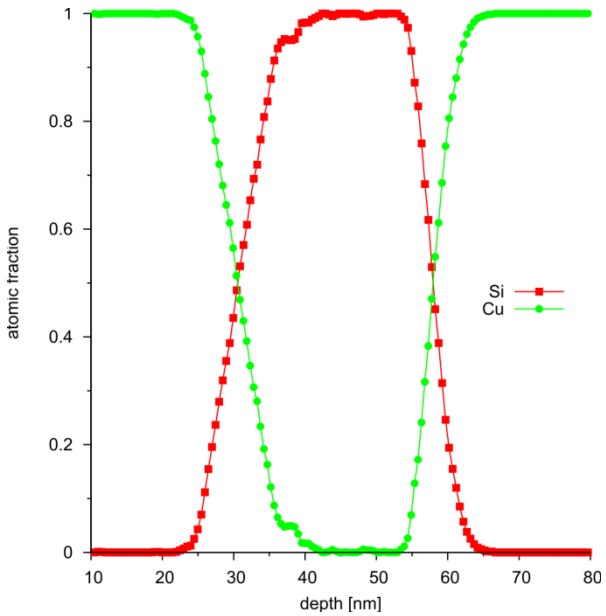

Figure 52 Concentration versus depth profile of the as-deposited, sandwich layered Cu/Si/Cu sample.

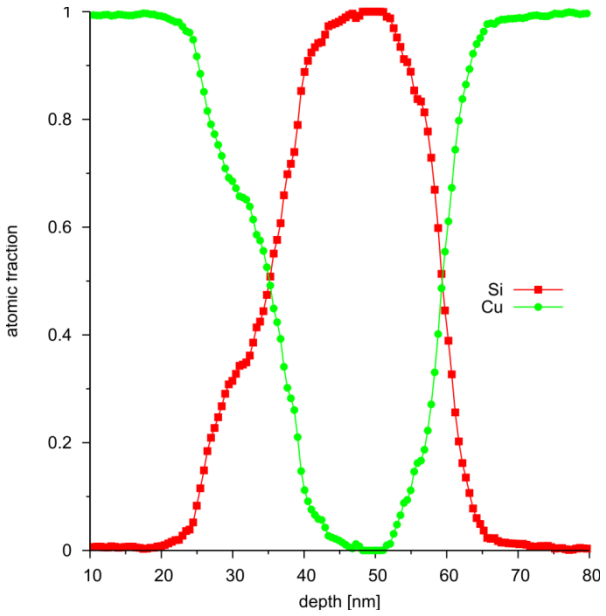

Figure 53 Concentration versus depth profile of an annealed (at 438 K), sandwich layered Cu/Si/Cu sample. The interface remained sharp in the case when the Si was deposited on the Cu, meanwhile clear sign of the phase formation appeared in the case of the other interface.

The upper interface shows a significant change compared to its as-prepared counterpart, but the bottom interface shows hardly any real change or sign of phase formation. The phase formation of the upper Cu/a-Si interface fast development is in similar range with the one

found in the previous experiment [109]. These results have been supported by APT measurements as well and will be discussed in details in [117].

Compare the quite dense fcc structure of the Cu to the a-Si is very different. The latter one has relatively high free volume in which a pretty fast interstitial diffusion is allowed for some metals. Taking into account the differences in their transport properties such as previously mentioned, that is the e.g. the pretty high diffusivity of Cu in a-Si with its quite low activation enthalpy and the silicon's segregating behavior in this system making this two-component system a little bit more complex.

Starting from the above ones depositing a sandwich structure of Cu/a-Si/Cu would allow the investigation of the behavior of the participants in both deposition modes. Now, comparing the depth profiles of Figure 52 (as-deposited) and Figure 53 (annealed) one can see that in the case when the Si was deposited on top of the Cu (bottom interface) even if the Cu tends to diffuse fast into the Si, segregating behavior dominates the process (thermodynamically favorable) [118,119]. On the other hand when the second Cu layer is deposited on top of the a-Si, it is non-favorable for the system and the Cu atoms diffuse into the a-Si layer forming a wide intermixed region. That is the reason for the observed deviation between the interfaces. The latter phase formation can take place only if there are large enough nuclei (larger than a critical size [120]) from which the process can strike out. Since the initial conditions prior to the annealing procedure or during it are suitable for the nucleation only in that case when one deposits the Cu on top position the nucleation and the latter phase formation will set off from that interface, while the other one remains more or less intact.

Samples with reverse stacking (a-Si/Cu/a-Si) were prepared as well. Those samples behaved similarly, i.e. in that case the lower interface became more diffused and the latter nucleation and phase growth started from that interface, meanwhile the upper interface where the Si takes a top position remained more or less sharp.

This behavior of the reverse samples excludes the possibility that these diffused regions for the two kinds of samples could be some SNMS related artifact.

III.3.3 Conclusions

We showed that instead of the expectations of the literature, we found that the Cu_3Si has formed at the interface and continued to grow following an anomalous kinetics proportional with time. Furthermore, equal contribution to the total phase growth of both interfaces has been shown. The proper interpretation of this anomalous growth kinetics needs further investigations to decide whether it is a consequence of the reaction control or the high diffusion asymmetry of the components which can also lead to anomalous growth kinetics [111,121]. The sudden formation of the thick crystalline Cu_3Si layer right after the T_0 heat

treatment is observed, that could refer to the presence of some small amount of precursors under the limits of detection of the XRD and possibilities of XPS. The APT analysis showed that just after the deposition precursors of intermixed regions (between the as deposited Cu and Si) are already present, which probably can be easily transformed to a homogeneous crystalline, Cu_3Si layer in the very early stage of the process. Cu_3Si is a possible initiator of the metal induced crystallization and can play an important role in Si-based Li-ion batteries, Blue ray discs, or solar cells from industrial point of view. Kinetic data, especially low temperature kinetic data for the battery applications is therefore greatly important. Based upon the linear growth relation, we found a reaction rate of $3.4\pm0.4\times10^{-13}$ ms^{-1} or roughly 1 nm/h at 408 K.

In the second series of experiments on this system performed on tri-layered Cu/a-Si/Cu specimens with layer thickness of 30 nm for each we investigated the nucleation of the Cu_3Si phase with the combination of SNMS and profilometer techniques. The comparison between the as-deposited and the annealed samples revealed a significant difference in phase formation depending on whatever the Cu or the a-Si was in relative top position during the sample preparation. The results showed that, after a short time annealing, Cu_3Si phase have been formed at the top (Cu/a-Si) interface while the bottom (a-Si/Cu) interface remained unchanged. The answer for this behavior comes from the segregating behavior of Si and the quite low activation enthalpy and high diffusivity of Cu in a-Si. Since the system tends to reach a thermodynamically favorable state, it moves toward that direction where these properties or behaviors provide the lowest energy state for the system. In this case in hand (Cu/a-Si/Cu/substrate), it means that the Si which has a tendency for segregation, will dominate the process. In case of the bottom interface results in a sharp and more or less intact interface. In the reverse deposition case the existence of an diffused region is much more preferable for the system which one in turn gives a push for the latter nucleation and phase formation.

These results can hopefully help to extend the understanding of the early stage solid state reactions in the Cu-Si system

My own contribution: *During these experiments my duty was the sample preparation; furthermore I have performed profilometer, 4 wire resistance, SNMS and XPS measurements. Furthermore, I have evaluated the experimental data.*

III.4 Silicene

During my stay in Marseille, France, I studied the thermal behavior of one or two monolayers of silicon deposited under ultra high vacuum conditions on silver substrate [Ag(111)]. This study was performed in the more general frame of the study of silicene growth on this metallic substrate.

Silicene is a homolog of graphene it is 1 monolayer thick material that consists of silicon atoms with honeycomb structure.

Before we would dig any deeper in the topic of silicene I have to take some notes about the graphene as the historical predecessor of silicene.

In case of carbon the sp2 and sp3 hybrid states play a very important role in the formation of the two main structures. In sp3 state when all atomic, s and p, orbital participate in the hybridization and form four equivalent orbitals, then the diamond structure is formed. In case of the sp2 state when the s and the p orbitals merge to form three equal hybrid orbitals leaving only the pz atomic orbital unaffected corresponds to the honeycomb structured, 1 monolayer thick form of carbon, namely the graphene, which is the most stable form.

Andre Geim and Konstantin Novoselov for the first time were able to separate a single sheet of graphene by exfoliation. The latter performed experiments showed features beyond expectations. This honeycomb structured system of graphene has cone shaped band structure with zero-gap at the corners of its Brillouin zone (BZ) [122,123] **(**Figure 54**).**

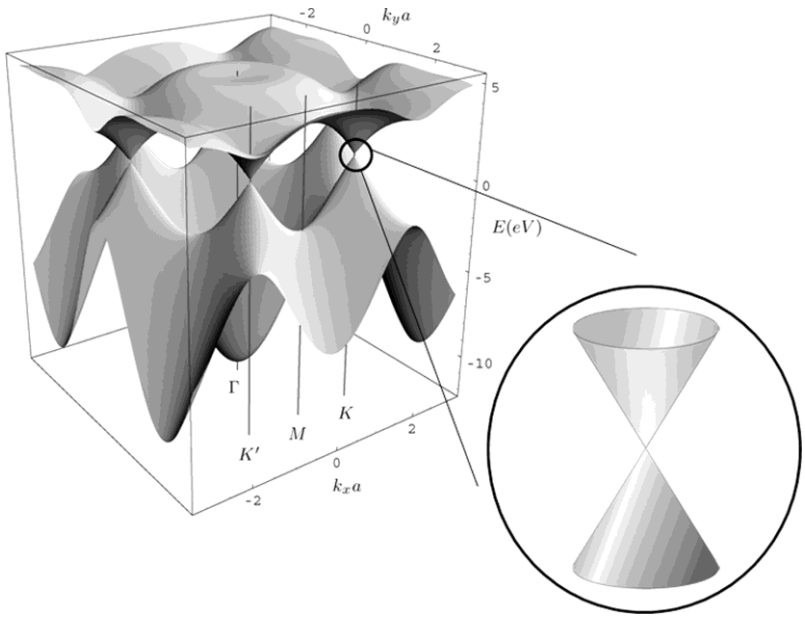

Figure 54 Honeycomb structured system of graphene that has cone shaped band structure with zero-gap at the corners of its Brillouin zone (BZ) [124]

It means that at the 6 corners [called Dirac Points (namely the K and K' points)] of the hexagonal shape BZ the conductions and valence bands meet at a point (where the Fermi level takes place). According to the calculations of previous investigations ([125]and the references therein) the charge carriers considered as massless, Dirac fermions i.e relativistic particles that travel with a speed close to the speed of light. Graphene however above this showed other interesting behaviors as well. The properties of graphene grabbed the imagination and dreams of many scientists and research groups around the globe and drove them into multifold experiments and investigations about the material that resulted in numerous publications.

The zero-gap at the Dirac Points of free standing graphene however means a significant drawback for an electric field modulated logic devices not mentioning the fact that their integration into the silicon based technology is till a matter of question.

Thus recently the focus turned to the other members of the group-IV semiconductors namely to Si and Ge or more precisely to their honeycomb structured form, the silicene and the germanene (**Figure 55**). Their electric properties are just as promising as of their predecessor without the problem of the questionable integration into the present silicon based technology.

Unfortunately, contrary to carbon for which the above mentioned two crystal structures exist in the nature, for silicon and germanium, only the diamond structure is known to form naturally.

The problem is that the sp3 hybridization form of silicon is much more stable and thus preferred (the same stands for Ge). However ab-initio theoretical calculations have shown, that a single sheet of silicene with mixed sp2-sp3 hybridization is also thermodynamically stable [126,127]. Indeed, the first theoretical works were very promising and they showed that silicene has an intrinsic stability with electronic properties close to that of graphene. However its atomic structure is not perfectly plane but presents a buckling in relation to mixed sp2-sp3 hybridization.

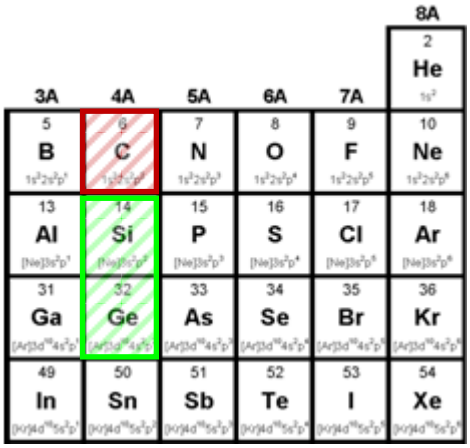

Figure 55 A small part of the periodic table. In the picture we highlighted the C, Ge and the Si which ones represent the graphene, germanene and the silicence respectively.

From an experimental point of view, few years ago, single sheets, nano-ribbons and nano-stripes of silicene were synthesized on Ag(111), Ag(110) and Ag(100) substrate respectively [128,129,130]. After these first findings many groups, all around the world, have confirmed the existence and possible production of silicene sheets on Ag(111). Silicene sheet has been synthesized also by segregation of silicon on Zirconium diboride thin films deposited on a silicon (111) wafer [131], and very recently by deposition of Si on Ir(111) [132] However unlike graphene the synthesis of a freestanding form of silicene is still the matter of research.

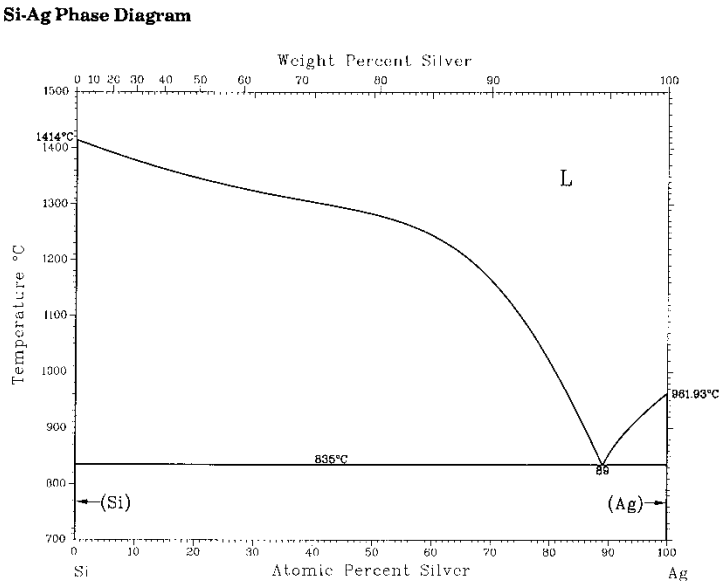

Figure 56 Equilibrium phase diagram of the Ag-Si system. [76]

Growth of silicene on Ag(111): state of the art

3 main reasons why silver is an ideal substrate for growing silicene:

- Silver and silicon show a very strong tendency to the phase separation in other words there is no predisposition to form any silicide.
- The limit of the solubility of silicon in silver, if there is one, is very low, as it can be seen on the bulk phase diagram (Figure 56).
- There is a perfect match between the crystalline structures of silicon and silver i.e. there is a natural perfect match between four nearest neighbors of Ag distances (1.156nm) and three unit cells of the (111) surface of silicon (1.152nm).

On the (111) face, it has been shown (see later) that depending on the growth conditions i.e. on the substrate temperature as well as on the deposition rate, the deposition of one monolayer (1ML) of silicon can result in at least 4 different superstructures, all linked with the perfect match. In other words, all superstructures observed correspond to a perfect epitaxie of the silicene layer rotated relatively to the Ag(111) substrate. At a substrate temperature in between 100 and 180°C associated to a low deposition rate (~ 1ML in 2 hours) a pure (4x4) superstructure is observed (by LEED and STM). At more elevated substrate temperatures (~ 300°C) and a more rapid deposition rate (1 ML in 15 minutes) a quasi-pure $(2\sqrt{3} \times 2\sqrt{3})R30°$ is observed (by LEED and STM). At intermediate temperatures of the substrate the mixture of (4×4) and the $(\sqrt{13} \times \sqrt{13})R13.9^{\circ}$ structures were observed (by LEED and STM) [136,133]. Recently at this intermediate temperature in addition to these superstructures another structure the $\sqrt{7}$x$\sqrt{7}$, which was predicted theoretically [136], has also been reported experimentally [134].

All these structures have been more or less confirmed and observed by different groups. However the (4×4) and the $(\sqrt{13} \times \sqrt{13})R13.9°$ superstructures are systematically reported, it does not stand for the $\left(2\sqrt{3} \times 2\sqrt{3}\right)R30°$ structure, which appears to be very sensitive to the growth conditions. Furthermore, even if we can understand why we need at around 180 °C a low deposition rate (it is likely in relation with the silicon surface diffusion) it is less obvious why we need a much higher deposition rate at 300°C.

Since the $\left(2\sqrt{3} \times 2\sqrt{3}\right)R30°$ structure is still a matter of debate in the field, in order to understand why is that some groups did not observe it and why it is so important to apply a high deposition rate, we have decided to follow the change, after the silicon deposition (at 300 °C), of the surface composition versus the annealing time at the same temperature.

Indeed, an unexpected dissolution process of silicon in the bulk silver could explain both observations. Thus, hereby a combination of LEED, AES and STM measurements is reported concerning the thermal behavior of the (4×4) and the $\left(2\sqrt{3} \times 2\sqrt{3}\right)R30°$ superstructures. After the deposition of 1 ML of Si at the temperatures which allows us to obtain the superstructures of (4×4) and $\left(2\sqrt{3} \times 2\sqrt{3}\right)R30°$ the sample was annealed at 300°C and the surface concentration of silicon was followed by AES. The effect of the annealing has been recorded after the growth of the (4×4) and that of the $\left(2\sqrt{3} \times 2\sqrt{3}\right)R30°$ superstructure.

III.4.1 Experiments

The sample-cleaning, preparation and the latter experiments were performed under ultra high vacuum conditions achieved by the 3 step vacuum system consisting of a primary rotation pump two turbo pumps and three separate ion pumps (see the experimental setup in Figure 4). Thanks to the three ion pumps the ultrahigh vacuum conditions could be maintained in all the three vacuum chambers, namely the the sample preparation, the AES & LEED and the STM chambers. In this way we could keep the pressure in the range of 10^{-9} - 10^{-10} mbar during the measurements.
In order to get a clean Ag surface in each case we cleaned the Ag(111) substrate with ion bombardment which was followed by a ~12 hours long heat treatment at 450-500 °C in order to regain the crystal structure on the surface.
Note that the temperature was measured with a thermocouple placed close to the sample (approximately 1 cm). It means that there is a difference between the absolute temperature and the measured one, which is underestimated.

After this step, in order to obtain the (4×4) superstructure the sample was heated up and held at 180°C in front of the evaporator, in which we passed 9A through the silicon wafer for 3 hours during the deposition. In order to obtain the $\left(2\sqrt{3} \times 2\sqrt{3}\right)R30°$ superstructure the

sample was heated up and maintained at 300°C in front of the evaporator (running with 12A this time) for 20min (see the schematic drawing in (see Figure 59).

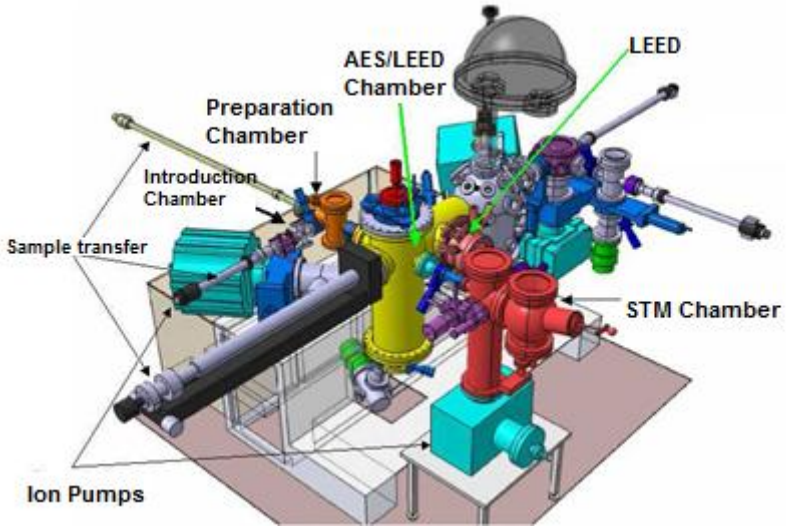

Figure 57 The experimental setup we used during our experiments, consist of individual chambers for the ion bombardement for the cleaning of the substrate, and the measurements of AES, LEED, STM. [135]

A piece of Si wafer was used for the Si deposition by evaporation (Joule heating) see in Figure 58 The Si wafer used during the evaporation. [135].

Figure 58 The Si wafer used during the evaporation. [135]

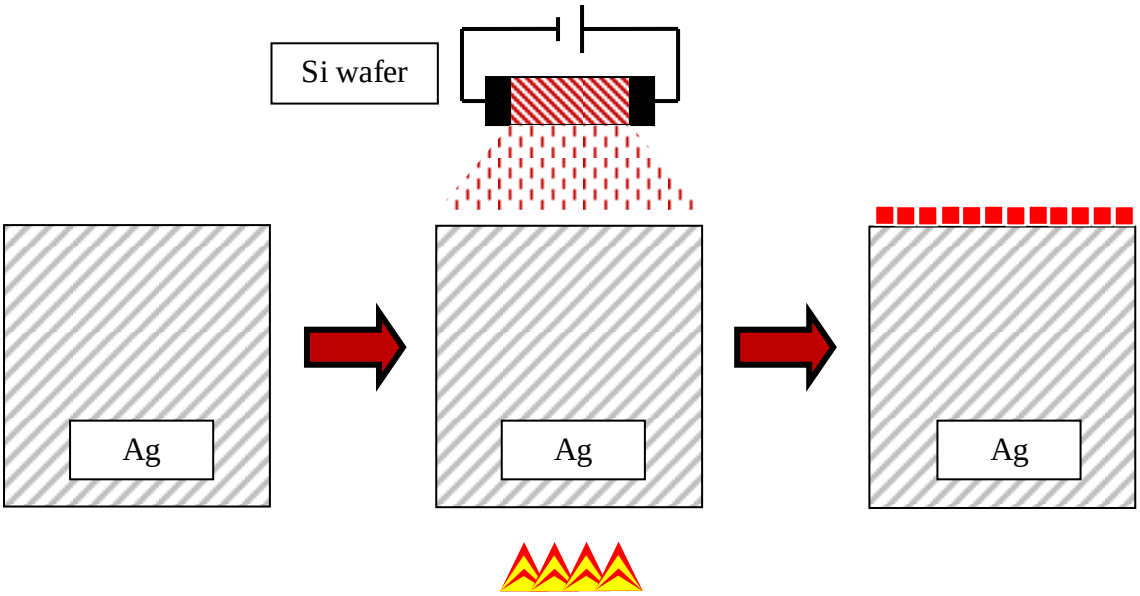

Figure 59 Schematic figure of the process of evaporation of Si on the Ag(111) substrate.

The dissolution of Si was followed by the AES at 300 ^{o}C in each case (Figure 60) till the Si signal dropped to 0, and just before each AES measurement LEED pattern was recorded in order to identify the deposited layer structure.

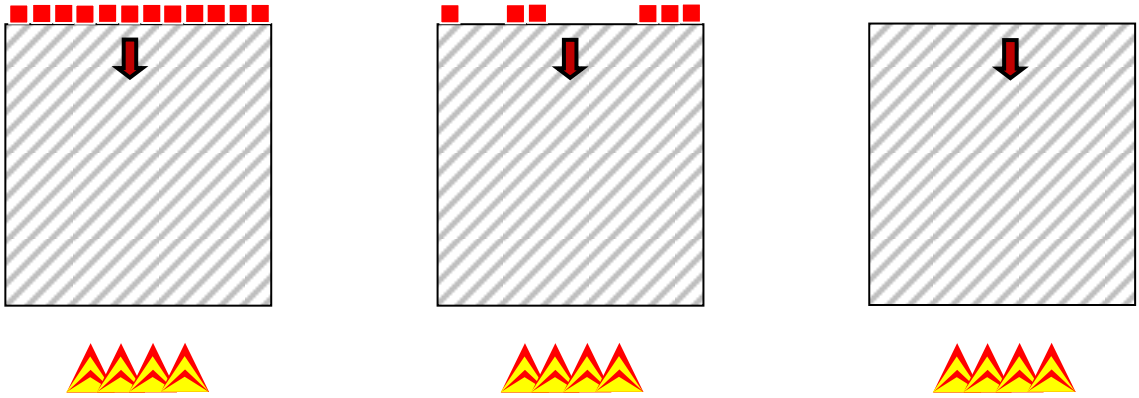

Figure 60 Schematic figure of the process of dissolution of Si in the Ag(111) substrate.

III.4.2 Results

III.4.2.1 Solubility limit in Ag-Si system

During the AES measurements we followed the peaks below:

1) Silver: MNN at 351 and 356 eV.
2) Silicon: LMM 92 eV.

and checked the peaks of carbon (272 eV) and oxygen (500 eV) for any observable trace of contamination.

According to previous experiments done on Si/Ag(111) system by Y. Colignon et al. a layer by layer growth mode of Si on Ag(111) can be deduced [(Figure 2.1) in [135] with the ratio of ISi/IAg around 0.5 that equals to one monolayer of Si on Ag(111).Thus we chose this 0.5 value of ISi/IAg ratio of Auger signals as a marker of the growth of the first monolayer and tuned our experiment in order to obtain such a ratio of Si and Ag as an initial condition for our experiments.

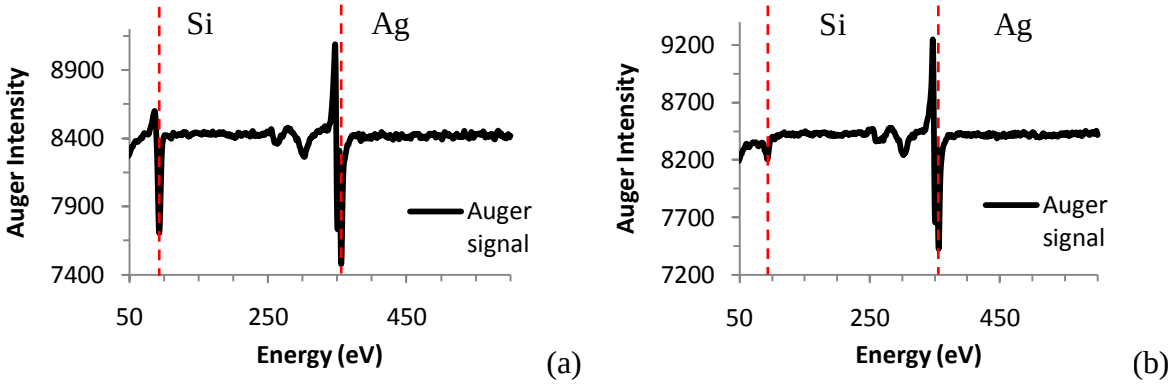

Figure 61 A typical Auger spectra recorded a) just after the deposition of 1ML of Si (performed at 300°C at this time) and b) after annealing (at 300°C).

Neither of the spectra in **Figure 61** show any sign of impurities or contamination which could be present on the metallic substrate due to Carbon, Sulfur or Oxygen. Furthermore in **Figure 61** we can also see that the intensity of silicon has strongly decreased without any shift on the energy scale which means that there was no modification in the nature of the chemical interaction between the silicon and the silver during the annealing.

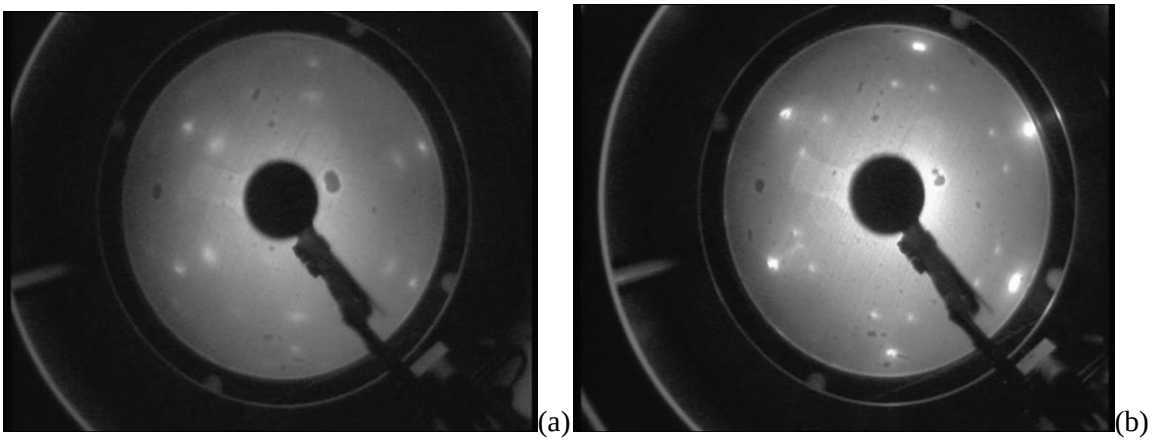

Figure 62 One can see the typical LEED patterns obtained after the deposition of 1 ML of Si on the Ag(111) substrate a) at 180°C and b) at 300°C, at which temperatures the 4x4 and the $\left(2\sqrt{3}\times 2\sqrt{3}\right)R30°$ superstructures form respectively.

The variations of the Auger intensity ratio ISi/IAg versus the annealing time have been recorded at 300°C after the growth of the (4×4) and $\left(2\sqrt{3} \times 2\sqrt{3}\right)R30°$ superstructures. Note that the same temperature (300°C) have been used during the growth and during the annealing time of the $\left(2\sqrt{3} \times 2\sqrt{3}\right)R30°$ superstructure, while in case of the (4×4) superstructure, the kinetics were recorded just after the growth which means that the temperature had to be increased rapidly from 180°C to 300°C.

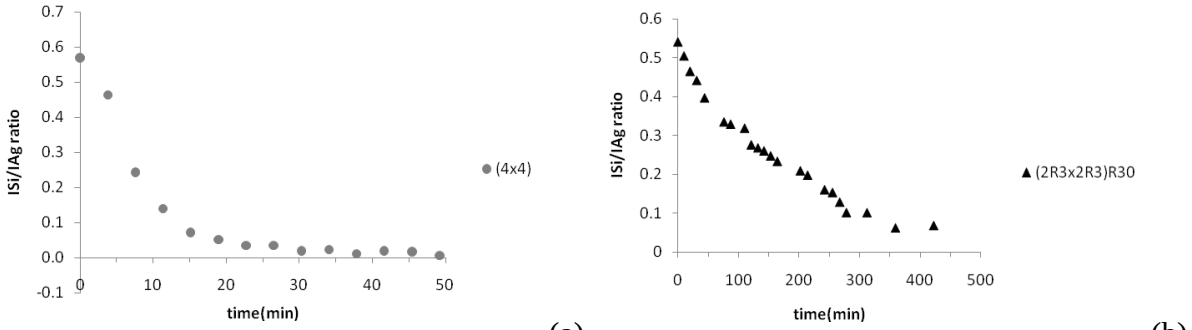

Figure 63 Dissolution of 1 ML of Si a) in case of the superstructures of (4×4), marked by grey circles and b) of $\left(2\sqrt{3} \times 2\sqrt{3}\right)R30°$, marked by black triangles

Two, markedly different curves were obtained for the two superstructures. There is a quite fast decrease of the Si in case of the (4×4) structure and a much slower one for the $\left(2\sqrt{3} \times 2\sqrt{3}\right)R30°$ structure.

The decrease of the silicon Auger signal is concomitant with the increase of the silver Auger signal. It can be explained by either a dissolution process of silicon in the bulk of silver or by a de-wetting of the silver surface by the silicon layer.

The origin of the two, markedly different shape of dissolution could be the signature of their intrinsic stabilities. In other words, the faster dissolution kinetics of the (4×4) superstructure would be the signature of a lower stability in comparison with the $\left(2\sqrt{3} \times 2\sqrt{3}\right)R30°$ structure. However, we have to be careful with this conclusion since in case of the (4×4) super structure the thermal history is not the same. Indeed the Si deposition was performed at 180°C while in case of the $\left(2\sqrt{3} \times 2\sqrt{3}\right)R30°$ the deposition took place at 300°C. The significant difference between these two deposition temperatures could explain the difference observed on the dissolution kinetics. Indeed, likely there is an increase of the Si content in the upper volume of the Ag substrate during the deposition in case of the $\left(2\sqrt{3} \times 2\sqrt{3}\right)R30°$ structure and in turn it could affect the latter dissolution process and slow it down (due to the decreased concentration gradient). On the other hand, in case of the (4×4) superstructure, we assume that the dissolution process can start when the sample reaches higher temperatures.

So, in order to determine at least the order of magnitude of the solubility limit of silicon in silver at 300°C, we can only use the dissolution kinetics of the (4 × 4).

To do that we used the following equation which assume that the dissolution process is only driven by a constant bulk diffusion coefficient and by the limit of the solubility (no segregation effect that could slow down the kinetics):

$$C_s(t=0) - C_s(t) = 2C_v(x \cong 0, t)\sqrt{\frac{Dt}{\pi}} \quad (41)$$

where, Cs(t) is the superficial concentration of Si as a function of time, Cs(t=0) is the initial superficial concentration of Si, while C_v(x=0,t) is the bulk solubility limit of Si in Ag close to the surface (x=0).

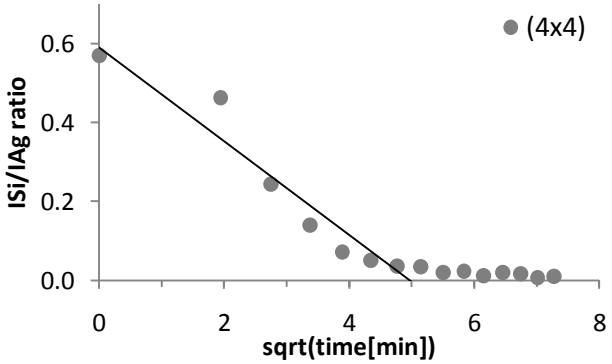

Figure 64 Dissolution kinetics of 1 monolayer of silicon forming a (4 × 4) superstructure recorded at 300°C.

We plotted the dissolution kinetics of 1 ML of Si with an initial superstructure of (4 × 4) in Figure 64, more precisely the variation of ISi/IAg ratio versus the square root of time. The non-linearity observed could be due to

i) the temperature rise from 180 to 300°C and/or
ii) the variations of the ratio ISi/IAg which are not exactly linear with the silicon surface concentration.

The average slope of this kinetics that we used in the calculation is drawn on the curve.

Usually the diffusion coefficient of Ge extracted from radiotracer measurements is used as the bulk diffusion coefficient of Si in metals, because of their similarity and the fact that Si does not have any usable radioactive isotope (the life time of the tracer is too short).

$$D_{Ge} = 0.084exp - (36500/RT)\ cm^2/s \quad (42)$$
$$D_{Ge} = 1E^{-15}\ cm^2/s \quad (43)$$

According to the structures given in ref [136] for the (4×4) superstructure we can deduce, the surface density of Si atoms is about 1.55E15 atom/cm^2. Using the tracer diffusion coefficient of Ge in silver given by [137].

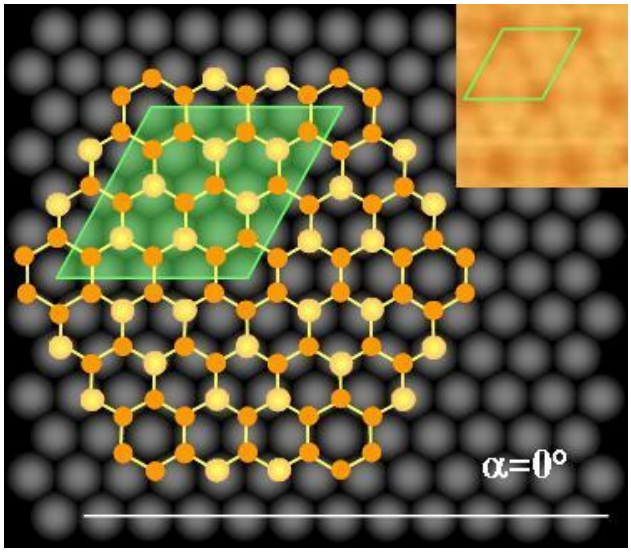

Figure 65 Atomic model of the (4×4) superstructure. [136]

From the kinetics shown in Figure 64and the previously listed parameters of Equation (40) we determined the limit of the solubility of silicon in silver at 300°C is between 1 and 2 at%.

III.4.2.2 Dissolution of a thicker silicon layer

In order to see the influence of the deposited silicon thickness we recorded (at 300°C) the dissolution kinetics of a larger amount of silicon deposition (at the same 180°C). The variations of ISi/IAg versus the square root of time are reported on the Figure 66. In these experiments, above, the calibration of the silicon amount was difficult mainly because in our system the evaporation was not constant with time due to the presence of a hot spot on the Si wafer. Nevertheless in order to estimate the silicon amount deposited, we used the calibration curve performed by C Leandri on Ag(100). According to this calibration, ISi/IAg ~ 1.45 corresponds to about 2 silicon monolayers (assuming that the growth mode was layer-by-layer type like on Ag(100) at RT).

The dissolution at 300°C of this thicker deposit is very different from the pure (4x4) structure (see in Figure 66). Indeed, at this time after the first quite fast and similar part, the Si concentration reached a plateau (around ISi/IAg=0.5-0.6), where the dissolution stops even after a quite long annealing time (> 3hours).
The LEED patterns observed just after the deposition of this ~2 Si ML and after the partial dissolution (on the plateau) are shown in Figure 67 respectively.

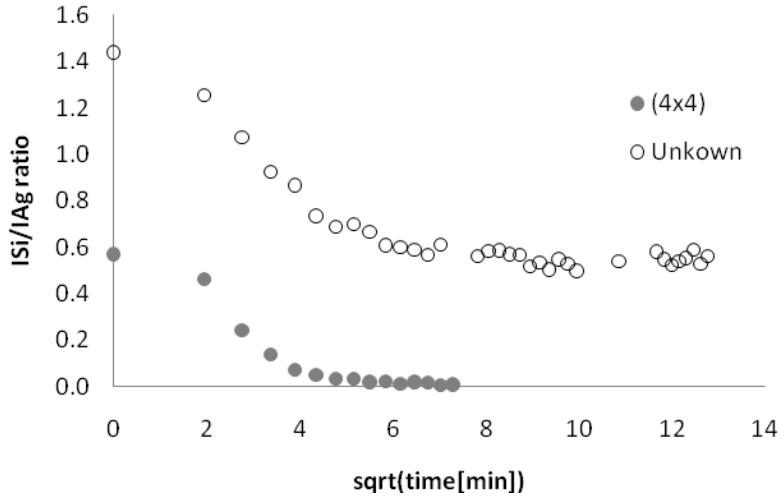

Figure 66 Dissolution kinetics recorded at 300°C after deposition of 1 ML of Si (marked by grey circles) and ~2 ML of Si (marked by empty circles) shown versus the square root of time.

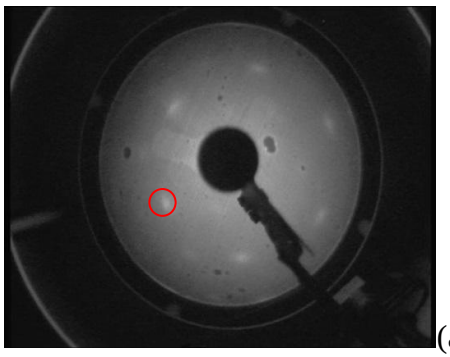
(a)
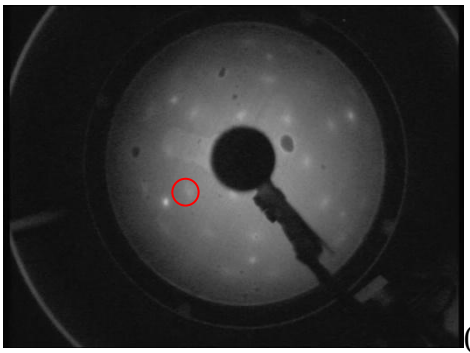
(b)

Figure 67 LEED pattern recorded (a) just after the deposition of about 2 Si ML (Ep=55eV) and (b) at the end of the annealing, on the plateau (Ep=84 eV)

The LEED pattern observed just after the deposition of 2 ML of Si is quite fuzzy. Only spots characteristics of the (4×4) superstructure are visible (highlighted on the picture). Spots of the silver substrate are very weak which is in line with at least 2 complete and flat Si ML. The LEED patterns obtained after annealing show spots characteristics of the silver substrate furthermore that of the (4×4) and of the $\left(2\sqrt{3} \times 2\sqrt{3}\right)R30°$ superstructure relative to the silicene layer.

In order to try to understand the LEED patterns and the kinetics shape observed, we performed STM measurements on this sample as well.

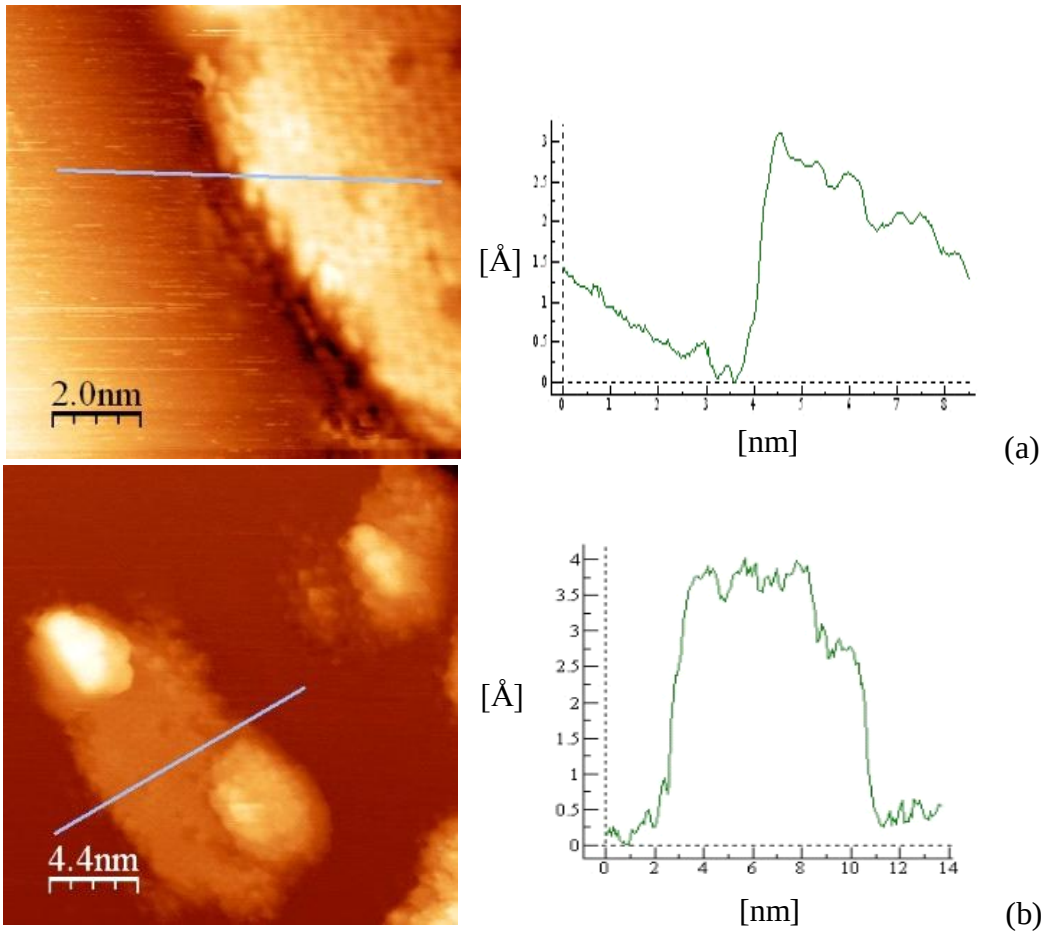

Figure 68 Typical filled state STM images [a) and b)] of the sample surface after the annealing and their line scan next to them.

The surface of the sample shows large terraces of pure Ag with the presence of flat 2D islands of silicon, most of them with the same height (~3.5 Å seen on the line scan) with the same periodic structure on top, which looks like a honeycomb structure. The periodicity of observable superstructure on these 2D islands is found to be 6.6 Å which corresponds to $\sqrt{3}$ of the silicene layer i.e. from the model shown in Figure 65 of the (4×4) superstructure, the distance between two hexagons of silicene on Ag(111) is 3.85 Å (4*2,89/3) and the $\sqrt{3}$ of this distance is 6.67 Å in very good agreement with the STM measurements and the LEED patterns.

Generally it is difficult only from STM images and from LEED patterns to give a structural model. The questions that still remained unanswered are

i) What is the number of silicon (silicene) layers which could give rise to a height of 3.5 Å?

ii) Is the last plane showing a $\sqrt{3}$ periodicity, a complete layer of buckled silicene, or silicon atoms adsorbed on the (4×4) or, finally, Ag atoms adsorbed on the (4×4) due to a segregation phenomenon?

This last assumption would be in line with the deposition of silver on Si(111) which form a $(\sqrt{3} \times \sqrt{3})R30^{\circ}$ superstructure and is known to be quite stable with the temperature [138]. In any case this experiment clearly shows that the islands observed are more stable than a pure (4×4).

Further experiments could be interesting and reasonable to investigate these questions in a more detailed work.

III.4.3 Conclusion

We performed a combination of AES, LEED, STM measurements depositing 1 or more monolayer(s) of Silicene on Ag(111) substrate with two different orientation namely

1) the (4×4) and
2) the $(2\sqrt{3} \times 2\sqrt{3})R30°$

We evaluated the limit of the solubility of Si in Ag from the AES measurements to be ~1-2 at% at 300°C.

This finding could explain that why it is needed to use a higher deposition rate to obtain the $(2\sqrt{3} \times 2\sqrt{3})R30°$ superstructure.

Interestingly in another series of the experiments we could observe the stabilization of a thicker silicene like layer that showing a $(\sqrt{3} \times \sqrt{3})$R30° superstructure relative to the (1×1) silicene. Further investigations are required for a better understanding of this behavior.

My own contribution: *During these experiments my duty was the cleaning and the preparation of samples; furthermore I have performed AES, LEED and STM measurements, I have contributed to the evaluation of the data as well.*

IV. Conclusion

Diffusion and diffusion related solid state reaction phenomena have been studied in four different material couples, namely in the Si-Ge, Ni-Si, Cu-Si and Ag-Si systems. These four materials the Ge, Ni, Cu and the Ag in one way or another play an important role in electronics or for other fields related to materials science such as power sources, solar cells, etc. Since our modern society built upon the shoulders of silicon based technology then the further investigations possible developments are required and are of great importance.

We first discussed our results achieved by computer simulation in the field of diffusion related stress effects. The input parameters covered a quite large range. Considering, however, the importance of the Si-Ge system for the industry, as a starting point for the parameters, data from the Si-Ge system had been chosen deliberately. Prior to our investigation Schmitz et al. [20] pointed out from their experimental results that the intermixing rate in a diffusion couple in spherical geometry could strongly be effected by stress, but surprisingly the parabolic growth rate is preserved. Schmitz et al. explained it by the switching from the Darken to the Nernst–Planck regime forced by the diffusion-induced stress.

We analyzed the question theoretically – for the sake of simplicity, for planar model geometry – to find the role of stress in diffusion and to identify the cause for effects forcing the system to shift from the Darken to the Nernst–Planck regime as it is reported in [20]. In our simulations we started from Stephenson's equations for a one-dimensional, isotropic n component system that describe the diffusion-induced stress development and stress relaxation by viscous flow [11,10]. We considered cases when the diffusion asymmetry was significant (strongly composition dependent diffusion coefficient resulting in significantly faster diffusion on one side of the interface than on the other) and also when it was negligible.

In conclusion we obtained that stress effects do not have any measurable effects on the kinetic coefficient of the interface shift, i.e. the parabolic growth rate is preserved. However, the intermixing rate decreases. The stress field enhances the atomic flux of the slower component but diminishes the other. As a consequence, their initial difference is equalized, leading to the establishment of the Nernst–Planck regime. The development of the Nernst–Planck regime is remarkably fast, finishing before any detectable shift of the interface. These results are in agreement with the experimental results of Schmitz et al. [20]

Then we reported the results achieved in another important system in most of the electronic devices: the Ni-Si. Indeed Ni silicides provide very important contact and protective materials for industry.

To monitor the very beginning of silicide phase formation in the Ni-Si system, we performed X-ray Standing Wave (XSW) based experiments on sandwich structured Ta/a-Si/Ni/a-Si/Ta/substrate samples. The Ta layers served as waveguides (in other words mirror layers). The experiments were realized in the Helmholtz-Zentrum Berlin für Materialien und Energie (HZB) in Germany by using a third generation synchrotron radiation source. We followed the phase formation and growth at a given temperature at which the Ni_2Si phase has formed and continued to grow.

In the Grazing Incidence X-ray Fluorescence (GIXRF) method the samples were irradiated by a beam with fix energy close to the absorption edge of Ni. Accordingly we excited the absorbent Ni atoms and measured the ejected fluorescent signal during their relaxation. By changing the angle of incidence of the beam we could change the transversal mode of the standing wave formed between the waveguide layers, i.e. the position of the nodal and anti-nodal points. This allowed us to tune the position from where the signal came. Afterward we used the software developed by one of our Hungarian team members to reconstruct the composition profile of Ni within the sample. This is a relatively new nondestructive depth profiling method with nanoscale resolution.

Subsequently, we performed Extended X-ray Absorption Fine Structure (EXAFS) measurements in fluorescence detection as well by changing the energy of the beam around the absorption edge of Ni and to keep a given transversal mode of the standing wave constant we also changed the angle of incidence of the beam adequately. This measurement provides information about the local environment of atoms; e.g. the next nearest Ni-Si distance and the number of next nearest Si neighbors of Ni atoms. As this measurement was also performed in the waveguide structure, the information came from not the whole sample but mainly from the position of the nodal points of the standing wave. Accordingly we realized a depth selective EXAFS measurement.

To our knowledge these methods were used first time in our Hungarian group to monitor compound phase formation, namely the formation of CoSi in the Co-Si system. The experiment reported in this thesis is the second example. This was, however, not only a repetition of the previous experiment in another system but we further developed the evaluation method by correlating the results obtained from the *independent* measurements of the GIXRF and EXAFS. From both analyses we were able to determine Ni_2Si/Ni ratio as a function of annealing time and compare them, which increases the reliability of this combined method.

In conclusion we demonstrated that using a combination of EXAFS and GIXRF measurements in waveguide structure and comparing their results, we could follow the very beginning of the phase growth in a metal silicide system in a non-destructive way achieving reliable results. Both the GIXRF and the EXAFS measurements equally pointed out

appearance the later development of the Ni_2Si phase, moreover the GIXRF and EXAFS results showed good correlation.

The third studied system was the Cu-Si system, where we were interested not only in the very beginning of the phase formation but also in the growth kinetics of the phase. The Cu-Si system gains a foothold amongst others in the field of power sources and solar cells as well. For example the Cu_3Si phase turns out to increase the structural integrity, flexibility of Si nanowire/rod based secondary batteries. Furthermore, as metallic atoms in Si reduce the recrystallization temperature of Si through the phenomenon of Metal Induced Crystallization (MIC), this opened a door for the future solar cells to become much more cost effective by allowing the application of less expensive substrates than the currently used quartz glass substrates which resist the very high recrystallization temperature of the silicon.

We performed a combination of experiments and techniques such as X-ray Diffraction (XRD), Atom Probe Tomography (APT), Secondary Neutral Mass Spectrometry (SNMS), profilometer and 4 wire resistance measurements on sputtering deposited samples (Cu/a-Si/substrate, Cu/a-Si/Cu/substrate, a-Si/Cu/a-Si/substrate and Cu/a-Si/Cu/substrate) in order to follow the early stage of phase formation and growth in this system. Essentially we obtained two interesting results from our investigations:

First, we found that in case of the Cu/a-Si/substrate samples the phase formation was followed by a linear kinetics contrary to a result reported in literature, according to which the the phase growth in the 450-500 K range was found to be parabolic [103]. Second, prior to the linear phase growth, we observed an extremely fast phase formation that appeared immediately after the very first and shortest annealing, that took only as long as the sample reached the desired temperature then was cooled down immediately afterwards. Even in this case a quite wide ~20 nm thick product layer was found. To clear up this phenomenon we prepared and investigated two types of samples: Cu/a-Si/Cu/substrate and a-Si/Cu/a-Si/substrate. We have found that the phase formation appeared only on that interface where the Cu was on top position while the other interface remained practically intact. This shows that the preparation sequence of the sample is a crucial point in phase formation processes. In the present case the phenomenon can be explained by the fact that the Si has surface segregation tendency in this system. Hence, during deposition of Si onto Cu the Si atoms prefer to stay on top, whereas deposition of Cu onto Si results in a thermodynamically non-favourable state. Consequently, Cu atoms diffuse into the a-Si layer forming a more diffused interface than in the reverse deposition case. Obviously, phase formation is easier and faster in an intermixed region than at a sharp interface.

Finally we showed our results concerning a quite new material in the field of electronics that is called silicene. The increasing effect of miniaturization and the demand for new candidates that could take the place of silicon and could give a push to the scientific fields of computers and other silicon based technologies, achieved in the recent years to the discovery of a new

material awarded by a Noble prize: the graphene. This material showed remarkable properties that could revolutionize the current state of electronic devices. However its integration into the recent technology is quite complicated. On the other hand, just in the neighborhood of the base material of the graphene, namely the carbon, there are two materials in the periodic table which could theoretically create the same honeycomb two-dimensional structure. These materials are the Ge based germanene and the Si based silicene. The silicene that is the silicon based homolog of the graphene could be the ideal solution for our problem. Investigations concerning this material are very important form both fundamental and theoretical point of view.

In this manner, we investigated the dissolution of Si into Ag for two of the known possible existing silicene superstructures on the Ag(111) substrate, in order to extract more precise dissolution data for this system and, at the same time, to study the stability of these superstructures on elevated temperature. We performed a combination of AES, LEED, STM measurements depositing 1 monolayer of silicene on Ag(111) substrate with two different superstructure orientations, namely (4×4) and $\left(2\sqrt{3} \times 2\sqrt{3}\right)R30°$ superstructures. We determined the dissolution limit of Si in Ag from data obtained from the AES measurements to be 1.88 at% at 300^{o}C.

In conclusion we may note that in the framework of this thesis we investigated Si based binary systems both experimentally and by computer simulation. The chosen systems have not only high industrial potential but are of fundamental importance as they cover the whole range of the basic thermodynamic classes of binary systems such as completely soluble (Si-Ge), insoluble or phase separating (Ag-Si) and compound forming (Ni-Si and Cu-Si). For this reason the achieved results are expected to be interesting to the community of materials sciences.

V. Acknowledgements

This thesis has built upon the shoulders of patient supervisors, helpful colleagues, dedicated friends, and an extremely supporting family and supplemented with the opportunities created by the institutions on both sides.

I'm especially thankful for my supervisors Dr. ***Zoltán Erdélyi*** *and Prof.* ***Christophe Girardeaux*** *and to my tutor Dr. Alain Portavoce to make this whole journey possible and for all the discussions and advices I've got from them.*

I would like to express my sincere thanks to Dr. F. Christien, from the Université de Nantes, and to Dr. K. Vad, from the Institute for Nuclear Research, Hungarian Academy of Sciences, for accepting to be referees of this work and devote a small of their precious time to judge this thesis.

I'm very grateful for the colleagues and the institutions that made possible to reach the equipments and helped to achieve my goals:

I would like to express my gratitude to the ***Department of Solid State Physics*** *and the* ***ATOMKI*** *in Debrecen, Hungary for the possibility that I could prepare my samples and I could use the SNMS, XPS, XRD systems and the profilometer. Especially for Dr. Gábor Langer for his advices and for the countless discussion we had. I'm just as thankful for Dr. Csaba Cserháti, who performed the evaluation of the EXAFS data and for Attila Csik who helped me in the XRD, SNMS and XPS measurements. Furthermore I would like to thank for Prof. Dezső Beke for his contributions in our publications.*

I'm very grateful to the group of the ***Im2np*** *in Marseille, France, where I learned how to use the AES, especially to Dr. Sébastien Vizzini. Furthermore I would like to thank Dr. Omar Abbes all the help I've got from him during the 3 years I spent in Marseille.*

I'm just as grateful to the ***Institute of Materials Physics at the University of Münster*** *in Germany, headed by Prof. G. Schmitz and his team for the APT measurements they performed. I'm especially grateful to Dr. Zoltán Balogh in this team, not just for helping a lot in the measurements during his stay in Debrecen but for sharing his precious time and knowledge ever since whenever I needed it.*

I owe a lot to the ***CINAM*** *in Marseille, France, for the possibility that I could use the AES, LEED and the STM systems and I'm very grateful to the chance that I could work with Dr. Bernard Aufray and Dr. Haik Jamgotchian.*

*I thank to the institute of Helmholtz-****Zentrum Berlin für Materialien und Energie*** *(HZB) synchrotron light source in Germany and to the colleagues there who made possible our synchrotron measurements.*

I'm extremely grateful for all the fellow Ph.d. students and Post-docs as well who made these three years comfortable and funny: Györgyi Glodán, Enikő Furu, Riku Lovics, Fernec Soha, Iurii Kogut, Gábor Molbár and to all the others…

I would like to thank for those lots of colleagues as well who have made the atmosphere inside or outside the institutions simply better in one way or another with their presence. Furthermore I would like to thank to all the co-workers for their contributions.

Finally I would like to thank for my family especially to my parents and to my brother and sister for their continuous support, without who I couldn't make it through.

I would like to express my gratitude to the Institut Francais de Budapest for their support and especially to Mr. Bob Kaba Loemba and the BGF.

This work was supported by the OTKA Board of Hungary (No. NF101329), by the TAMOP 4.2.2.A-11/1/KONV-2012-0036 and TAMOP-4.2.2/B-10/1-2010-0024 projects (implemented through the New Hungary Development Plan co-financed by the European Social Fund, and the European Regional Development Fund).

VI. References

1 The atomic philosophy of the early Greeks – Encyclopedia Britannica / www.britannica.com
2 H. Bracht, S. Brotzmann; Materials Science in Semiconductor Processing 9 (2006) 471–476
3 R. Kube et al, Materials Science in Semiconductor Processing 11 (2008) 378–383
4 J. Philibert, Atom Movements - Diffusion and Mass Transport in Solids, Les Editions de Physique (, 1991).
5 Balogh Zoltán – Diffúziós aszimmetria hatásai nanoskálán (Phd. thesis)
6 D. L. Beke (editor), Diffusion in Semiconductors and Non-Metallic Solids: Diffusion in Semiconductors Vol. 33-A (Berlin: Springer-Verlag, 1998)
7 Balogh Zoltán, Erdélyi Zoltán, Beke L Dezső, Langer A. Gábor, Csik Attila, Hans-Gerd Boyen, Ulf Wiedwald, Paul Ziemann, Alain Portavoce and Christophe Girardeaux, Applied physics letters 92, 143104 (2008)
8 Erdélyi Z, Katona G, Beke DL, Phys. Rev. B 69: pp. 113407-1-4. (2004)
9 http://web.unideb.hu/zerdelyi
10 D. Beke, P. Nemes, Z. Erdélyi, I. Szabó, G. Langer, Material Research Symposium on Proceedings 527 (1998) 99–110.
11 G. Stephenson, Acta Metallurgica 36 (10) (1988) 2663–2683.
12 H. Mehrer, Diffusion in Solids, Springer -Verlag, Berlin, Heidelberg, 2007.
13 Hartung F, Schmitz G. Phys Rev B 2001;64:245418.
14 Larche´ FC, Cahn JW. Acta Metall 1982;30:1835
15 Gordon MH, Schmidt WF, Qiao Q, Huang B, Ang SS. Exp Mech 2002;42:332.
16 Gurov KP, Gusak AM. Fizika Metallov Metallovedenie 1985;59:1062.
17 Gusak AM, Kornienko SV, Lutsenko GV. Diff Def Data 2007;264:109.
18 Svoboda J, Fischer F. Acta Mater 2011;59:1212
19 Fischer F, Svoboda J. Acta Mater 2010;58:2698.
20 G. Schmitz, C.B. Ene, C. Nowak, Acta Materialia 57 (9) (2009) 2673–2683.
21 D.L. Beke, I.A. Szabó , Z. Erdélyi, G. Opposits, Materials Science and Engineering A 387–389 (2004) 4–10.
22 Z. Erdelyi, D. L. Beke, P. Nemes, and G. A. Langer, Phil. Mag. A79/8, 1757 (1999)
23 V. I. Dybkov, Solid State Reaction Kinetics, IPMS Publications, 2013
24 B.Ya. Pines. K voprosu o mekhanizme diffuzii v kristallakh khimicheskikh soedineniy i kinetike reaktivnoy diffuzii // Fiz. Tverd. Tela.- 1959.- V. 1, No. 3.- P. 482-488.
25 B.Ya. Pines. *Ocherki po metallofizike*.- Khar'kov: Izd-vo Khar'kovskogo Universiteta, 1961.
26 H. Bracht, S. Brotzmann / Materials Science in Semiconductor Processing 9 (2006) 471–476.
27 R. Kube et al./Materials Sciencein Semiconductor Processing 11 (2008)378–383
28 E.A. Guliants and W.A. Anderson, J. Appl. Phys., 89 (2001) 4648.
29 T.J. Konno and R. Sinclair, Philos. Mag., 66 (1992) 749.
30 A. Hiraki, Surf. Sci. Rep., 3 (1984) 357
31 Z. Wang, L.H. Jeurgens, J.Y. Wang and E.J. Mittemeier, Adv. Eng. Mater., 11 (2009) 131)
32 Z. Erdélyi, Ph.D. Thesis, Diffusion in nanomaterials and nanosize effects on mass transport: Experiments and simulations, UNIVERSITE DE DROIT, D'ECONOMIE ET DES SCIENCES D'AIX-MARSEILLE FACULTE DES SCIENCES ET TECHNIQUES DE SAINT-JEROME, 2001
33 J.W. Gibbs, The Collected Works of J.W. Gibbs, Yale University Press, New Haven, Vol. 1 (1948)
34 E.A. Guggenheim, Trans. Faraday Soc., 36, 397 (1940)
35 D. McLean, "Grain Boundaries in Metals." Oxford Univ. Press, Oxford, 1957.
36 F.L. Williams and D. Nason, *Surf. Sci.*, **45**, 377 (1974)
37 M.J. Sparnaay, Surf. Sci Rept., 4, 101 (1984) M.J. Kelley and V. Ponec, *Prog. Surf. Sci.*, **11**, 139 (1981)
38 G. Tréglia, B. Legrand et F. Ducastelle, *Europhys. Lett.*, **7**, 575 (1988)
39 Z. Erdélyi, C. Girardeaux, Zs. Tőkei, D. L. Beke, Cs. Cserháti, A. Rolland Investigation of the interplay of nickel dissolution and copper segregation in Ni/Cu(111) system. SURFACE SCIENCE 496:(1-2) pp. 129-140. (2002)
40 D. L. Beke, C. Cserháti, Z. Erdélyi, I. A. Szabó, Chapter 7 - "Segregation in Nanostructures" in Nanoclusters and Nanocrystals, edited by Hari Singh Nalwa, American Scientific Publishers, 2003
41 P. Wynblatt and R.C. Ku, *Surf. Sci.*, **65**, 511 (1977)
42 J. Freidel, *Advan. Phys.*, **3**, 446 (1954)

43 http://www.microscopy.ethz.ch/bragg.htm
44 Qun Shen, Cornell University; CHESS Technical Memo 01-002, March 8, 2001
45 http://idw-online.de
46 https://www.helmholtz-berlin.de
47 A. Gupta, N. Darowski, I. Zizak, C. Meneghini, G. Schumacher, A. Erko, Spectrochim. Acta B 2007, 62, 622.
48 A. Gupta, C. Meneghini, A. Saraiya, G. Principi, D. K. Avasthi, Nucl.Instrum. Methods. Phys. Res. B 2003, 212, 458.
49 Z. Erdélyi, C. Cserháti, A. Csik, L. Daróczi, G. A. Langer, Z. Balogh, M. Varga, D. L. Beke, I. Zizak and A. Erko; X-Ray Spectrom. **38**, 338–342 (2009)
50 B.N. Dev, A.K. Das, S. Dev, D.W. Schubert, M. Stamm, G. Materlik, Resonance enhancement of X-rays in layered materials: application to surface enrichment in polymer blends, Phys. Rev., B 61 (2000) 8462.
51 S.K. Ghose, B.N. Dev, A. Gupta, Resonance enhancement of X-rays and fluorescence yield from marker layers in thin films, Phys. Rev. B64 (2001) 233.
52 Atsuo Iida;Grazing Incidence y-ray fluorescence analysis using synchrotron radiation; Advances in x-ray Analysis, Vol. 35 (1993)
53 L. G. Parratt, Phys. Rev. 1954, 95, 359.
54 D. L. Windt, Comput. Phys. 1998, 12, 360
55 S. K. Ghose, B. N. Dev, Phys Rev B 2001, 63, 245409.
56 Matthew Newville; Fundamentals of XAFS, Consortium for Advanced Radiation Sources, University of Chicago, Chicago, IL, 2004
57 G. Vlaic, L. Olivi, CROATICA CHEMICA ACTA, CCACAA 77 (3) 427-433 (2004)
58 www.haverford.edu
59 K. Vad, A. Csik, G. A. Langer; Secondary neutral mass spectrometry – a powerful technique for quantitative elemental and depth profiling analyses of nanostructures; SPECTROSCOPYEUROPE; Vol. 21 No. 4 (2009)
60 H. Oechsner; Electron and mass spectrometric analysis of plasma controlled surfaces and thin films; Pure & Appl. Chem., Vol. 64, No. 5, pp. 615-622. (1992)
61 H. Oechsner; Analysis of electrically non-conducting sample structures with electron and mass spectroscopic methods; Thin Solid Films 341 (1991) 105-108
62 H.Gnaser, H. Oechsner; Preferential sputtering of isotopes: fluence and emission-angle dependence; Phys. Rev. Let. 63, 24 (1989) 2673-2676
63 www.ambiostech.com
64 http://mxp.physics.umn.edu/s04/Projects/s04xrf/
65 http://dc351.4shared.com/doc/t1dJN7YW/preview.html
66 http://www.specs.com/
67 Y. Kuk et al., Rev. Sci. Instrum. 60, 165 (1989)
68 http://www.fhi-berlin.mpg.de
69 W. Ranke, Fritz-Haber-Institut der MPG; Low Energy Electron Diffraction – http://www.fhi-berlin.mpg.de/acnew/department/pages/teaching/pages/teaching__wintersemester__2003_2004/ranke_leed_160104.pdf
70 Ertl/Küppers figure. 9.12, p 217
71 http://wiki.utep.edu/display/~ckroy/Auger+Electron+Spectroscopy+%28AES%29
72 http://www.pcs-gerstl.de/joomla/index.php/component/virtuemart/?page=shop.product_details&flypage=flypage.tpl&product_id=60&category_id=2
73 Müller, E.W., Panitz, J.A. and McLane, S.B., Rev.scient. Instrum., 1968, 39, 83.
74 Cerezo A, Godfrey TJ, Smith GWD, Application of position-sensitive detector to atom probe microanalysis, REVIEW OF SCIENTIFIC INSTRUMENTS 59:(6) pp 862-866 (1988).
75 R. Schlesiger, C. Oberdorfer, R. Würz, G. Greiwe, P. Stender, M. Artmeier, P. Pelka, F. Spaleck, G. Schmitz, Review of Scientific Instruments, 81, 043703 (2010)
76 T.B. Massalski (ed.), Binary Alloys Phase Diagrams, second edition (ASM International), 1992
77 A. Portavoce, Mécanismes élémentaires de redistribution de l'antimoine au cours de la croissance d'hétérostructure$Si/Si_{(1-x)}Ge_{(x)}$: Diffusion, ségrégation, désorption et effet surfactant, Thèse doctorat, (2002)
78 Z. Erdélyi, Z. Balogh, D. Beke, Acta Materialia 58 (17) (2010) 5639–5645.
79 F. Spaepen, Journal of Magnetism and Magnetic Materials 156 (1–3) (1996) 407–410.
80 S.M. Prokes, F. Spaepen, Applied Physics Letters 47 (3) (1985) 234–236.

81 J.J. Wortman, R.A. Evans, Journal of Applied Physics 36 (1) (1965) 153–156.
82 Z. Erdélyi, B. Parditka, D. L. Beke, Scripta Materialia 64 (2011) 938–941
83 R. Anderson, J. Baglin, J. Dempsey, W. Hammer, F. d'Heurle, S. Petersson, Appl. Phys. Lett. 35 (1979) 285
84 K.N. Tu, J. Appl. Phys. 48 (1977) 3379.
85 S. Petersson, E. Mgbenu, P.A. Tove, Phys. Status Sol. A 36 (1976) 217.
86 K.N. Tu, W.K. Chu, J.W. Mayer, Thin Solid Films 25 (1975) 403.
87 F.M. d'Heurle, R.M. Geffken, K.N. Tu, IBM Tech. Disclosure Bull. 19 (1977) 3233.
88 C. Lavoie, F.M. d'Heurle, C. Detavernier, C. Cabral, Microelectron. Eng. 70 (2003) 144.
89 J.A. Kittl, A. Lauwers, O. Chamirian, M. Van Dal, A. Akheyar, M. De Potter, R. Lindsay, K. Maex, Microelectron. Eng. 70 (2003) 158.
90 S.-L. Zhang, Microelectron. Eng. 70 (2003) 174.
91 F.M. d'Heurle, J. Mater. Res. 3 (1988) 167.
92 C. Lavoie, C. Coia, F.M. d'Heurle, C. Detavernier, C. Cabral Jr., P. Desjardins, A.J. Kellock, Diffus Defect Data. Pt A Defect and Diffusion Forum 237–240 (2005) 825.
93 C. Lavoie et al. / Microelectronic Engineering 83 (2006) 2042–2054
94 S. Oukassi, J. S. Moulet, S. Lay, and F. Hodaj, Microelectron. Eng. **86**, 397 (2009).
95 N. Mattoso, J. Mater. Sci. **30**, 3242 (1995).
96 L. A. Clevenger and C. V. Thomson, J. Appl. Phys. **67**, 1325 (1990).
97 B. Ravel & M. Newville J.Synchrotron Rad. (2005), 12:4, pp. 537-541
98 P. Villars; Pearson's handbook: crystallographic data for intermetallic phases, Materials Park, OH: ASM International, 1997
99 S.B. Lee, D.K. Choi, F. Phillipp, K.S. Jeon and C.K. Kim, Appl. Phys. Lett., 88 (2006) 083117.
100 Y.C. Her, C.W. Chen and C.L. Wu, J. Appl. Phys., 99 (2006) 113512.
101 H.X. Chen, Z.X. Dong, Y.P. Fu, and Y. yang, J. Solid State Electrochem., 14 (2010) 1829.
102 S.L. Ou, P.C. Kuo, S.C. Shen, T.L. Tsai, C.Y. Yeh, H.F. Chang, C.T. Lee and D. Chiang, Appl. Phys. Lett., 99 (2011) 121908.
103 R.R. Chromik, W.K. Neils and E.J. Cotts, J. Appl. Phys., 86 (1999) 4273.
104 F.M. d'Heurle and P. Gas, J. Mater. Res., 1 (1986) 205.
105 T.E. Schlesinger and R.C. Cammarata, Appl. Phys. Lett., 59 (1991) 441.
106 C. Cserháti, Z. Balogh, A. Csik, G.A. Langer, Z. Erdélyi, Gy. Glodán, G.L. Katona, D.L. Beke, I. Zizak, N. Darowski, E. Dudzik and R. Feyerheim, J. Appl. Phys., 104 (2008) 024311.
107 J.Y. Cheng and L.J. Chen, J. Appl. Phys., 69 (1991) 2161.
108 F. Nemouchi, D. Mangelinck, C. Bergmann, P. Gas and U. Smith, Appl. Phys. Lett., 86 (2005) 041903.
109 B. Parditka, M. Verezhak, Z. Balogh, A. Csik, G. A. Langer, D. L. Beke, M. Ibrahim, G. Schmitz, Z. Erdélyi, Acta Materialia 61 (2013) 7173–7179
110 R. Schlesiger, C. Oberdorfer, R. Würz, G. Greiwe, P. Stender, M. Artmeier, P. Pelka, F.Spaleck and G. Schmitz, Rev. Sci. Instrum. 81 (2010) 043703
111 B.E. Deal and A Groves, J. Appl. Phys. 36 (1965) 3770.
112 J. Philibert, Mat. Sci. Forum, 155-156 (1994) 15.
113 U. Gössele and K. Tu, J. Appl. Phys. 53 (1982) 3252.
114 D.L. Beke, Z. Erdélyi, Z. Balogh, Cs. Cserhát, G.L. Katona, J. of Nano Res. 7 (2009) 43.
115 J. Klafter and I. Sokolov, Phys World 18, (2005) 29.
116 Z. Erdélyi and D.L. Beke, J. Mater. Sci. 46 (2011) 6465
117 M. Ibrahim, Z. Balogh, P. Stender, R. Schlesiger, G. H. Greiwe, G. Schmitz, B. Parditka, G.A. Langer and Z. Erdélyi; to be submitted to Acta Materialia
118 R.L. Fogelson, Y.A. Ugay, A.V. Pokoyev, I.A. Akimova and V.D. Kretinin, Phys. Met. Metallogr., 35 (1973) 226.
119 S. Coffa, J.M. Poate, D.C. Jacobson, W. Frank and W. Gustin, Phys. Rev. B, 45 (1992) 8355 .
120 M. Gusak and K.P. Gurov, Solid State Phenom., 23-24 (1992) 117.
121 J. Philibert, Mat. Sci. Forum, 155-156 (1994) 15.
122 Novoselov, K. S. et al. (2004). "Electric Field Effect in Atomically Thin Carbon Films". Science 306 (5696)
123 Kostya Novoselov, Nature Materials 6, 720 -721 (2007)
124 Graphene Sensors; Hill, E.W. ; Centre for Mesoscience & Nanotechnol., Univ. of Manchester, Manchester, UK ; Vijayaragahvan, A. ; Novoselov, K. ; Sensors Journal, IEEE: Volume:11 Issue:12

125 K. S. Novoselov, A. K. Geim et al.; Two-dimensional gas of massless Dirac fermions in graphene, Nature 438, 197-200 (2005)
126 S. Lebègue and O. Eriksson, Electronic structure of two-dimensional crystals from ab initio theory ,PHYSICAL REVIEW B 79, 115409 2009
127 S. Cahangirov et al.; Two- and One-Dimensional Honeycomb Structures of Silicon and Germanium, PRL 102, 236804 (2009)
128 B. Aufray, A. Kara, S. Vizzini, H. Oughaddou, C. Léandri, B. Ealet, et al., Graphene-like silicon nanoribbons on Ag(110): A possible formation of silicene, Applied Physics Letters. 96 (2010) 183102.
129 B. Lalmi, H. Oughaddou, H. Enriquez, A. Kara, S.S. Vizzini, B.B. Ealet, et al., Epitaxial growth of a silicene sheet, Applied Physics Letters. 97 (2010) 223109.
130 C. Léandri, H. Oughaddou, B. Aufray, J.M. Gay, G. Le Lay, a. Ranguis, et al., Growth of Si nanostructures on Ag(001), Surface Science. 601 (2007) 262–267.
131 A. Fleurence et al.; Experimental Evidence for Epitaxial Silicene on Diboride Thin Films, PRL 108, 245501 (2012)
132 L. Meng, Y. Wang, L. Zhang, S. Du, R. Wu, L. Li, et al., Buckled Silicene Formation on Ir(111)., Nano Letters. (2013).
133 R. Arafune et al.; Structural transition of silicene on Ag(111), Surface Science 608 (2013) 297–300
134 D, Chiappe et al.; Local Electronic Properties of Corrugated Silicene Phases, Adv. Mat. vol. 24, no. 37, pp. 5088-93 (2012.)
135 Yann Colignon et al; Etude expérimentale d'un plan de silicium depose sur une surface d'argent(111); Rapport de stage de master 2.; (2011)
136 H Jamgotchian et al 2012 J. Phys.: Condens. Matter 24 172001
137 R.E. Hoffman, Acta Metall. 6 (1958) 95
138 N. Mariotti et al.; Scanning tunneling microscopy at multiple voltage biases of stable "ring-like" Ag clusters on Si(111)–(7×7), Surface Science 606 (2012) 1755–1759